SELF-PROPAGATING HIGH-TEMPERATURE SYNTHESIS (SHS) OF POROUS PARTS USING NANOCRYSTALLINE NITI

FRANCIS GOH CHUNG WEN

School of Mechanical and Aerospace Engineering

A thesis submitted to the Nanyang Technological University
in fulfilment of the requirement for the degree of
Master of Engineering

2006

ACKNOWLEDGEMENTS

The author would like to express his deepest and most sincere gratitude to his two supervisors, Associate Professor Lim Chu-Sing and Dr. Tay Bee Yen for their guidance and advice throughout this project. He would like to convey his appreciation for their patience, encouragement and understanding throughout the duration of this project. At the same time, the author would like to extend his sincere thanks to Dr Gu Yan Wei and Dr John Yong (Forming Technology Group Manager), who have in one way or other supported the work. The work was carried out under the research grant of SIMT/02-420004 by SIMTech in collaboration with NTU. The author wishes like to attribute a special thanks to the Singapore Institute of Manufacturing Technology (A*STAR) for the research studentship.

TABLE OF CONTENTS

LIST OF FIGURES

LIST OF TABLES

LIST OF NOTATIONS

h	Height of compacted pellet
d	Diameter of compacted pellet
m	Weight of compacted pellets
ρ	Green density general
ε	General porosity
$NiTi_{100\%}$	Reactant with 100% elemental powder of composition ratio
$NiTi_{MA\ 25\%}$	Reactant with 75% elemental powder and 25% nanocrystalline powder of composition ratio
$NiTi_{MA\ 50\%}$	Reactant with 50% elemental powder and 50% nanocrystalline powder of composition ratio
α	Radiation of X-ray diffractomer
d_s	crystallite size
θ	Bragg angle
η	Lattice strain
B	Peak width at half the maximum intensity
λ	Wavelength of the X-radiation used (i.e. 1.5406 $\mathring{A}$)
X	The percentage of composition mixture (i.e. 50%)
M	The atomic weight in [amu] (i.e. M_{Ti} - 47.9 & M_{Ni} - 58.71)
V_{ad}	Adiabatic steady-state velocity
V_m	Velocity prior to quench out
T_0	Initial Temperature
T_{ig}	Ignition temperature
T_{ad}	Adiabatic combustion temperature
T_c	Actual combustion temperature
$C_p(R_i)$	The heat capacity of the reactant
$L(R_i)$	The phase transformation enthalpy of the reactant and subscript i refer to solid or liquid phase of reactant
ΔH_f	Changes (absorbed or evolved) of enthalpy of formation
T_m	Melting point of the compound $NiTi$
ΔH_m	Heat fusion of the $NiTi$
ν	Melting fraction of $NiTi$
$C_{ps}(p)$	$NiTi$ heat capacities in the solid phase
$C_{pl}(p)$	$NiTi$ heat capacities in the liquid phase
P_s	Power supply of ignition system
d_e	Distance of the electrode
Q_s	Gas system flow rate

LIST OF ABBREVIATIONS

Ni	Nickel
Ti	Titanium
Ca	Calcium
Co	Cobalt
Sr	Strontium
Fe	Iron
MA	Mechanical Alloying
XRD	X-ray diffraction
TEM	Transmission electron microscopy
SEM	Scanning electron microscope
EDS	Energy-dispersive X-ray spectrometry
DSC	Differential scanning calorimeter
M_s	Martensite-start temperature upon cooling
M_f,	Martensite-finish temperature upon cooling,
A_s	Reverse-transformation-start temperature upon heating
A_f,	Reverse-transformation-finish temperature upon heating
M_d	Highest temperature to strain-induced martensite
SMA	Shape memory alloy
SME	Shape memory effect
SE	Superelasticity
HIP	Hot isostatic pressing
SPS	Spark plasma sintering
SHS	Self-propagation high-temperature synthesis
SADP	Selected-area diffraction pattern

ABSTRACT

Porous Nickel Titanium (NiTi) shape memory alloy (SMA) is a promising material for use in applications such as biomedical implants. It has effective damping characteristics to shock by utilizing the energy absorption capabilities. Conventional methods such as the sintering process, hot isostatic pressing (HIP) and spark plasma sintering (SPS) have also been used to produce porous NiTi SMA. However, these methods are generally slow. The self-propagation high-temperature synthesis (SHS) process, on the other hand, has been proven to be an ideal alternative in this project, with its rapid processing capability and adaptability in producing materials into cellular/porous structure.

In this study, SHS was used to fabricate porous NiTi. The objectives of this study were to achieve nanocrystalline Ni-Ti and investigate the employment of SHS for this. Several process parameters were used to study influence on morphology and reduction of undesirable by-product phases. The effects of compaction characteristics, green porosity of compacted reactant, preheating temperatures and the inclusion of nanocrystalline powders on pore morphology and phase formation of products were investigated. In this study, the variables of experimental parameters such as the compression forces of 8, 16, 24 kN and preheating temperatures of 200 ^{o}C and 300 ^{o}C on three different sets of chemical composition ratios of reactants ($NiTi_{100\%}$, $NiTi_{MA25\%}$, and $NiTi_{MA50\%}$) were examined. Thermal reaction was employed to control the austensite phase transition (reverse martensitic transformation) of the porous NiTi. The strength characteristic of the synthesized porous NiTi was then evaluated.

The concept of using mechanical alloying (MA) process incorporated into SHS to fabricate porous NiTi was employed in this research. Nanocrystalline Ni-Ti reactant powder as a reaction agent was formulated. By adding 25% nanocrystalline reaction agent ($NiTi_{MA25\%}$): mean pore sizes of 100 to 600 μm with general porosity ranging between 52 to 58 vol.% of porous NiTi parts were obtained. Using the nanocrystalline reaction agent additive helped produce porous parts which NiTi was the major phase at 300^{o}C preheating temperature. This major phase increased by 13% and resulted in reduced unwanted by-products as compared ta not using the reaction agent ($NiTi_{100\%}$). Furthermore, no undesirable unreacted Ni was observed in the final porous NiTi part. This unreacted Ni is carcinogenic and will affect the performance of the SMA. In addition, increased amount of the reaction agent to 50% ($NiTi_{MA50\%}$) produced dense NiTi part.

Abstract

Conventionally, elemental reactant ($NiTi_{100\%}$) produced an unsuitable pore size. Large mean pore sizes of synthesised parts ranging from 1000 to 4500 μm with general porosity ranges between 43 to 57 vol.% were obtained. In addition, the unreacted Ni was not eliminated in the final products.

In addition, the additive nanocrystalline reaction agent ($NiTi_{MA25\%}$) in SHS-synthesized parts achieved almost 300% increase in mean maximum compressive stress as compared to that of porous $NiTi_{100\%}$. SHS-synthesized porous $NiTi_{100\%}$ and $NiTi_{MA25\%}$ were solution treated. The results showed an increment of predominant phases (B2 and B19') in porous $NiTi_{100\%}$ and $NiTi_{MA25\%}$ by almost 17% and 27% respectively (as compared to the non-solution treated specimens). In solution treatment at 1000 ^{o}C and subsequently aging, porous $NiTi_{100\%}$ at 550 ^{o}C obtained high austensite finish temperatures (A_f) at around 76 ^{o}C. With similarly heat treated porous $NiTi_{MA25\%}$ (with additive of nanocrystalline reaction agent), A_f temperatures at around 53 ^{o}C were obtained.

Based on this study, it was found that decreasing green porosity of compacted reactants by increasing compression forces had decreased the pore size and general porosity in the final porous NiTi part. Furthermore, increasing of preheating temperature during the SHS process had increased the NiTi phase formation. The green porosity (initial sample density) and preheating temperature influenced morphology and product composition of the synthesized parts. The study also established that additive nanocrystalline Ni-Ti reaction agent by mechanical alloying process is instrumental in the SHS process. In this study, the author demonstrated that the addition of nanocrystalline NiTi reaction in SHS increases the material systems' activation energy levels thus lowering the activation barrier and synthesis temperature.

CHAPTER 1 INTRODUCTION

1.1 Self-propagating high-temperature synthesis(SHS)

SHS offers more advantages compared to conventional powder metallurgy (PM)(e.g. sintering, hot isostatic pressing (HIP) and spark plasma sintering (SPS)). This process is simple and avoids the need for expensive process facilities and equipment. Furthermore, the rapid exothermic reaction process leads to time and cost savings. The SHS process is associated with combustion wave and has the ability to expel volatile impurities as a wave propagates through the sample. As a result, it leads a higher purity of products [1]. The core advantage of the SHS process is the ability to manipulate the pore morphology within the porous NiTi by changing its combustion temperatures. This factor is then able to produce an "engineered" pore size within the porous NiTi part. A typical process compacted the powders and ignited by an ignitor (i.e. oxyacetylene torch, electric arc, induction coil or laser beam). This process is self-sustaining through the reactant mixture in the form of a propagating combustion wave [1]. In this way, the SHS process is able to create its own exothermic reaction thus offering the production of less costly porous composites and intermetallics.

1.2 Limitations and motivations

The research in this field has not many information on the influence of the process in producing porous NiTi structures (pore morphology) [2-6]. Conventional methods (i.e. sintering, HIP and SPS) have not been able to manipulate pores size and achieve the homogenous pores in the final product. To control either a suitable pore size or obtain a NiTi (B2 and B19) dominant phase in the final porous NiTi by SHS has not yet been achieved to date. This has posed a challenge to many researchers [2-6]. In addition, the elimination of unreacted nickel in the porous SHS NiTi is needed if such porous material is to be used in biomedical applications. Ni can cause the potential deleterious effects in the human body [7].

The goal of synthesizing single phase NiTi from elemental powder via SHS has not been achieved yet. The products were typically a mixture of several intermetallic phases, i.e., NiTi, Ti_2Ni, Ni_3Ti and Ni_4Ti_3. Process parameters such as higher preheating temperature, finer powder size, higher initial reactant density were employed to minimize the secondary intermetallic phases [2-5, 8-11]. These undesirable secondary intermetallic phases cause

difficulties in achieving the unique mechanical properties such as Shape Memory Effect (SME) and Superelasticity Effect (SE).

1.3 Objectives

Hence, the objectives of the project are:

1. To investigate the employment of self-propagating high temperature synthesis (SHS) process parameters for the production of porous NiTi structures.
2. To achieve nanocrystalline powder as reaction agent and investigate the effect on SHS process.
3. To minimize the secondary intermetallic phase (i.e. Ti_2Ni, Ni_3Ti) and eliminate unreacted Nickel in order to optimise single phase of NiTi SMA
4. To evaluate the characteristics of the synthesized porous NiTi.
5. To study the effects of heat treatment on the austensite phase transition (reverse martensitic transformation) and on possible manipulation of phase transition transformation of the porous NiTi.

1.4 Scope

SHS is to be established and employed to rapidly produce porous NiTi parts. This process exploits the exothermicity of reactants (Ni-Ti) and ability to create a highly porous structure via combustion synthesis. In addition, SHS is investigated to manipulate the pore morphology of the material by controlling the process of combustion temperatures which makes it possible to achieve "engineered' pore morphology [12]. Hence several process variables and parameters such as NiTi elemental powder, mechanical alloying (MA) powder (i.e. nanocrystalline reaction agent) and ignition process parameters (i.e. pre-heat temperature, voltage, current) are to be investigated. The nanocrystalline material is to be created by MA process. MA has the capability of introducing new additional energy into the material via utilizing the atomic arrangement in the cores of defect such as grain boundaries, interphase boundaries or dislocations [13]. Furthermore, the nanoscaled materials/reaction agents were developed by mechanical alloying process offers a broad range of chemical composition and atomic structure. These results may improve the phase, mechanical and physical properties of NiTi SMA. Hypothetically through this reaction optimisation process, the unreacted nickel will be minimized or eliminated. The evaluation of the strength characteristics of synthesized porous NiTi such as ultimate compressive strength and Young's Modulus will be conducted.

The thermal reaction treatment process is used to study the austensite phase transition (reverse martensitic transformation) behavior and may possibly be used to manipulate the phase transition transformation of the porous NiTi SMAs. This may further reduces the nickel residues in the SHS synthesized parts through homogenisation during the thermal treatment. Furthermore, it helps to remove the residual hydrogen in the synthesized parts as this would influence the formation of stress-induced martensite.

Several apparatus are to be used for characterising the properties and performance of the synthesized porous NiTi. In the morphology analysis, equipment such as optical image analysis, scanning electron microscope (SEM), transmission electron microscopes (TEM), image analysis and porosimetry are used. The phase analysis is done on x-ray diffraction (XRD), and energy-dispersive X-ray spectrometry (EDS). Uniaxial compression tests will be performed on the specimens using an INSTRON hydraulic universal testing machine. The reveres transformation behavior of the porous NiTi SMA during heat treatment will be investigated using modulated differential scanning calorimeter (DSC). The scope of the research work is illustrated in Figure 1.1.

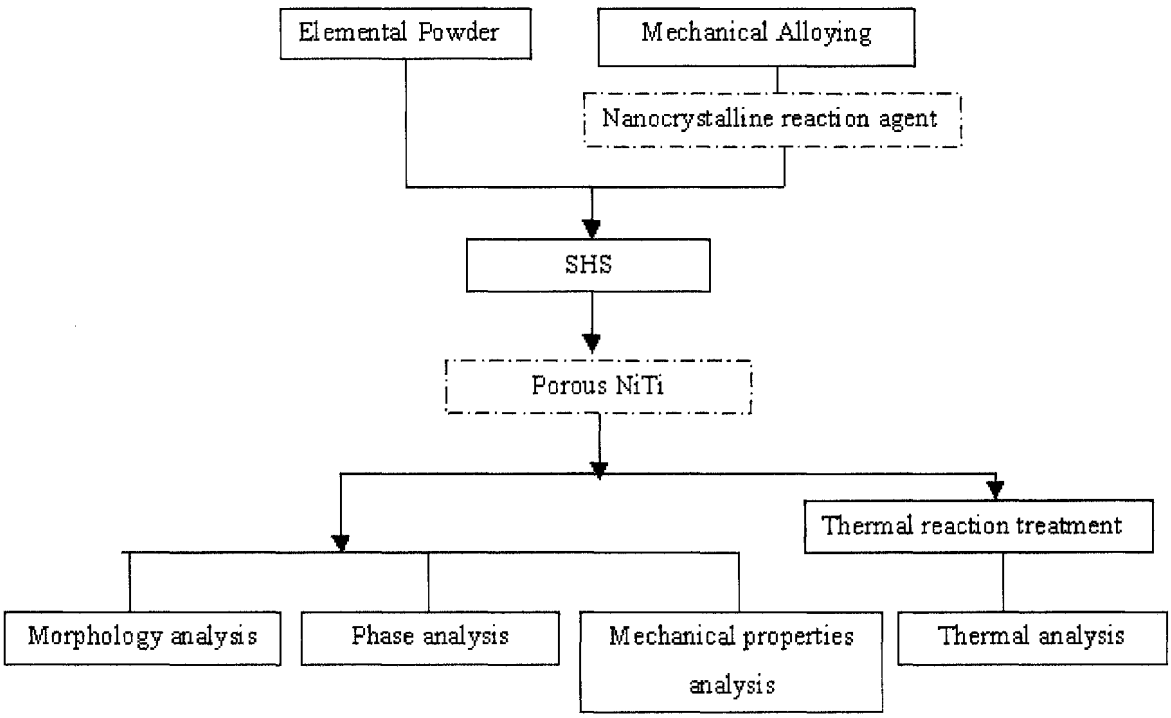

Figure 1.1 The process flow chart

CHAPTER 2 LITERATURE REVIEW

This chapter reviews published information on the related subject matter: NiTi shape memory alloy (SMA), porous NiTi, different methods of producing porous material and the fundamentals of self-propagation high-temperature synthesis (SHS). The experimental approach theory for this research is also included.

2.1 The Nickel Titanium (NiTi) shape memory alloy (SMA)

2.1.1 History on NiTi SMA

The first patent on NiTi was tradenamed 'Nitinol' by the Naval Ordnance Laboratory in 1965 by Buehler [14] and his colleagues. In the late 1960s, Raychem developed the first industrial SMA application in aeronautics with Cryofit connector for F-14 airplane hydraulic circuits. The interest in NiTi as an implant biomaterial was sparked off by Andreasen *et al.* [15] who developed a superelastic dental braces with shape memory retention capabilities. NiTi shape memory alloys (SMAs) offer shape memory effect and superelasticity properties which are suitable for medical implants. These unique characteristics of NiTi have catalysed the recent research in producing porous NiTi SMAs for biomedical application [3, 5, 16-18]. The possibility of producing SMAs in porous form opens new applications including reduced Young's modulus, improved osseointegration and possibly drug delivery.

2.1.2 The mechanism of SME and superelasticity of NiTi SMA

The SME and superelasticity phenomena are known thermal and mechanical SMA characteristic respectively. The thermal SMA characteristic at martensite state is soft and ductile and can be easily deformed when stress is applied. The thing reverts to their original shape when it reaches a certain temperature phase (i.e. austensite state where material is strong and hard). This phenomenon is known as SME and illustrated in Figure 2.1 (1 to 5). When the SMA at stress-induced martensite state exhibits SE property, it performs extreme elasticity and reversible deformation up to 8% at a constant stress (as show in Figure 2.1 (1 to 2))[11]. The mechanisms of SME and SE were further elaborated as below.

Figure 2.2 shows the phase-temperature transformation hysteresis loop describing the event of SME. Figures 2.1(1)-(5) correspond to the event by using photo illustration. The hysteresis H is an important characteristic of heating and cooling conditions on SME. It is characterised by four temperatures: M_s, which is the martensite-start temperature upon cooling, M_f, which is the martensite-finish temperature upon cooling, A_s which is the reverse-transformation-start temperature upon heating and A_f, which is the reverse-transformation-finish temperature upon heating. Figure 2.1 shows a classical example of SME phenomenon of a NiTi SMA wire. Initially, the wire has the shape of parent phase in martensite phase (Figure 2.1(1a)) at the M_s (Figure 2.2(1)). As the result of self-accommodation, the martensite variants are formed side by side (Figure 2.1(2b)) when it cooled below at M_s. These variants of martensite phase exist in a same parent phase structure but different in orientation. More elaborate explanation on this martensitic transformation of self-accommodation can be found in references [19-21]. Once the wire is deformed when stress is applied at the M_f, deformation will proceed by twin boundary movement as show in Figures 2.1(2b) to (2c). Lastly, the SME (i.e. revert back to its originated shape) will occur once the temperature is heated above A_f (as shown in Figures 2.1(3)-(5)).

SE undergoes a shear-like mechanism when stress is loaded. This behaviour is called stress-induced martensitic transformation as shown in Figures 2.1(1a to 2c). With the stress continually to apply, this transformation will still occur as long as the temperature reach above M_s or near A_f. Once a point above A_f, it can no more stress can be induced (as shown in Figure 2.2). Hence, above M_d in a NiTi SMA will deform like other ordinary materials by slipping.

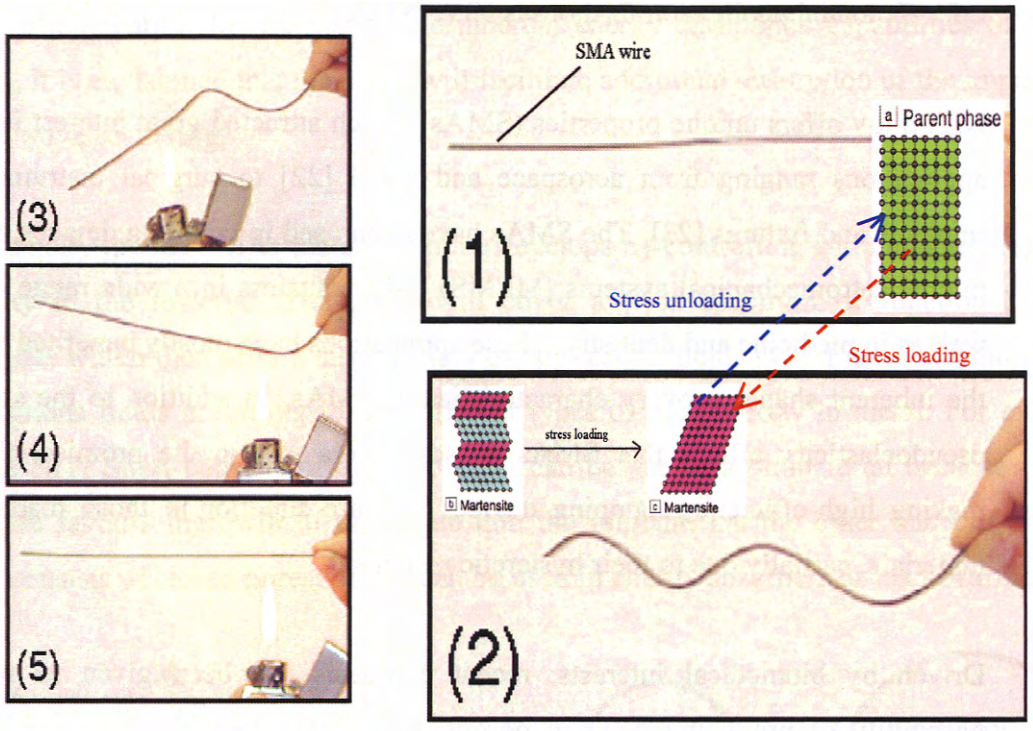

Figure 2.1 Photography of illustration on SME behavior [19]

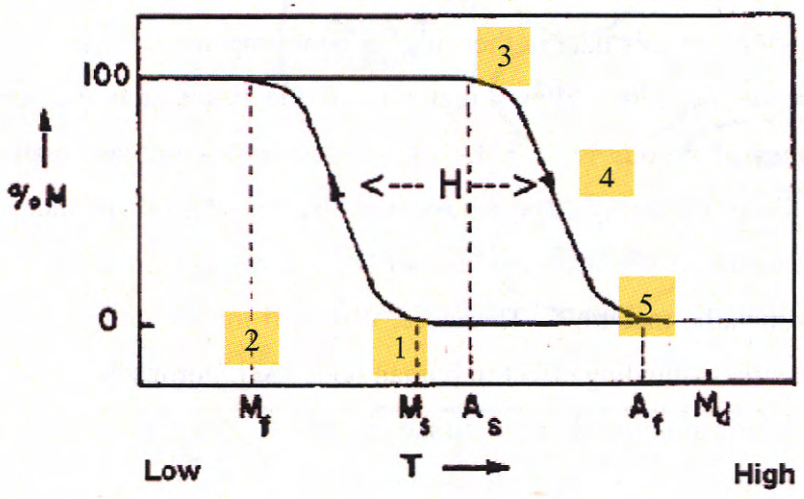

Figure 2.2 Illustration on thermal transformation hysteresis loop T= temperature Vs % M= martensite percentage of NiTi SME

2.2 Potential application for Porous NiTi (SMA)

NiTi alloy offers unique properties (SMAs) which attracted great interest in various fields of applications ranging from aerospace and naval [22] to surgical instruments and medical implants and fixtures [23]. The SMAs have been used in coupling devices, microactuation of microelectromechanical systems (MEMS) [24], actuators in a wide range of applications as well as in medicine and dentistry. These applications have mostly benefited from the ability of the inherent shape recovery characteristics of SMAs. In addition to the shape memory and pseudoelasticity effects that SMAs possess, there is also the promise of using SMAs in making high-efficiency damping devices that are superior to those made of conventional materials, partially due to their hysteretic response.

Driven by biomedical interests, recent emphasis has been given to porous NiTi. The possibility of producing NiTi in porous form opens new fields of application, including reduced weight and increased biocompatibility. Since 1950s, porous biomaterial such as bio-polymers, bio-ceramics, bio-glasses and bio-metals were of growing interests and had other potential for future biomaterial applications [25]. Perhaps the most successful application of porous SMAs to this date is their use as bone implants [11, 26-31]. In addition, the porous structure of the alloys allows ingrowth of the tissue into the implant [25, 29, 32]. The advantages of porous NiTi SMA over other porous implant materials are as follows: (1) greater biocompatibility, (2) great fixation efficiency, (3) shape memory effect (SME), and (4) superelasticity. The elastic modules of NiTi were reported near to human bone as compared to other metallic materials. Therefore, very stiff metallic implant such as stainless steel will result in stress-shielding effect in human body [33]. Porous NiTi also can be used as scaffolds for cell spreading and new tissue ingrowth once implanted into living tissues for reconstructive surgery [34]. These numerous benefits have catalysed the recent research [4, 27, 35-38] on the application of porous NiTi SMAs biomedical usage.

Another potential application for porous NiTi SMA is as an effective damper. It does this by utilizing the energy absorption capabilities of the material. It has been demonstrated that a significant part of the impact energy is absorbed and thus able to carry significant loads [39]. Beyond the energy absorption capability of dense SMA materials, porous SMAs offer the possibility of higher specific damping capacity under dynamic loading conditions. The reason for such high-energy absorption is the sequence of forward and reverse phase transformations

in the SMA matrix. In addition to the inherent energy dissipation capabilities of the SMA matrix, it is envisioned that the pores will facilitate additional absorption of the impact energy due to wave scattering.

Functionally graded SMAs material can be develops by controlling and manipulating suitable porosity in the material. Thus, this will cover a wide spectrum of functional operation principles which then offer a large variety of application fields [40]. Figure 2.3 shows several applications fields according to the different types of morphology in metal. For example, if porous NiTi SMA consists of open pores, it can be use as a biomaterial because its porous structure favours ingrowth of the tissue into the implant. On the other hand, if the porous SMA consists of closed pores, then it can be used in energy absorbers or load-bearing.

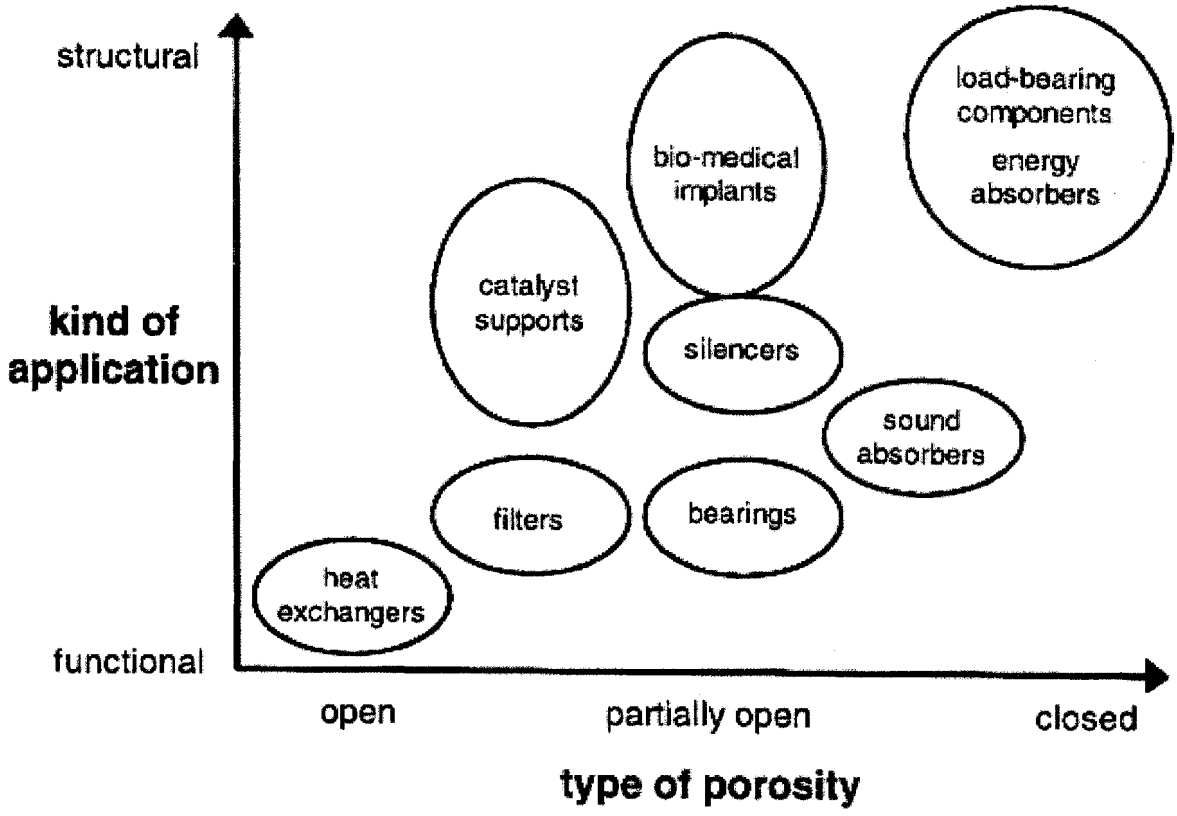

Figure 2.3 Different varieties of applications in terms of various types of porosities.

2.3 Recent developments in manufacturing porous NiTi SMA.

The first porous NiTi was probably produced in 1994 by V.I Itin et. al.[11]. In 1999, Gyuther [41] successfully patented the porous NiTi article. This was then followed by several investigations using sintering, hot isostatic pressing (HIP), spark plasma sintering (SPS) and

self-propagation high-temperature (SHS) to manufacture a porous NiTi SMA [2-4, 27, 35-38, 42, 43].

2.3.1 Sintering

Sintering process undergoes a densification of powder compacts at temperature below melting point of the powder. The shrinkage occurs as the pores between the particle decrease in size until they are eliminated. The driving force of the sintering process is the reduction of surface energy. The sintering principle is base on densification method involving removal of the pores between the starting particles combined with coalescence and strong bonding between adjacent particles were used to produce porous part. Thus ironically it is used to produce a porous parts. Hence, in order to introduce pores in the material, pore forming agents such as titanium hydride (i.e.TiH_2) were used. This will evolve hydrogen when heated to a sufficiently high temperature which then generated pores in the material.

2.3.2 Hot isostatic pressing

Hot isostatic pressing (HIP) is a manufacturing process that involves simultaneous application of high temperature and pressure. Originally, the main reason of using this process over other convectional process is that the powders are able to be consolidated to higher densities at a lower temperature. However, Ishizaki [44] had succeeded in developing a capsule-free HIP process to make porous ceramic materials which is different from the traditional capsule HIP. Powder compacts are sintered directly under highly pressurized gas. High open porosity can be obtained through this process at high sintering temperature due to the densification of powder compacts, which are delayed by high-pressure gas.

2.3.3 Spark plasma sintering (SPS)

Traditionally, SPS is used to sinter ceramic powders quickly to its full density at a relatively lower temperature compared. In the SPS process, uniaxial pressure is applied on the compacted material powder during sintering. A pulsed dc current is used simultaneously with a pressure to primarily sinter powders and activation of powder particles is achieved by the application of electrical discharges. Recently, porous NiTi rod were processed by spark plasma sintering (SPS) [45].

2.3.4 Reasons for employing SHS process as compared to other conventional methods (sintering, HIP and SPS) for producing porous NiTi.

Conventionally, Sintering, HIP and SPS are involved in compacted material powder and sintered into a desired dense shape form. For past several years, the problem of macro-micro porosities present in the material produced by these conventional methods is what many researchers trying to solve. However due to the porous material attracted great interest in various fields of application (ref. section 2.2), there have been some attempts to design and process porous NiTi, but the porous NiTi in the earlier works proved to be unsatisfactory. These conventional methods are not been able to manipulate pores size and eliminated unreacted Ni in the final product. Single phase or reducing secondary intermetallic phases are still constantly found in the final sintered parts. In addition it has difficult to achieve the homogenous pores in the final product. On the other, SHS process has shown the ability to create porous NiTi parts rapidly and affordable.

Thus, the reasons for employing SHS process over conventional methods can be summarized as follows [1, 46]:

1) The simplicity of the process avoids the need of expensive process facilities and equipments.
2) The rapid exothermic reaction process leads to time and cost saving in operating and process.
3) The higher purity of products can be obtained by this method. This is because the process associated with the combustion wave and the volatile impurities has low boiling point temperature that are expected to be expelled as the wave propagates through the sample.

4) The possibility of obtaining complex or metastable phases. This is based on the high thermal gradient and the rapid rate of cooling associated with the combustion process.
5) SHS process has the ability to manipulate the pore morphology within the porous NiTi by changing its combustion temperatures.

2.3.5 The secondary intermetallics phases: Ti_2Ni, $TiNi_3$ and Ni_4Ti

An examination of the Ni-Ti binary alloy diagram shows three neighbouring stable intermetallic phases of Ti_2Ni, $TiNi_3$ and Ni_4Ti. It was reported [3] that Ti_2Ni phase can induce brittleness to the final product and subsequently lead to cavitation corrosion of porous NiTi SMA in the physiological environment. The Ni_4Ti phases affect the martensite transformation in supporting the formation of the R-phase and affecting the Ni-content of the matrix [47]. Therefore, the synthesis and processing method for porous NiTi should take into account the above considerations.

2.3.6 Self-propagating high-temperature synthesis (SHS)

The combustion synthesis/reaction sintering such as SHS was employed in this work. It is also known as solid-flame combustion. SHS has offered wider advantages as compared to convectional PM (e.g. sintering). With SHS process, pore structure, morphology, and combustion temperatures can be manipulated. It is also possible to achieve a functionally graded material. The process is rapid, simple and avoids the need for expensive process facilities and equipment [1].

2.3.7 History of SHS

The earliest record in the literature for using combustion synthesis dates back to 1825 in the synthesis a ceramic refractory material. Later in 1885 [1], Goldschmidt used highly exothermic of metal oxide (i.e. chromium, manganese, molybdenum, iron, titanium and zirconium) to react with aluminium. The process was then described as a " thermite reaction, a metallic compound is reduced by one of several metal of metallic alloys in such a way that when mixture is ignited at one place, the reaction continues on its own accord" [1].

In the 1940s and 1950s, several American scientists [1] carried out this combustion synthesis research (although it was not called this). They found that calcium metal ingots could be converted to hydride by an exothermic process synthesized with nitride metal whereby intermetallic compound calcium nitride was obtained. Walton [1] applied the self-propagating principle by inserting a piece of magnesium ribbon as an ignitor into a power mixture of aluminium and phosphorus to produce aluminium phosphide. Later in 1964, Krap [1] introduced a process called the chemical hot press. This process was carried out using an electrical current through a mixture of powders in a die of a press. Once ignited, exothermic reaction was self-sustained

Since 1976, more than 30 different institutes and universities in Russia (i.e. former U.S.S.R) have been engaged in SHS research and development. An unsupported research in former Soviet Union began a systematic investigation on fundamentals, methodology, and ideology of SHS research [48]. It was then that the SHS research became more analytical of which the scope of the study was extended to the mechanism of heat transfer, chemical reaction and kinetics of SHS reaction. The term "structural macrokinectics" which is the study of the relationship between the direct and indirect chemical reaction rate, heat and mass transfer and structural transformation during the SHS combustion reaction were then introduced. Through extensive of analytical research, three basic conditions must be met to produce a self-propagating reaction were established [49]:

1. The reaction must be strongly exothermic and a heat of reaction on the order of 167.432 kJ/mole is generally enough.
2. A liquid phase should form during the reaction to enhance diffusion such that the optimum condition occurs when the calculated adiabatic temperature is at or above the melting point of the desired product. When calculated adiabatic temperature is less than the product melting point, preheat is necessary unless a low-temperature eutectic exists.
3. The rate of heat dissipation must be less than the rate of heat generation, or else the reaction will be quenched. Heat dissipation is largely affected by particle size, bulk density, and surface/volume ratio. A study [1] found that the relationship between the adiabatic steady-state velocity V_{ad} and the velocity prior to quench out V_m was:

$$V_m \approx \frac{V_{ad}}{1.65} \tag{2.1}$$

Where V_m is the critical velocity at which the combustion process is on the verge of being quenched out.

2.3.8 Introduction to Self –Propagating High Temperature Synthesis [SHS]

The SHS process offers new possibilities of producing advanced materials, such as ceramics, composite materials, and intermetallic compounds. This synthesis reaction is a highly exothermic and as such the reaction is self-sustaining. Once enough heat is generated, the reaction will sustain after its initiation. There are two different modes: combustion wave and thermal explosion. The combustion wave mode is initiated at one end of the sample by means of an external energy source (i.e. heated coil/wire, electric spark, laser beam, etc.) and proceeds through the reactant mixture in the form of a propagating combustion wave. This combustion wave travel at a velocity ranging from 0.1 to 25 cm/s [50]. Table 2.1 tabulates the typical parameters value of SHS. The thermal explosion method or simultaneous combustion mode involves a method of heating up the whole entire sample up to a temperature at which the reaction becomes spontaneous and simultaneously throughout the volume. This mode is usually for weakly exothermic system, which requires preheating prior to ignition [1]. Both of these combustion synthesis modes are illustrated in Figure 2.4.

Table 2.1 A typical parameters of SHS [48]

Burning velocity	0.1-20 cm/s
Combustion temperature	2300-3800 K
Heating rate	10^3-10^6 K/s
Igniting flux	10-200 cal/cm^{2}s
Induction time for ignition	0.2-1.2 s
Ignition temperature	800-1200 K

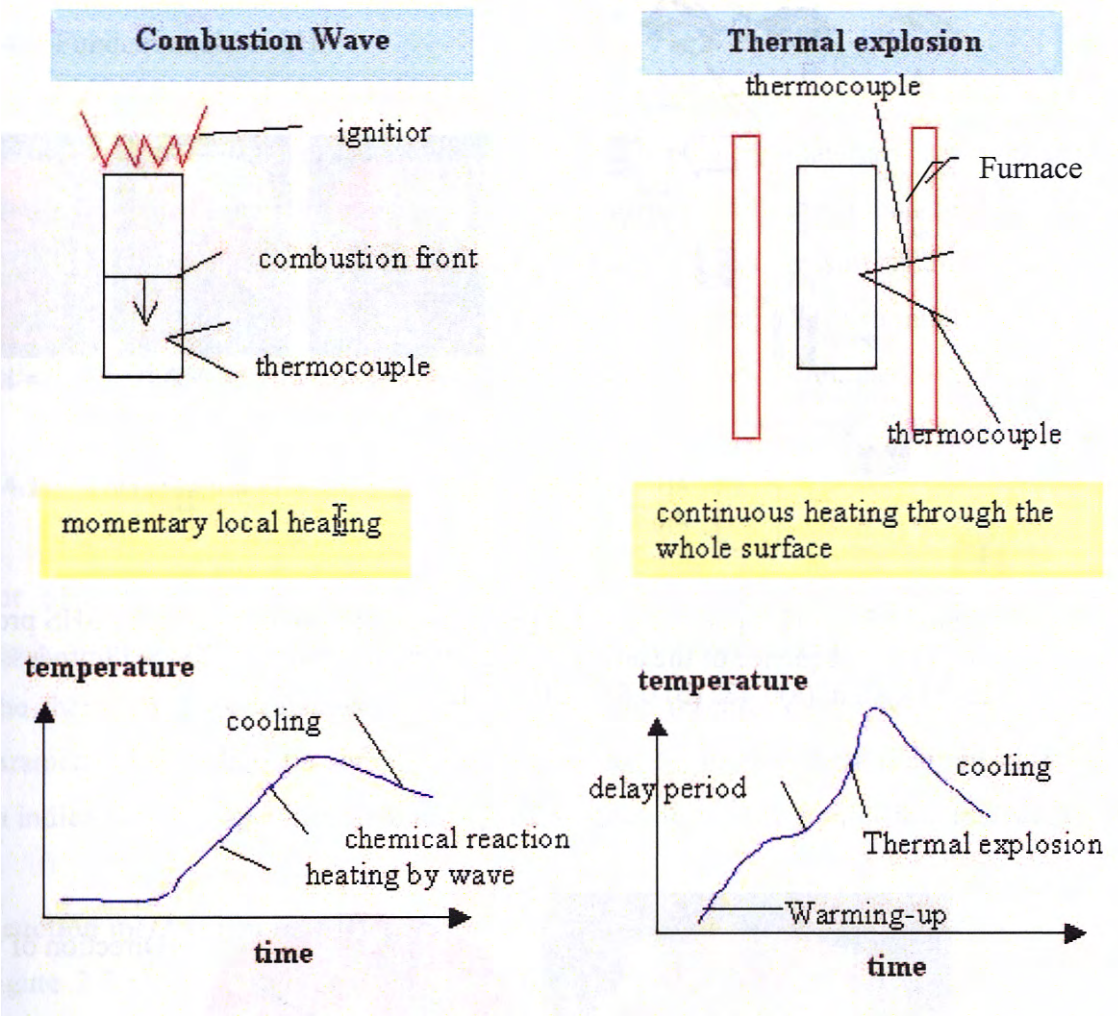

Figure 2.4 The two different modes of SHS process: the combustion wave (autowave process) and thermal explosion (induction process) [48]

SHS can be carried out on a fine powder, thin film, liquid and gases. However, most of the process favours using powder mixture (loose or pellet) form. Figure 2.5(I) shows a typical experiment procedure of SHS process using pellet sample by cold compacted prior to SHS process. This process can be operated in vacuum, open air and inert or reactive gas environment [48]. A photographical example of combustion synthesis in wave combustion mode on Ni-Ti system is shown in Figure 2.5(II). Figure 2.6 illustrates a schematic representation of the SHS process and propagation wave.

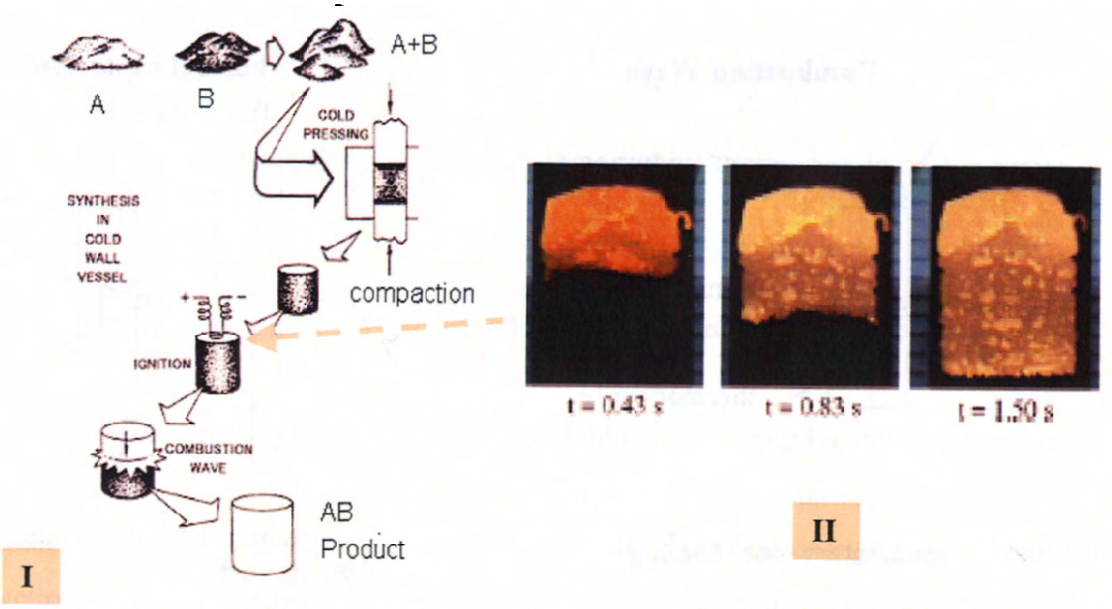

Figure 2.5 (I) Schematic drawing of combustion synthesis by the SHS process [51] (II) A sequence of the advance of a combustion wave in the SHS process for Ti–Ni system (a)0.43s (b) 0.83s (c)1.50s [5].

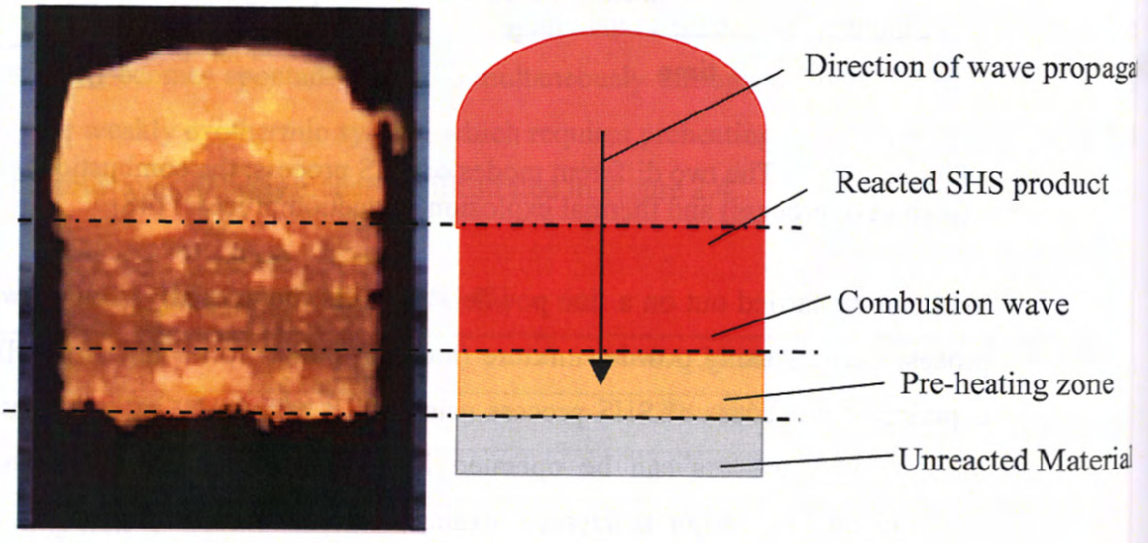

Figure 2.6 A schematic representation of the SHS process and propagation wave through a powder compact.

2.4 Fundamentals of SHS

Fundamentals for this process involves thermodynamics, materials science, combustion theory, chemical kinetics and structural macrokinetics, and other allied fields of knowledge [48]. Process parameters include thermal conductivity, gas pressure ignition mode, ignition temperature, initial temperature (the preheating temperature, combustion temperature, heating and cooling rates) and physical conditions of reactant (solid, liquid, gas).

2.4.1 Thermodynamics

For SHS reactions, thermodynamic calculations can help to predetermine the adiabatic combustion temperature or both the combustion temperature and product composition [48]. The thermodynamic calculations are based on the reaction enthalpies. The main principal parameter is the adiabatic combustion temperature T_{ad} in this reaction combustion. It shows an indication of temperature attained by the product during the combustion reaction process.

Reaction mechanism on SHS process

Figure 2.7 shows a typical temperature–time plot of schematic representation for the SHS process. This process is required to be highly exothermic in order to be self-sustaining and hence energetically efficient. The exothermic reaction is initiated at the ignition temperature T_{ig} and generates heat at maximum/combustion temperature T_c.

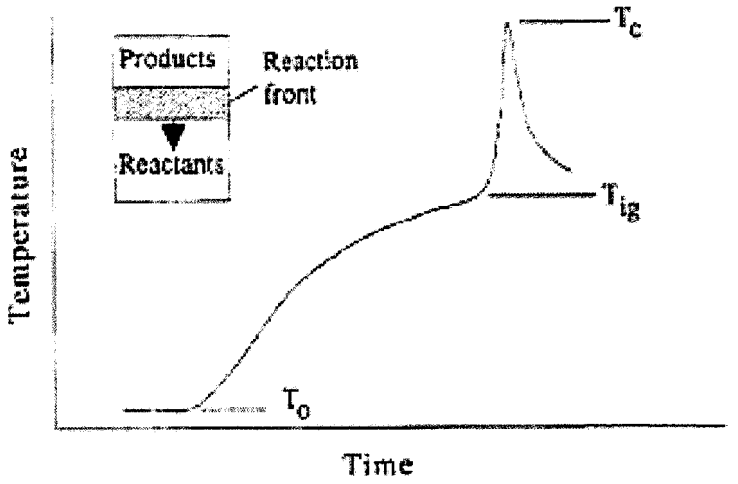

Figure 2.7 The schematic representation of the temperature-time during an SHS reaction [1].

There are four important temperatures which may affect the process of the reaction and final product:

1. The initial temperature, T_0, normally refer as preheating temperature that is the average temperature of the reactant sample before the reaction is ignition in the propagation mode
2. The ignition temperature, T_{ig}, that represents the point at which the SHS reaction is dynamically activated without further external heat supply
3. The adiabatic combustion temperature, T_{ad}, that is the maximum combustion temperature achieved under adiabatic conditions.
4. The actual combustion temperature, T_c, that is the maximum temperature achieved normally under non-adiabatic conditions.

Thermodynamic considerations in SHS process for NiTi system

The thermodynamic calculation can predict the ability to ignite or initiate a certain combustion reaction. This will obtain the optimum preheating temperature based on the reaction enthalpies. In this reaction combustion, the main principal parameter is the adiabatic combustion temperature, T_{ad}. This temperature shows the temperature attained by the product during the combustion reaction.

For example:
Consider the reaction between Nickel, *Ni*, and Titanium, *Ti*, to produce the intermetallic compound *NiTi*. Then the expression can be shown as:

$$Ni + Ti \rightarrow NiTi \tag{2.2}$$

Thus the enthalpies required for the reaction at 298 K are:

$$\Delta H_{reaction,NiTi} = \Delta H_{f,NiTi} - (\Delta H_{f,Ni} + \Delta H_{f,Ti}) = \text{-67.781 KJ/mol} \tag{2.3}$$

Where

ΔH_f – refers as changes (absorbed or evolved) of enthalpy of formation in the system

subscript – refers as system e.g. Ni is nickel

In order to achieve the condition above, the law of conservation of energy needs to be established. Therefore, the enthalpy of reactant $H(R)_{To}$ (i.e. *Ni* and *Ti*) at the initial temperature, T_0, must be equal to the enthalpy of the product $H(P)_{To}$ (i.e. *NiTi*) at adiabatic temperature, T_{ad}, as shown in Figure 2.8 (black line). The sum of the reactant and product s' enthalpy will generate heat of combustion reaction process at ignition temperature (T_{ig}), thus the heat of the reaction $\Delta H\ (T_{ig})$ are:

$$\Delta H(T_{ig}) = -[H(R)_{To} + H(P)_{To}] \tag{2.4}$$

When the initial (green) reactant mixture is at initial temperature, T_0, it only will ignite at T_{ig}. Thus the amount of heat needed for reactant R from T_0 to T_{ig} during the exothermic SHS reaction will be:

$$H(R) = \int_{T_0}^{T_{ig}} \left(\sum n_i C_p(R_i)\right) dT + \sum_{T_0 - T_{ig}} n_i L(R_i) \tag{2.5}$$

where

$C_p(R_i)$ - The heat capacity of the reactant

$L(R_i)$ - The phase transformation enthalpy of the reactant

subscript i - Refers to solid or liquid phase of reactant

The relationship between the *H-T* illustrates in Figure 2.8 under the condition given by equation (2.4). If the initial temperature of the reactant T_0 (i.e. pre-heating) increases to T_{ig}, it will decrease the enthalpy of reactant $H(R)$ and increase the enthalpy of product $H(P)$ (blue line in Figure 2.8). In other words, preheating the reactant can be used to increase the combustion temperature (i.e. T_{ad} to $T_{ad}(T_1)$ from black dotted to blue dotted line) for low exothermic reaction. Li et. al. [4] and Yeh et. al. [5] showed significance influence on the preheating temperature at or above 200 °C and 100 °C respectively improved the combustion temperature in the SHS porous NiTi. The further increased from T_0 to T_{ig} will decrease $H(R)$ to zero and all of $\Delta H(T_{ig})$ and will be available to be absorbed by the products which resulting in an adiabatic temperature of $T_{ad}(T_{ig})$. Hence, under this condition the reaction is ignited under simultaneous combustion. The heat loss ΔQ from the reaction front corresponding to the difference between measured the T_c and the calculated T_{ad} is indicated in Figure 2.8.

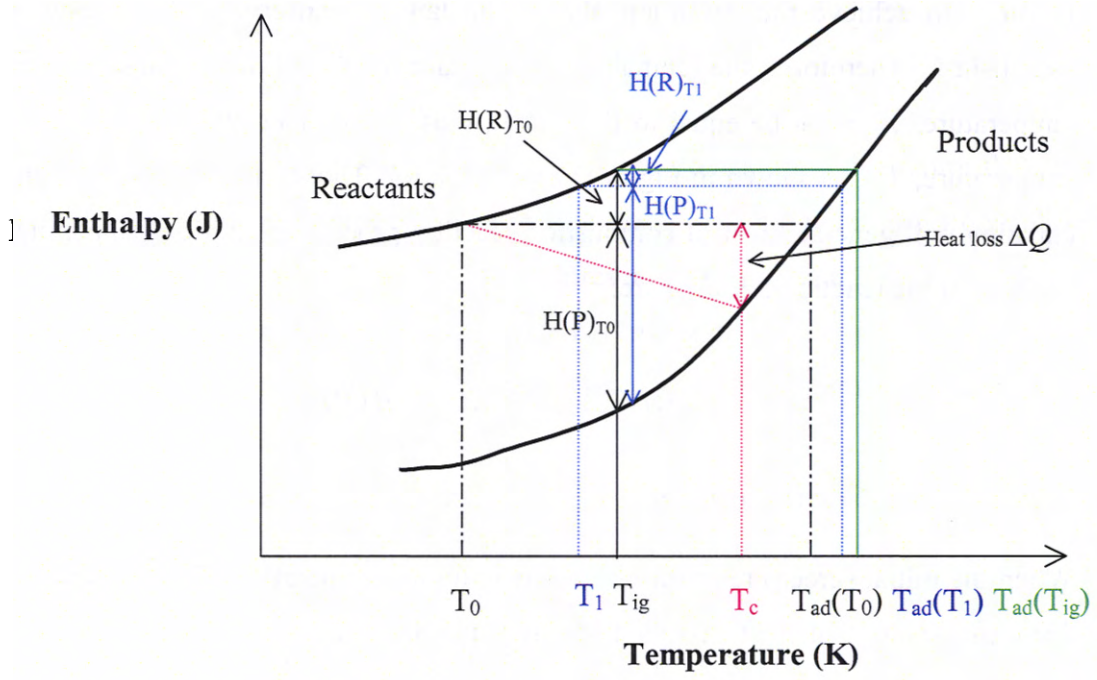

Figure 2.8 Schematic representation of the enthalpy-temperature plot for reactants and products in a reaction system that involves no phase change in reactants and products

The adiabatic temperature can be calculated from the heat released during the reaction of Ni-Ti system. Thus, this expression can be shown in the following:

$$\Delta H^0 = \Delta H_f^0(T_o) + \int_{T_o}^{T_{ad}} C_p(p)dT \qquad (2.6)$$

where

H_f^0 - is the enthalpy of formation of the intermetallic compound of *NiTi* at temperature T_0

$C_p(p)$ – is the heat capacity of the product *NiTi*

Under condition of rapidity reaction, it is reasonable to assume the combustion reaction is pseudo-adiabatic i.e. $\Delta H^0 = 0$. Then the equation (2.6) will become if $T_{ad} < T_m$

$$-\Delta H_f^0(T_0) = \int_{T_0}^{T_{ad}} C_{p_s}(p)dT \qquad (2.7)$$

where

T_m - is the melting point of the compound *NiTi*.

ΔH_m -is the heat fusion of the *NiTi*

ν -is the melting fraction of *NiTi*

$C_{ps}(p)$ - is *NiTi* heat capacities in the solid phase

$C_{pl}(p)$ - is $NiTi$ heat capacities in the liquid phase

Then if $T_{ad} = T_m$:

$$-\Delta H_f^0(T_0) = \int_{T_0}^{T_m} C_{p_s}(p)dT + \nu\Delta H_m (0 \le \nu \le 1) \tag{2.8}$$

If $T_{ad} > T_m$:

$$-\Delta H_f^0(T_0) = \int_{T_0}^{T_m} C_{p_s}(p)dT + \Delta H_m + \int_{Tm}^{T_{ad}} C_{p_l}(p)dT \tag{2.9}$$

In addition the enthalpy of formation of the intermetallic compound of $NiTi$ at temperature T_0 can be also calculated from

$$\Delta H_f^0(T_0) = \Delta H_{f,298}^0 + \int_{298}^{T_0} \left\{ C_p(NiTi) - [C_p(Ti) + C_p(Ni)] \right\} dT \tag{2.10}$$

Therefore, the adiabatic temperature T_{ad} at a certain preheating temperature can predetermined by using above equation (2.7)(2.8)(2.9). A schematic depiction of this process is show in Figure 2.9.

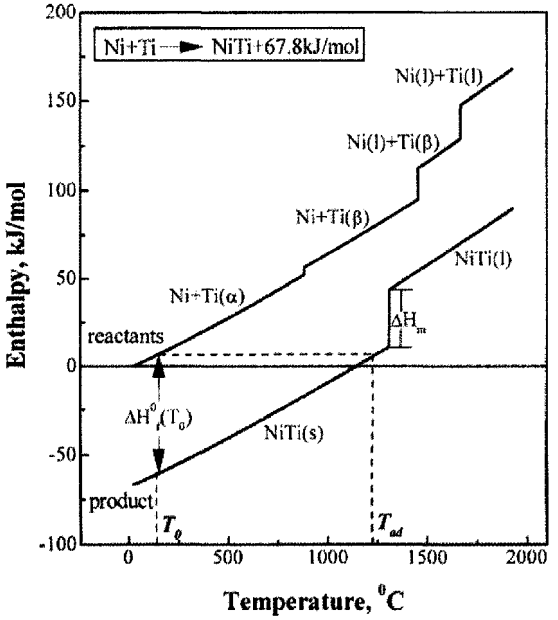

Figure 2.9 The enthalpy-temperature diagram for the NiTi system [4]

The influence of preheat temperature T_0 on adiabatic temperature T_{ad}

Figure 2.10 shows the influence of the preheating temperature T_0 on adiabatic temperature T_{ad}. The graph is established by calculations according to equations (2.7)(2.8)(2.9). The thermodynamic data are taken from [52]. The T_{ad} increases as it reaches T_0 of 227 °C. Further increase of T_0 results in T_{ad} maintaining a constant temperature until T_0 reaches 750 °C. Further increase of T_0 after 750 °C will increase the T_{ad}. The plateau between the preheating temperatures of 227 °C to 750 °C exists as T_{ad} reaches the melting temperature of NiTi compound and the melting fraction increases almost linearly with increasing T_0. The inset graph in Figure 2.10 shows a completed melting between the T_0 of 227 °C to 750 °C.

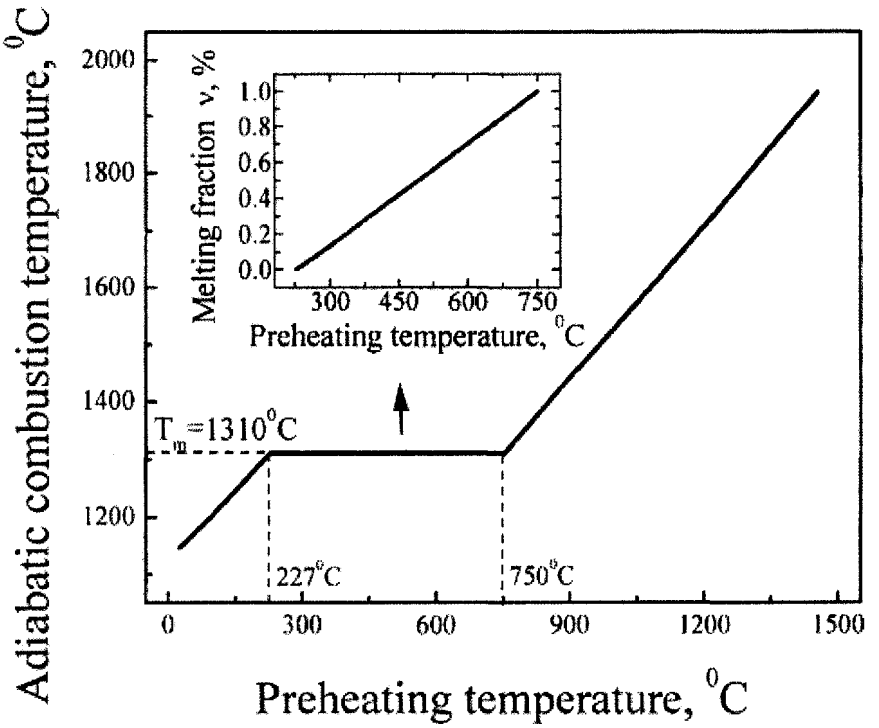

Figure 2.10 The calculated adiabatic combustion temperature Vs preheating temperature [4]

The method of using preheating temperature on reactant only has influence on the combustion temperature. This has also subsequently changed the whole morphology of pores and phase transformation in the as-SHS final product. Li et. al. [4] had demonstrated the effect of different preheat temperatures on pore structure of porous NiTi as shown in Figure 2.11. In Figure 2.11, the final as-SHS porous product with preheating temperatures above 300 °C obtained pores in a linear-alignment along the propagating wave direction. However in the phase analysis on final as-SHS, no significant improvement was made with increasing preheating temperature in this study. The presence of secondary unwanted intermetallics (i.e. Ti_2Ni, Ni_3Ti and Ni_4Ti) still remained in the final porous NiTi. Recently, Yeh et. al.[5] had produced NiTi part by SHS. Similarly, the reaction parameter such as preheating temperature

was used to improve the phase formation in the final NiTi product. In his finding, the presence of unreacted Ni and other secondary intermetallic were eliminated and reduced at preheating temperatures of 200 °C and 300 °C respectively. Nevertheless, too much melting phase was formed and produced a dense NiTi phase.

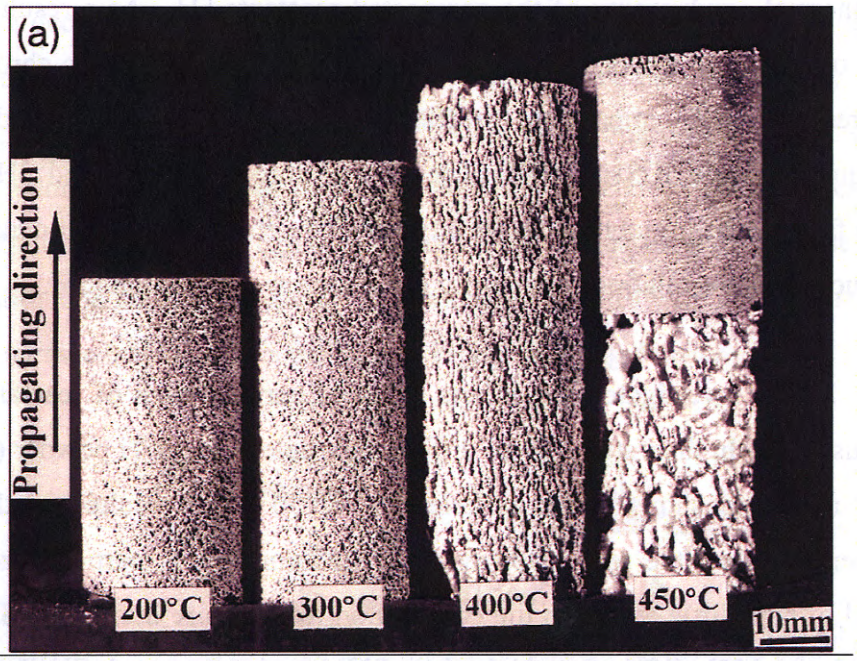

Figure 2.11 Macrograph on Porous NiTi by SHS at four different preheating temperatures

2.4.2 Materials Science

The fundamentals of material science were necessary for the characterization of SHS specimens, since the SHS process is done using powder mixture by cold compaction. Therefore processing parameters related to the powder such as chemical composition of reactant, reactant particle shape and size, green density during compaction stage and ignition techniques inevitably will affect the SHS reaction. Many of these parameters are interdependent on one another and contribute significant effects on the final product morphology and properties.

Particle size and shape of reactant

The shape of the particle can influence packing, flow and compressibility at compaction stage [53, 54]. The size and shape of the particle will influence the green density, green pore size and thermal conductivity of the compacted reactants [1]. As a result, the particle size will have on effect on the degree of completeness of the reaction, the chronological sequence of the reaction, the temperature profile of the combustion zone and the velocity of the combustion wave of SHS [55]. The general porosity of the final SHS product depends on three factors; the initial relative density, the difference in the molar density of the reactant and product and the evolution of impurity gases during combustion [55].

Li et. al. [4] investigated the effects using of particle sizes of reactants in SHS to produce porous NiTi. In their study, three different particle sizes of Ti powder (i.e. 5.2, 36.5, 67.2μm) were used and showed that particle size of 36.5 μm resulted in the lowest combustion temperature than the rest. However, the influence of Ti particle sizes in the reactant had found to have little effect on the combustion temperature during the SHS. In another study by Yeh et. al [5], different particle size of Ni powder was used. Similarly, They had found no significant effect on the SHS process of front propagation velocity. This was mainly due to the formation of eutectic liquid during the propagation of the flame-front. However, by decreasing Ni particle size from 43 μm to 5 μm, Yeh noted elimination of the unreacted Ni in as-SHS NiTi final products.

Influence of particle packing, flow and compressibility

The qualitative descriptors of various particle shapes are shown in Figure 2.12. Generally, a microscopy technique is the most appropriate technique to quantify shape. The distribution of the various particle size has effect on the packing density. This can be explained when smaller particles are distributed into the interstitial space between the larger particles, the packing density will increase and hence the porosity and pore size decrease significantly. However, when the mean particles size is 100 μm or below approximately, there will be increased interparticle friction and particle bridging is more likely to occur [54]. Another consequence of using smaller particle is the decreasing of packing density which due to increase of surface area, lower particles mass and greater significance of the short-range weak

forces such as electrostatic fields, moisture and surface adsorption. Hence, lower packing density with smaller particles increase resistance to compaction.

The particle shape and surface texture also contribute to interparticle friction, particles bridging and consequently packing density. For example, using mono-sized spherical shape will cause a decrease in packing density. On the other hand, using less roughness of particle surface (departure of shape from spherical) will improve packing density which eventually enhances green density during compaction. Also, by mixing different sizes of particles, green density of a compacted reactant is also enhanced [54]. Generally, to achieve higher packing density, vibration or lubricant can be introduced. However, these may cause problems such as agglomeration and size segregation. In summary, particles with smaller size, irregular shape and rough surface texture will contribute to higher packing density.

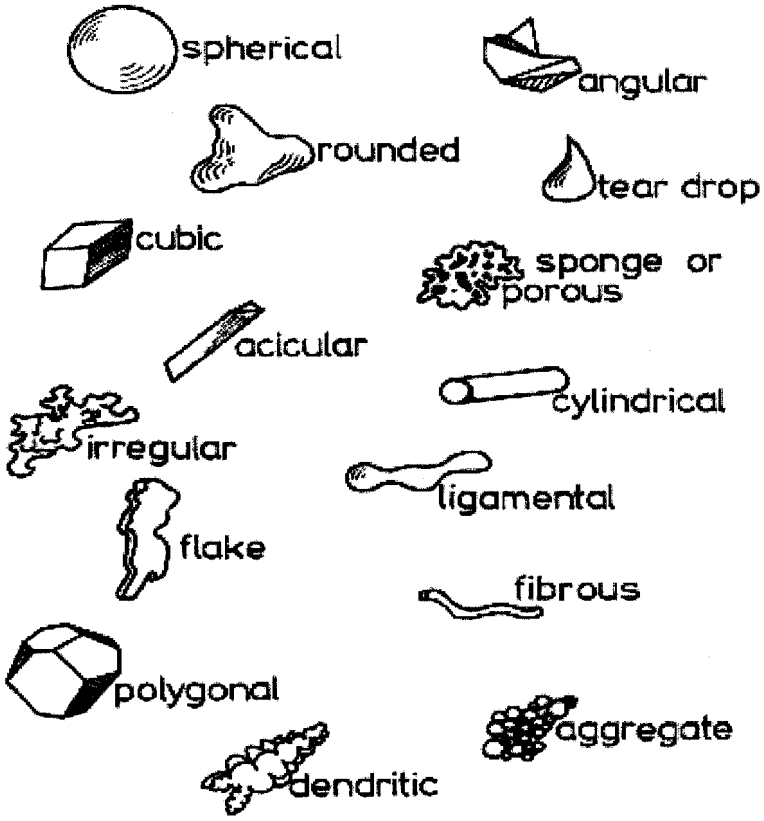

Figure 2.12 Qualitative description on various shape of powder particles [53]

Capillary mode

There are two main modes of combustion reaction in the SHS process such as the capillary mode and the diffusion mode. Figure 2.13 illustrates the capillary spreading was during the melting eutectic formation in SHS dominantly by capillary mode. The titanium particle started to melt and spread at the reaction zone to leave cavities (pores) in the final combustion product [49]. This phenomenon is related to surface energy occurring during liquid phase in the combustion synthesis. A study [1] was shown on the effect of particle size against volume and influence on capillary mode. In the study, it was concluded that the magnitude of the capillary force depends on the curvature of the liquid phase shape form, the surface energy and the liquid volume fraction. The more curved the surface, the greater the attractive force. Thus, smaller volume of liquid gives a greater force. Likewise, higher surface energies increase capillary forces.

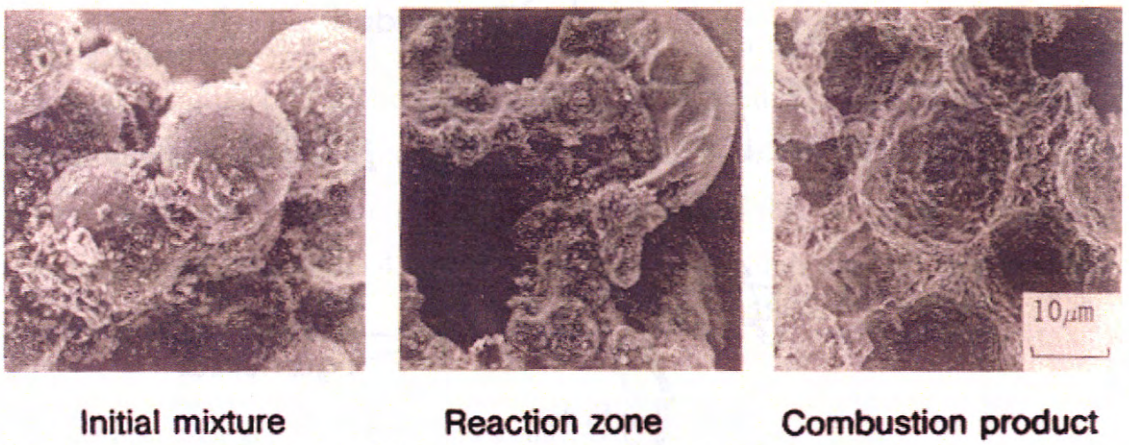

Figure 2.13 Micrograph of illustration on Capillary spreading take place in the titanium-carbon system [49]

Recently, Castillo et. al. [12] demonstrated the effect of gravitational force on the morphology of pores in the final as-SHS product as shown in Figure 2.14. Gravity plays a significant role in the structure and properties of materials produced by SHS. Low gravity produces classic grain growth phenomenon while the terrestrial environment yields long lamellar grains with characteristic spots as shown in Figure 2.14.

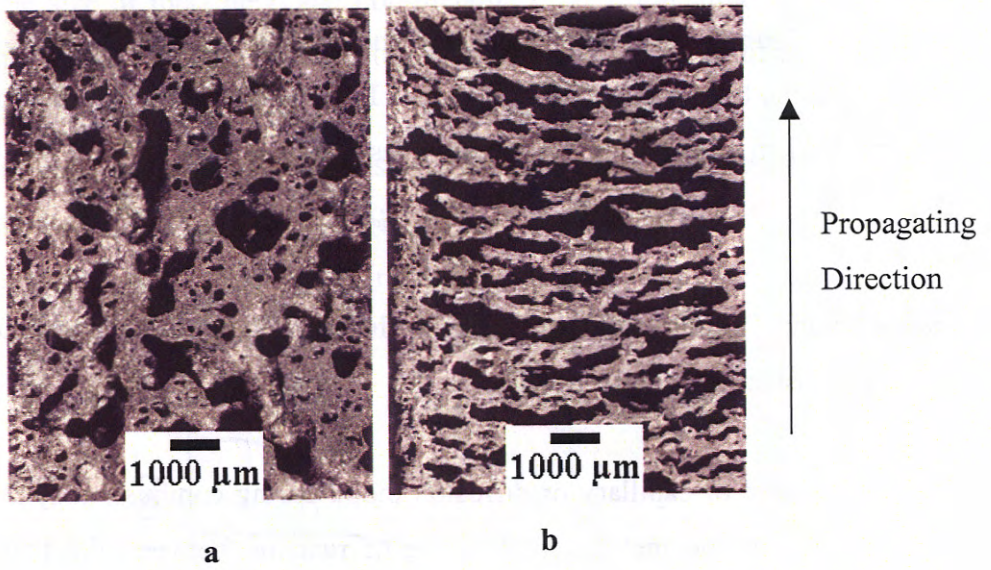

Figure 2.14 Effect of gravity on reaction system of 92% TiB and 8%Ti. (a) was produced in low gravity and (b) was produced in terrestrial (1 g) conditions

Diffusion mode

A study on SHS of Titanium-carbon system affirmed the co-existence of the two modes of combustion reaction: capillary action mode and diffusion mode [1]. In the capillary mode, combustion reaction is controlled by the rate of the capillary spreading of the reactant molten phase during capillary action mode. In diffusion mode, the combustion reaction is driven by reactive diffusion between the reactant. This diffusion mode occurs when the reactant particles do not melt during the combustion synthesis, i.e. solid-phase reaction takes place under the reactive diffusion mode. Taking as an example of the Ni-Ti reactant system in a gas-transport action of reaction diffusion as follow:

$$Ni_{soild} + D_{gaseous} \xrightarrow{T_1} (NiD)_{gaseous} \qquad \text{(Zone I)} \qquad (2.11)$$

$$(NiD)_{gaseous} + Ti_{soild} \xrightarrow{T_2} NiTi_{solid} + D_{gaseous} \qquad \text{(Zone II)} \qquad (2.12)$$

The temperature difference $\Delta T = T_1 - T_2$ is the driving force for the *Ni* solid to transfer from Zone I to Zone II. The exothermic and endothermic reaction of Ni_{soild} with gaseous carrier $D_{gaseous}$, at the temperatures is $T_1 > T_2$ and $T_1 < T_2$, respectively. To consider as one stage in the mechanism of solid phase reaction in gas-transport of SHS wave will be such as:

$$Ni_{soild} + Ti_{soild} \rightarrow NiTi_{soild} \tag{2.13}$$

Since Ni and Ti are metallic element, the chemical nature of both gaseous carriers may be by halogens instead of hydrogen [49].

The dominance of capillary or diffusion mode during combustion synthesis depends on the particle size of the metal. In the case of reaction between the titanium-carbon system theoretical analysis for diffusion-controlled mode and capillary action mode has been established [1]. In the diffusion-controlled mode, the theoretical analysis can be expressed when the particle size is small [1]:

$$r_0^2 << \sigma\lambda r_r \mu V^2 \ln\left[\frac{T_c - T_0}{T_m - T_0}\right] \tag{2.14}$$

Where

r_0 is the particle size of the starting reactant

r_r is the non-molten reactant

λ is the thermal diffusivity

σ is the surface tension of the liquid

μ is the viscosity of the liquid

V is the velocity of the combustion

Similarly, for capillary mode to be dominant, the reaction is characterized by:

$$r_0 >> \frac{\sigma r_r}{\mu D} \tag{2.15}$$

where

D is the diffusion coefficient of the reactant

The reactant particle size determines the reaction mechanism by controlling the velocity of the propagating combustion wave had shown in the previous theoretical analysis (i.e. eqn. (2.14

and (2.15)). In the similar titanium-carbon system, the dependence of the combustion rate V the particle size of metallic r_0 and non-metallic (r_1 r_2 r_3) at three different regions (kinetic, transition, capillary region) was illustrated in Figure 2.15. The diffusion-controlled mode is dominant in kinetic region (I), where V is independent with r_0. In the transition region (II), V significantly decreases as r_0 is increasing. However, the dependence of V on r_0 is relatively unsubstantial in the capillary region (III). Thus, in the capillary region, the combustion wave V decreases as the particle size of Ti (melting component) increases.

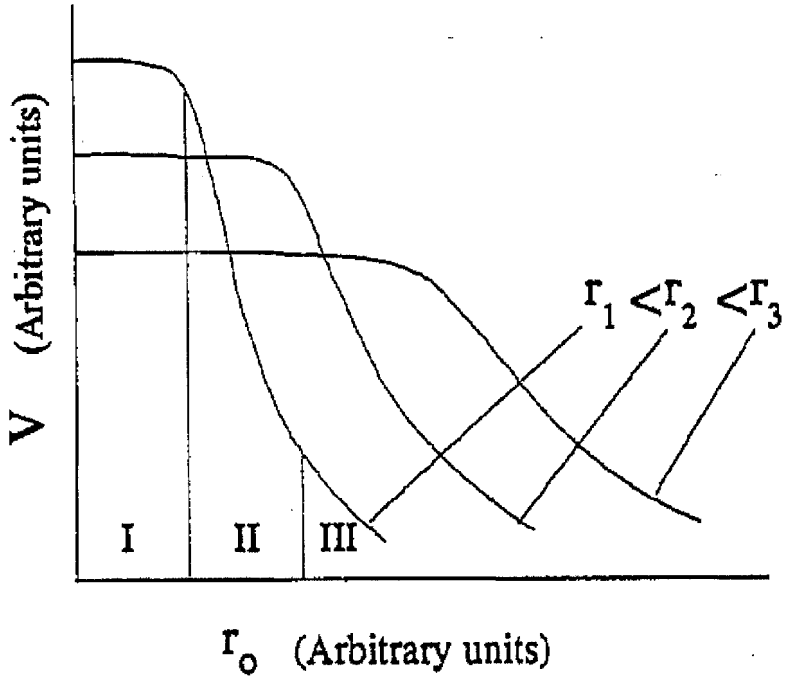

Figure 2.15 The correlation between the combustion rate and particle size of metallic (r_0) and non-metallic (r_1, $r_2$and r_3) reactant at (I) kinetic region;(II) transition region;(III) capillary region.

The compaction stage

During compaction stage, pressure is used to consolidate the powder with close dimensional control. This process involves both rearrangement and deformation of the particle, leading to development of the interparticle bond. This also means that compaction not only gives shape to the powder but also decreases the porosity and increases the coordination number of particle. Compaction is not a reversible process since the applied pressure modifies particle shape. Figure 2.16 shows a simplified view of the stages in compacting metal powder. At the initial stage, particles were rearranged and this increased number of contacts area between each other. With higher compaction pressure, particle undergoes plastic deformation. Thus,

the pressure causes localized deformation at the contacts points giving work (strain hardening and decreased contact distance between particles. Therefore, the increase of external pressure will provide better packing and leads to decrease in porosity.

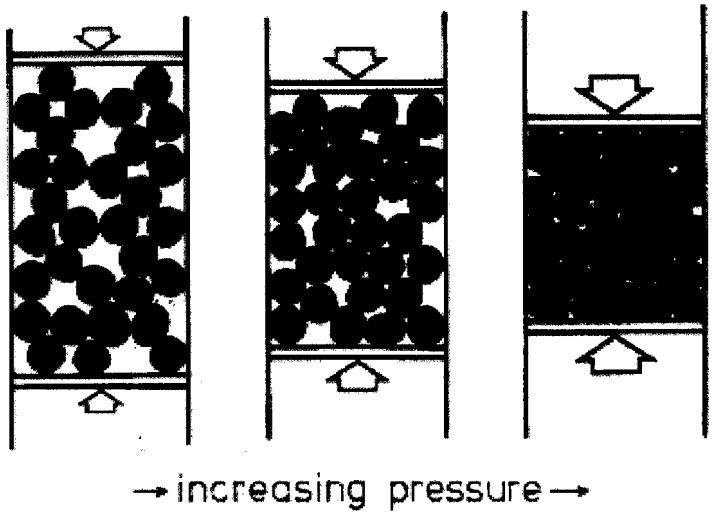

Figure 2.16 A diagram show on compaction stages with increasing pressure.

The theoretical analysis on compaction

The theoretical analyses on compaction stages can be done through taking into consider action a cylindrical compact of diameter D and height H as in Figure 2.17. dH is the compaction height with an external pressing force applied on it. This pressure forces consist the top pressure P and that is transmitted through the bottom pressure P_b. Mathematically the balance of forces can be expressed as follows:

$$\sum F = 0 = A(P - P_b) + uF_n \tag{2.16}$$

where

F_n: is the normal force

u : is the coefficient of friction between the powder and die wall

A: is the cross sectional area of the sample

Therefore

$$F_n = \pi zPDdH \tag{2.17}$$

where

z : is the ratio of the radial stress to the axial stress

And the friction force F_f is calculated directly from the F_n and the coefficient of friction as

$$F_f = uF_n = u\pi PDdH \tag{2.18}$$

By integrate the $dP = P\text{-}P_b$ with respect to dH can be obtained the pressure at any position x below the punch as shown:

$$\frac{P_x}{P} = \exp\left[-4uz\frac{x}{D}\right] \tag{2.19}$$

This equation (2.21) is applicable to single and double action compaction. Single action compaction refers to only one axial direction of external force compressed onto the compacted reactant where double action refers to two axial directions of external forces. However, for double action compaction, the distance x is refer to the nearest distance of the punch. From the equation (2.21) had shown that the pressure decay depend on the compact height to diameter ratio. With decreasing diameter, the pressure decreases more rapidly with depth. Hence, for homogeneous compaction small height to diameter ratios are desirable.

For single ended pressing, the average compaction stress is estimated as:

$$\sigma_1 = P\left(1-2uz\frac{H}{D}\right) \tag{2.20}$$

For double ended pressing, the average compaction stress is estimated as:

$$\sigma_2 = P\left(1-uz\frac{H}{D}\right) \tag{2.21}$$

Thus, from the both equations above show the average stress is dependent on the geometry (H/D), the interpatricle friction (z) and the die wall friction (u).

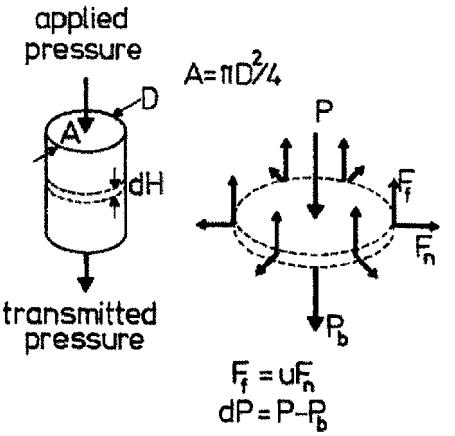

Figure 2.17 Diagram on the balance forces during die compaction

The height to diameter ratio of compacted reactant

The height to diameter ratio (*H/D*) is an important parameter to achieve uniform compac properties. Generally, when *H/D* exceeds five, the die compaction is unsuccessful [53] Figure 2.18 presents the approximate pressure distribution of compacted sample having *H/I* of 0.42,0.79,1.66 in a single action pressing of copper powder using constant compactio pressure of 700 Mpa [53].

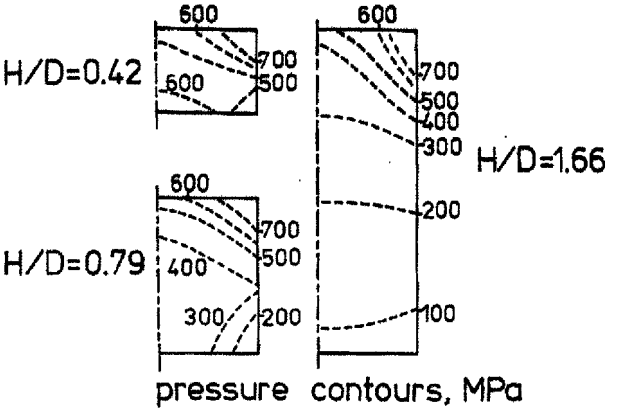

Figure 2.18 Pressure distribution in compacted copper powder cylinder on single acting compaction [53]

Figure 2.19 shows the density distribution plot in cylinders of compact copper powder fo single and double acting compaction. In single action compaction, the lowest density ha occurred at the compact bottom while in the double action compaction the lowest densit occurred at the centre of the compact.

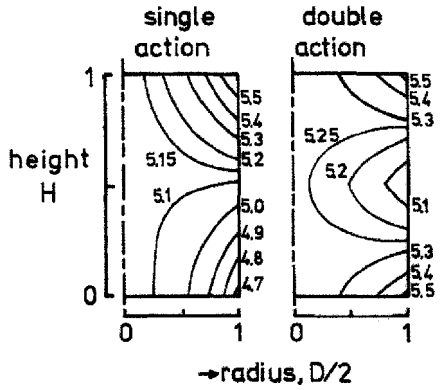

Figure 2.19 The constant density line in cylinders of compact copper powder for single and double acting compaction [53].

Effects on thermal conductivity of SHS by prior reaction parameters:

The compaction of the reactant (green powder) plays an important role in the combustion synthesis reaction. The previously mentioned parameters such as *H/D*, compaction pressure and single or double action compact have influences to the densities on the compact reactant. This initial reactant density is also known as green density. The compacted reactant with significantly high or low green density will cause the difficultly to ignite during SHS. In addition, the green density has influenced on the propagation of the reaction. The excessive contact between the particles will lead to too much heat loss at the reaction zone due to increase of thermal conductivity in the reactant particle [55]. The investigation of Yeh et. al. [5] shown that the green density of reactant had an influenced on the combustion temperature. In their result shown in Figure 2.20, the green densities of the reactant increased from 40% to 60% increased 30% of combustion temperature.

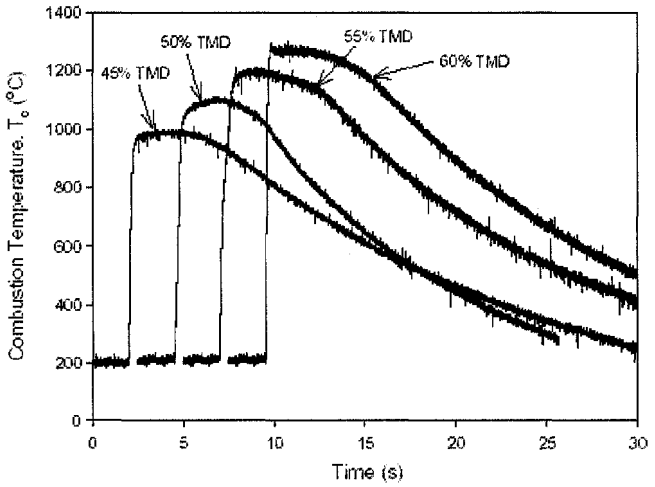

Figure 2.20 Effect of green sample density on combustion temperature in SHS of NiTi intermetallic [5]

Pre-compaction powder handling

The operation that occurs in pre-compaction is blending and mixing to combine a desire homogenous new composition. The mechanisms of powder mixing can be diffusion convection and shearing process. The volume of powder in the mixer determined the mixin efficiency. As the mixer becomes filled with powder, the relative motion of the powder i inhibited. Hence, powder volume between 20% and 40% of the mixer capacity is usuall optimal [53].

In a cylindrical mixer, the mixing efficiency varies with both the powder characteristics an the mixer operation characteristics. Low rotational mixing speed is inefficient because of litt motion. At high rotational speeds, the centrifugal forces can prevent mixing. The optim rotational speed for cylindrical mixer has been estimated by Sundrica [53]:

$$N_o = \frac{32}{d^{0.5}} \tag{2.22}$$

where

N_o is the optimal rate of ratio [RPM].

d is diameter of the cylinder mixer [m].

The ignition techniques

Currently, several ignition techniques were employed to ignite SHS reaction such as lase radiation, radiant flux, resistance heating coil, heated gas ignition spark and chemical oven etc. The most commonly used ones comprise a tungsten wire that produces heat through a electric discharge and ignites the mixture powder directly. The radiant flux is able to offer feasible standardizes the condition of ignition for each reaction. The ignition characteristi depended on the heat flux density, the reaction parameters and atmosphere pressure [1]. Thi approach of ignition is mainly on the radiation source, a reflector that is used to converge th radiation and a shutter which is able to controlling the amount of radiation. Another metho to ignite the reactant is laser. This type of ignition system is capable of achieving very hig heat flux densities (e.g. $> 10^{11}$ Wm^{-2}). The heated gas ignition is used to ignite metal powde in a hot gas oxidizer. In addition, microwave energy method was also used as an ignitio technique in SHS reaction. However, in most reaction system, the energy of microwave need

to be maintained because the volume of the adjacent unreacted mixture tends to increase as the propagation wave moves outwardly. The SHS process in thermal explosion mode (ref. Figure 2.4) are carried out at a constant pressure furnace and filled in an inert gas. The whole reactant sample are heated at a constant rate which in result in simultaneous combustion [1].

2.4.3 Combustion Theory and Chemical Kinetics

The characteristic of combustion theory is described in terms of wave propagation and wave structure. The latter is based on joint analysis of the equations of heat conduction with non-linear heat sources (i.e. heat release in chemical reaction) and chemical kinetics (i.e. ideal solid-flame combustion).

The kinetics of chemical reactions in SHS system provides information about the rate of heat release at high temperatures. The rate of the heat release can be obtained from the burning velocity on combustion temperature measurements and thermograms of combustion or electrothermal explosion whereas, similar data of the reaction of metal with gases can be measured from electrothermographic measurements[48]. In addition, the analysis calculations may also take into account the processes of melting and capillary spreading infiltration of a gaseous reagent (i.e. infiltration combustion), various heat transfer processes (i.e. heterogeneous combustion), etc [48].

Temperature profiles can be determined with instruments such as microthermocouple and optico-spectra. For SHS process, the exact value of the combustion velocity is not important. Hence, SHS temperature profiles reveal a quantitative study of different characteristics of combustion wave structure during the synthesis. There are four elementary patterns of SHS wave as shown in Figure 2.21. The type I is a classical case with narrow zone such that combustion wave consists of heated layer and react zone (Figure 2.21 I). Type II with has a wider zone of combustion which consists of two-subzones: propagation and postcombustion (Figure 2.21 II). The type III wave is still in chemical reaction stage. The chemical stage consists of two zones of which the first one is affected by the front propagation (Figure 2.21 III). Finally, the type IV wave was resulted from the phase transition during SHS. The temperature plateau results from the simultaneous action of the chemical reaction and phase transition (e.g. reactant melting) (Figure 2.21 IV). Figure 2.22 reveals the

combustion thermogram of Ti-Si system which encompass various wave pattern describ previously [49].

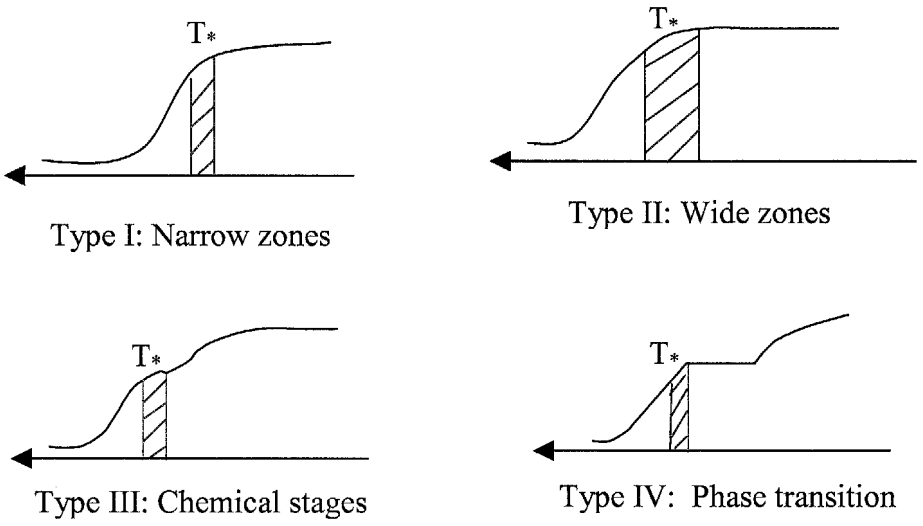

Figure 2.21 Different characteristic of temperature profiles of SHS waves where T* is the temperature affecting wave propagation

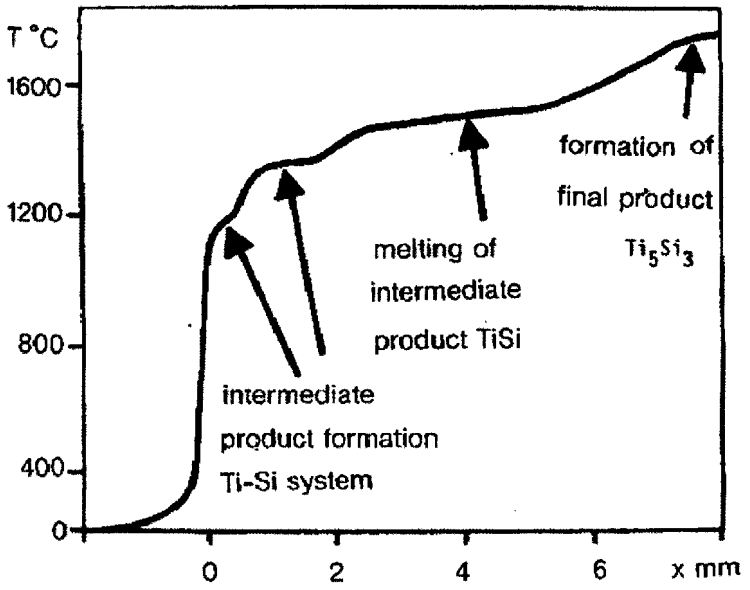

Figure 2.22 Thermogram of the combustion of the 5Ti + 3Si system [49]

2.4.4 Chemical and Structural Macrokinetics

The combustion theory has provided the foundation for better understanding and description of the SHS process. However, it does not describe the formation of the final state of SHS product (e.g. their phase composition, structure). The new scientific term "Structural Macrokinetic (SMK)" was originated to describe the SHS theory in consideration of combustion mechanism and processes of structure formation. Structural Macrokinetic studies the evolution of the medium structure during in course of chemical conversions taking into account of heat and mass transfer process. The concept of the final product formation in SHS process were analysed and developed into two mechanisms; equilibrium and nonequilibrium mechanisms as show in Figure 2.23.

Figure 2.23(A) presents a typical solid phase reaction at extremely low combustion in equilibrium mechanisms of SHS process. In this mechanism, chemical and structure transformation advance simultaneously in the common zone of heat evolution. Both of these chemical and phase compositions are form immediately behind the combustion front. However in the nonequilibrium mechanism as shown in the Figure 2.23(B), its chemical and phase composition transformations take place far behind the combustion front when the chemical reaction had been completed. The metastable phase of the final product structure were formed in the heat evolution zone. The nonequilibrium mechanism is regarded as the rapid SHS process. The experimental techniques were used to study these mechanisms such as motion pictures and video recording, thermometry, pyrometry, chemical analysis, XRD and metallography. In addition, it can be also used to investigate the mechanism of chemical, phase, and structure transformations in SHS reactions [48].

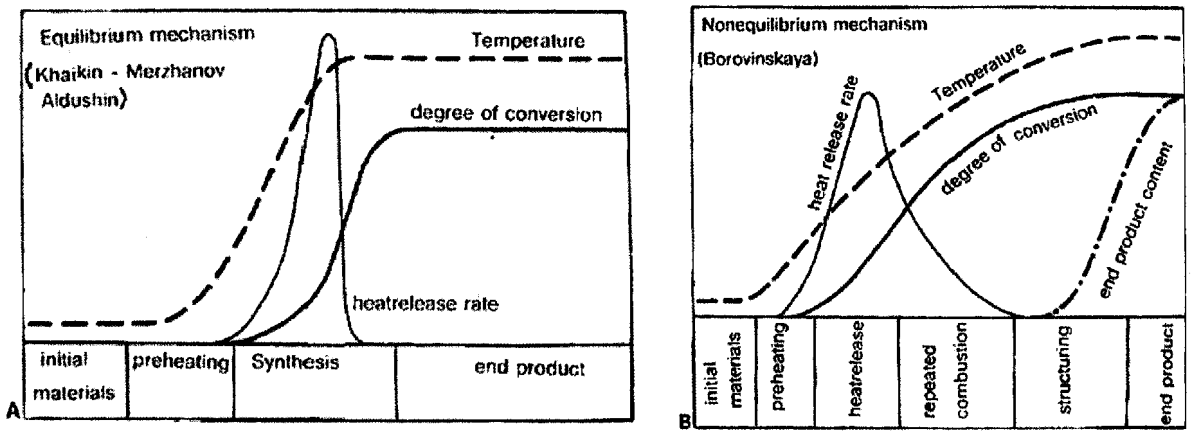

Figure 2.23 The adiabatic structure of combustion wave (A) equilibrium mechanism and (B) nonequilibrium mechanism [49].

2.5 The Experimental Approach Theroy

In material science and the solid-state progress, there are two main approaches that commonly apply: (1) developing and applying new methods for characterisation for materials (2) creating a novel materials with special structure feature and properties. In this study, the experimental approach is by creating special properties with new atomic structure and properties such as by the use of nanocrystalline material. Mechanically alloying process is intended to achieve a nanocrystalline material as a reaction agent far subsequent SHS process. Beside the atomic arrangement in the cores of defect such as grain boundaries, interphase boundaries or dislocations in the material, mechanical alloying also introduced new stored energy in the reaction agent.

Recently, the addition of nanocrystalline powder has shown advantages in SHS process. In Levashov et. al. [56] investigation, using nanocrystalline additive in titanium carbide showed a decreased combustion temperature and an increased physical and mechanical properties in the SHS products. As a result, an improvement of hardness and crack growth resistance in the SHS end-products. In the other research, the use of nano-scale nickel aluminide (i.e. NiAl) in SHS has shortened the time synthesis by half as compared to the micro-scale NiAl composite [57]. This recognition has generated a great interest on using of nanocrystalline powder as starting reagents and modifying additives. Therefore, using nanoscale additives incorporated with SHS is a potential key research direction to be explored.

2.5.1 Nanocrystalline materials

Nanocrystalline materials are single-phase or multi-phase material. These materials have a majority of crystals or grains of size usually in the order of few 1-100 nanometers. For many materials, the yield strength σ_y varies with grain size according to

$$\sigma_y = \sigma_0 + k_y d^{-\frac{1}{2}} \tag{2.23}$$

In the Hall-Petch equation, d is the average grain diameter, and σ_0 and k_y are constants for a particular material. This theory states that hardness increase is inversely proportional to the square root of the grain size. According to equation (2.23), if the grain size reduces to nanoscale, metal properties will get stronger and harder (i.e. more brittle). Apart from increasing hardness and strength properties, nanocrystalline material offers higher electrical resistance, increased specific heat capacity, improved thermal expansion properties, lower thermal conductivity and improved magnetic properties [58].

2.5.2 Nanocrystalline materials prepared by solid state processing (Mechanical Alloying)

There are several techniques for producing nanocrystalline material. These can be done for different phases such as vapour phase (e.g. inert gas condensation), liquid phase (e.g. electrodeposition, rapid solidification) and solid state (e.g. mechanical attrition).

One of the advantages of using mechanical alloying process to fabricate nanocrystalline material is its potential capability to produce bulk quantities of material in solid state using uncomplicated equipment and at room temperature [59].

Mechanical alloy (MA) is a powder processing technique for the production of homogenous material starting from blended elemental powder mixtures and create the composite metal powders with controlled fine microstructure. During MA there is repeated fracturing and rewelding the powder in highly energetic ball mill. This ball milling process involves a high energy surface reaction interdiffusion, joining and equally rapid breaking apart of the intercolliding particles (as in Figure 2.24). Hence, minimum grain size

obtained by milling has been attributed to a balance between the defect/dislocation structure introduction by the plastic deformation of milling and its recovery by thermal processes.

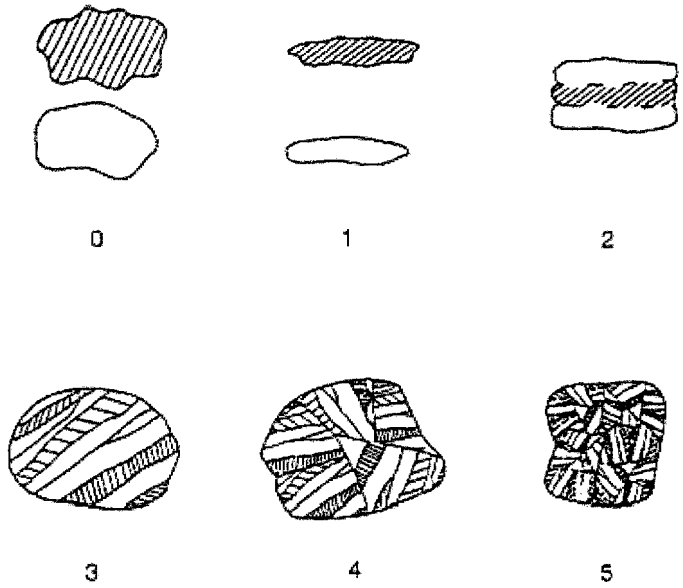

Figure 2.24 Schematic representation of typical stages (0 to 5) of particles are repeatedly flattened, fractured and welded, an homogeneous mixture on the atomic scale is obtained [60]

2.5.3 Factor affecting the mechanical alloying

The properties of milled powder included the particle size distribution, the degree of disorder or amorphization and the final stochiometry. These properties can be more completed controlled by monitoring the milling condition. The determinant influence the final milled powder are two main factors: (1) the raw material used for MA, and (2) process variables such as type of milled, milling container, milled speed, milling time, type, size and size distribution of the grinding medium, ball-to powder weight ratio, extent of filling the vial, milling atmosphere, process control agent and temperature of milling [13, 61]. A more detailed explanation can be found in Suryanarayana's work [13].

CHAPTER 3 INITIAL TRIALS

This chapter reports the different types of raw materials used by two different equipments. Three different ratios of compacted reactants employed prior to the SHS process. Characterisation methods for morphology and phase analysis are also briefly described.

3.1 As-received elemental powder

The elemental powder composition is made up of titanium, Ti (99.9% purity, CERAC Inc., USA) and nickel, Ni (99.9% purity, CERAC Inc., USA) as shown in Table 3.1. The average particle size of Ni and Ti were 5 μm and 74 μm, respectively. The idea of using a smaller particle size for Ni and larger particle size for Ti is to increase the surface-volume ratio of the reactant and induce higher diffusivity rate of Ni into Ti during the combustion synthesis process. In doing so, fine Ni powder is postulated to enhance the formation of NiTi intermetallic phase and eliminated the unreacted Ni in the final SHS product [5]. However, the size difference between Ni and Ti will cause problems of agglomeration and size segregation during mixing/blending of equiatomic of Ni-Ti powder. Thus, morphological studies were carried out to verify any problem on agglomeration and size segregation.

Table 3.1 The chemical composition of raw powders (ref. Appendix A and Appendix B).

Ti (at.%)	**Ca (at.%)**	**Sr (at.%)**
Bal.	<0.001%	0.0005%
Ni (at.%)	**Co (at.%)**	
Bal.	<0.0003%	

3.1.1 Morphological study

The as-received powders of Ti and Ni were examined under scanning electron microscop (SEM). From the SEM micrographs, the shape of Ni powder appeared to be filamentous an Ti powder particulate was angular as shown in Figure 3.1.

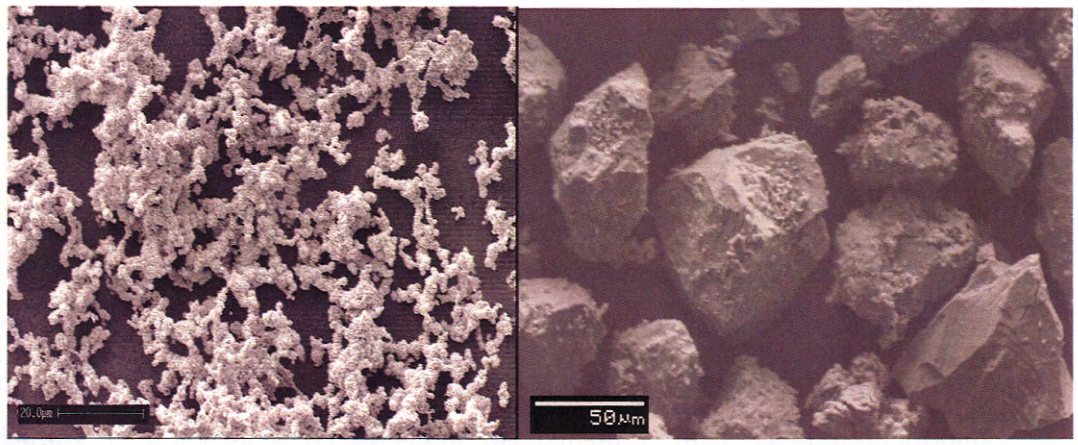

(a) (b)

Figure 3.1 As-received (a) Ni with particle size ~5 μm and filament shape (b) Ti partic size ~74 μm and angular shape.

3.2 Experimental Plan

The as-received Ni and Ti reactant powders were mixed into an equiatomic ratio for synthesis The weight of the powders was measured with an analytical balance (Mettler-Toledo™ B204 S ref. Appendix C). The mixing was conducted with two different equipments: tumbler mixe (Bioengineering Inversina™) and ball milling machine (Retsch™ machine Model PM-400) a shown in Figure 3.2. The classical mixing method by tumbler mixer is to ensure homogenou mixing of elemental powder. Nanocrystalline reaction agent was obtained by solid-stat process such as mechanical alloying (MA). The powder mixture was then cold compacted to desired green density and shape. The compact was synthesized through SHS process to obtai the porous parts. The morphology studies, phase analysis and mechanical property analysi were done on the final SHS products. Finally, thermal reaction treatment studies were carrie out on the as-SHS part for thermal analysis.

(a) (b)

Figure 3.2 Two different methods for preparing the as-received powder: (a) Bioengineering Inversina™ tumbler mixer; (b) Retsch™ machine Model PM-400 ball milling machine.

3.2.1 Compaction Stage

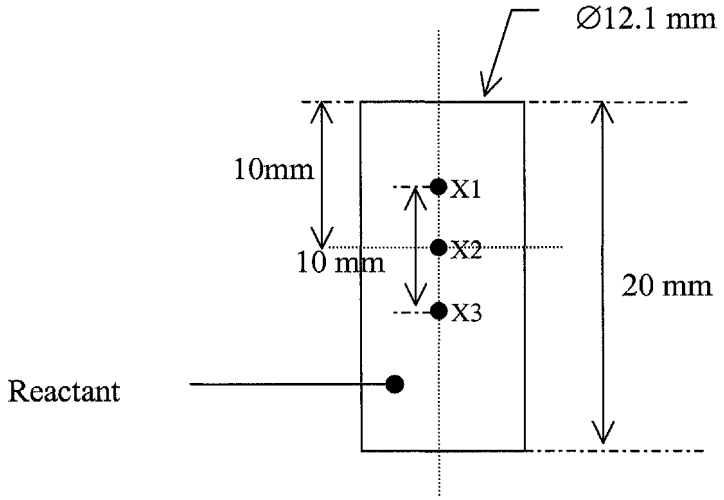

Figure 3.3 Illustration of points of interest on the reactant for morphological and phase analysis

The cold compaction was conducted on a 30 Ton WASBASH™ hydraulic press for 120s using a double action die to form pellets of Ø12.1 mm and height of ~ 20 mm. Each mixed

reactant powders was about 8g and fed into a ∅12.1 mm by 25 mm deep tool steel die. Th height h, diameter d and weight m of the pellets were then measured using a by micromete and analytical, respectively. The green density, ρ, was estimated using the followin equation (3.1). Figure 3.3 shows the points of interest (X1, X2 and X3) were selected on th reactant for morphological and phase analysis. Therefore statistical average point of X1, X and X3 were then evaluated.

$$\rho = \frac{m}{\pi\left(\frac{d}{2}\right)^2 h} \tag{3.1}$$

The general porosity percentage, ε, of the reactant was calculated as followed:

$$\varepsilon = \left(1 - \frac{\rho}{\rho_o}\right) x100\,\% \tag{3.2}$$

where ρ_o is the density of the corresponding bulk material. The densities of bulk Ni-T elemental powder and nanocrystalline reaction agent were measured by gas pycnomete Micromertitics™ AccuPyc 1330. Three pellets were prepared for each experiment conducte to obtain a statistical average.

3.2.2 The SHS experimental procedures

Table 3.2 tabulates three different composition ratios used in this investigation. Sample synthesised from $NiTi_{100\%}$ of which the constituents were elemental powder. They were use as control samples to study the effects of adding NiTi nanocrystalline reaction agent. Thre different compaction forces and two different preheating temperatures were investigated a shown in Table 3.3. Each of the specific compacted reactant was assigned to an I.D. numbe for identification purposes. An ignitor was then used to initiate an external energy source t heat up one end of the sample. The experiment was repeated three times.

Table 3.2 The chemical composition ratio of three sets of reactants

Set	Notation	Ni-Ti nanocrystalline reaction agent (wt%)	Ni-Ti Elemental (wt%)
1	$NiTi_{100\%}$	0	100
2	$NiTi_{MA25\%}$	25	75
3	$NiTi_{MA50\%}$	50	50

Table 3.3 Experimental parameters on SHS

Compaction force [kN]	8,16,24
Preheat temperature [°C]	200,300

3.2.3 Mechanical properties experimental procedure

Uniaxial compression tests were performed on the specimens using an INSTRON hydraulic testing machine. The strain rate was kept at 10^{3}/s. The compression tests were performed at constant room temperatures (25 °C). The compressive samples from the cylindrical porous $NiTi_{100\%}$ (Chapter 6) and $NiTi_{MA25\%}$ (Chapter 7) were cut to a size of 12.1 mm nominal diameter and 10 mm nominal depth with general porosity ranging from 50 to 55%. Five compressive specimens from each porous $NiTi_{100\%}$ and $NiTi_{MA25\%}$ were performed for the compression test. The nominal stress–strain curves were recorded. The ultimate compressive strength and compressive strain were defined as the values of stress and strain, respectively, at which stress reached the maximum value in the stress–strain curve.

3.2.4 The thermal reaction treatment experimental Procedure

The SHS-synthesized porous $NiTi_{100\%}$ and $NiTi_{MA25\%}$ were under heat treatment in the flowing argon gas environment using a top loading furnace (Oxy-Gon™ TC Series). The heat treatment were divided into two stages: (1) solid solution treatment at 800 and 1000 °C for 4 h of holding time; (2) aging treatment at 400, 450, 500 and 550 °C for 1 h holding time. In both stages the heating rate was 5 °C/min and cooling by of furnace cooling.

3.3 Characterisation Methods

3.3.1 Morphological study

The as-SHS final products were cut using a Struer™ diamond cut-off wheel and mechanically polished to ensure good quality surface for morphology of pore and phase analysis. The samples were examined by optical, scanning electron microscopy (SEM) and transmission electron microscopy (TEM) depending on the particle size of the samples.

The morphology of the products were observed by scanning electron microscopy (SEM)(i.e. JEOL JSM5600LV) operated at 20 kV equipped with an energy dispersive x-ray (EDX) backscatter electron spectroscopy (BES) unit. The general porosities of the final product were measured with image analysis software (i.e. Cambridge Instruments Leica™ Quantimet 570).

The pore sizes of the final SHS product were estimated using image processing and analysis software (i.e. ImageJ™)

In addition, JEOL 2000 transmission electron microscopy (TEM) operated at 200 kV was used to investigate more detailed analysis for finer grain size particles. Thus, TEM was employed to approximate the crystallite size of the nanocrystalline reaction agent powders.

3.3.2 Phase analysis

Phase studies of the as-SHS products were determined by X-ray diffraction (XRD) (i.e. Philips™ MPD 1880 X-ray diffractomer) with CuKα radiation at 40 kV and 30 mA.

XRD techniques can be applied to analyse very fine particles in the range of 50 nm [53]. The crystallite size and lattice strain of the nanocrystalline reaction agent by MA was established using the X-ray peak broadening techniques. The XRD peak broadening is due to instrumental effects, small particle size and lattice strain. The MA powder usually agglomerated at higher milling time, thus it was more accurate to relate to the diffraction. The crystallite sizes of the MA Ni-Ti powder were determined by measuring the Bragg peak

width at half the maximum intensity and applying the Scherrer formula which is shown in equation (3.3).

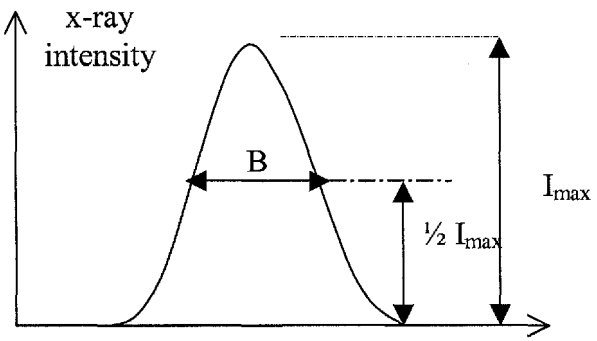

Figure 3.4 X-ray peak broadening is measured in term of the width B at an intensity one half of the maximum

$$B = \frac{0.9\lambda}{d_s \cos\theta} + \eta \tan\theta \qquad (3.3)$$

Where

d_s - the crystallite size λ - the wavelength of the X-radiation used (i.e. 1.5406 Å)

θ - the Bragg angle B- the peak width at half the maximum intensity

η- the lattice strain

After rearranging equation (3.3) can be written as follow:

$$B\cos\theta = \frac{0.9\lambda}{d_s} + \eta \sin\theta \qquad (3.4)$$

Therefore, when $B\cos\theta$ is plotted against $\sin\theta$, a straight line is obtained with the slope as η and the intercept as $0.9\lambda/d_s$. From this equation, the crystallite size, d and the lattice strain η at various milling times can be calculated.

3.3.3 Thermal analysis

The phase constituent was determined by X-ray diffraction. From the aged materials, specimens were cut out in one region for modulated differential scanning calorimeter (DSC) measurements. This technique measures the heat absorbed or given off by a small sample of the material as it is heated and cooled through the transformation temperature range. The

endotherm and exotherm peaks, as the sample absorbs or gives off energy due to th transformation, are easily measured for the beginning peak, and end of the phase change i each direction. The reverse transformation behavior during heating was investigated usin DSC Type 2920 by TA Instruments. DSC specimens, with mass between 15 to 16 mg, wer cooled down to –40 °C and held for 3 min to establish thermal equilibrium. Then, the DS measurement started heating up 150 °C at a rate of 5 °C/min.

3.4 The powder loading and other handling procedures

To minimise oxidation of the powder, all powder handling procedures such as loadin measurement and compaction were carried out inside a workstation (i.e. MBRAUN™ Labst Germany) as shown in Figure 3.5. The workstation provides a complete laboratory inert ga system, including glove box, external gas purification system, small standard antechambe and PLC control with touch-screen monitor. The workstation environment is constantl monitoring at 1 ppm of O_2 and 1 ppm of H_2O with O_2/H_2O analyzer. The handlin procedures included the preparation of elemental powder and nanocrystalline reaction age during mixing and mechanical alloying, respectively. During the compaction stage, th reactants were fed into the die inside the workstation to reduce contamination.

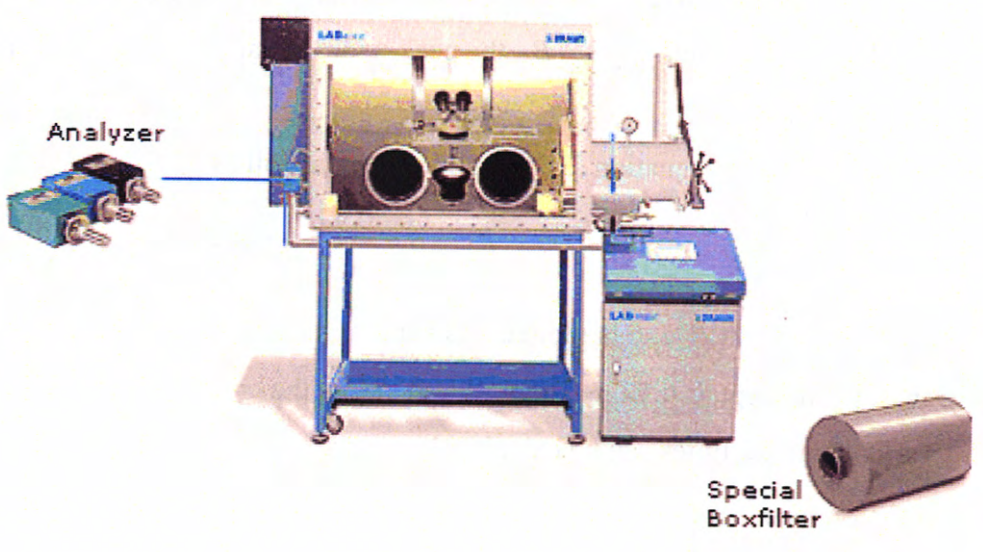

Figure 3.5 MBRAUN™ Labstar workstation

CHAPTER 4 PREPARATION OF REACTANT POWDER

This chapter describes the two different methods on how to prepare the reactant powder: (1) the elemental powder by tumbler mixer, and (2) the nanocrystalline reaction agent by mechanical alloying MA process. Results and discussions on the outcomes from the two methods are included in this chapter.

4.1 Calculation for equiatomic weight percentage composition of NiTi

It is necessary to obtain a precise concentration mixing of Ti and Ni through theoretical calculation. Hence, this calculation is done as follows:

$$\text{wt.\% of Ni} = \frac{\frac{X\ .M_{Ni}}{N_A - Avagadro's\ nos.}}{\frac{X\ .M_{Ni}}{N_A} + \frac{(1-X)M_{Ti}}{N_A}}$$

$$= \frac{X_{Ni}.M_{Ni}}{(1-X_{Ti}).M_{Ti} + X_{Ni}.M_{Ni}} \quad (4.1)$$

$$\text{wt.\% of Ti} = \frac{X_{Ti}.M_{Ti}}{X_{Ti}.M_{Ti} + (1-X_{Ni}).M_{Ni}} \quad (4.2)$$

Where

X: The percentage of composition mixture (i.e. 50%)

M: The atomic weight in [amu] (i.e. M_{Ti} - 47.9 & M_{Ni} - 58.71)[62]

From the equations (4.1) and (4.2), the equivalent weight percentage for Ni and Ti are 55.07% and 44.93% respectively.

4.2 Preparation of elemental powder by tumber mixer

The equiatomic weight percentage composition Ni-Ti reactant powders were measured by analytical balance to four decimal places accuracy and mixed by a tumbler mixer. The tumbler mixer uses inversion kinematics mechanism for mixing the reactant. This three dimensional motion of the tumbler mixer combines a figure-of-eight movement with rotation and sets the powder in a rhythmic, pulsating motion. This technique is much more reliable than other techniques such as barrel mixers, v-blenders, double cone blenders or ribbon mixers, which have segregation zones and longer mixing and cleaning times.

In the tumbler mixer, the mixing efficiency varies with both the powder characteristics and the mixer operation characteristics. For example, a low rotational mixing speed is inefficient because of little motion. At high rotational speeds, the centrifugal forces can prevent mixing. Therefore, the optimal rotational speed for cylindrical mixer are estimated by using the Sundrica formula [53]:

$$N_o = \frac{32}{d^{0.5}} \tag{4.3}$$

Where

N_o is the optimal rate of ratio [RPM].

d is diameter of the cylinder mixer [m].

With ∅0.09m of the cylinder mixer used, the calculated optimum speed is obtained at 106 rpm. The equiatomic mixed Ni-Ti powder is filled to 30% volume of the cylindrical mixer capacity ensure mixing efficiency (ref. section 2.8.5). Table 4.1 tabulates the experimental parameters such as the method of mixing, the mixer speed, the mixing time and the mixing temperature used for preparation of Ni-Ti elemental powder.

Table 4.1 The parameters used in for preparation of Ni-Ti elemental powder

Mixing	**Method**	*Tumbler mixer*
	Speed [RPM]	*106*
	Time [h]	*8*
	Temperature [°C]	*25*

4.2.1 The morphology studies, chemical analysis and phase analysis

SEM was used to examine the blended Ni-Ti elemental powder morphology. The chemical analysis made by EDX spectroscopy, gave a quantitative analysis of composition percentage Ti and Ni as 45.35 and 53.57 (at %) respectively as shown in Figure 4.1. The Au peak was attributed to gold coating on the specimen for SEM examination. The XRD phase analysis in Figure 4.2 shows individual peak of Ni and Ti powders. Hence no alloying has occurred. The elemental Ni-Ti density was measured to be 6.0186 g/cm^3 using pycnometer Micromertitics^{TM} AccuPyc 1330.

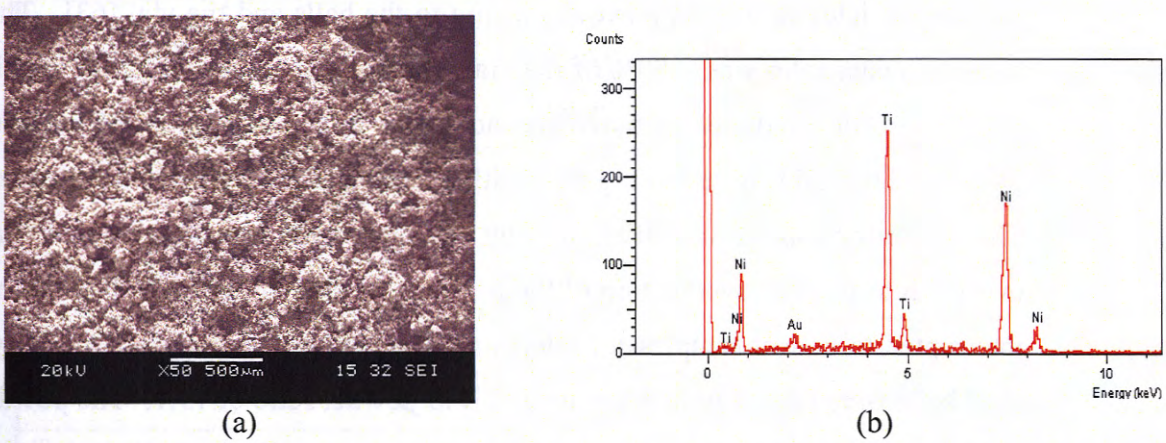

(a) (b)

Figure 4.1 (a) SEM micrograph and (b) the EDX analysis of on Ni-Ti mixture prepared by tumbler mixer.

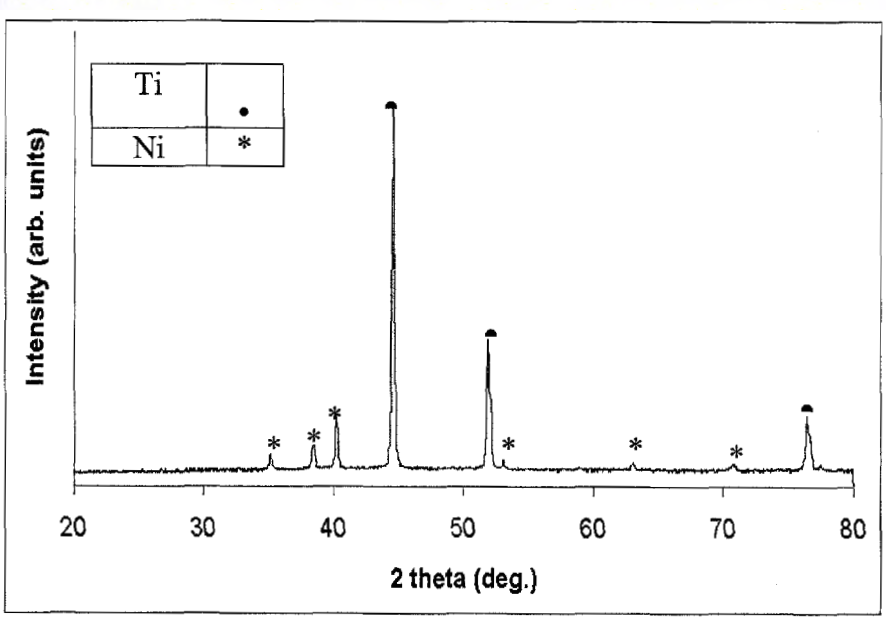

Figure 4.2 XRD spectrum on Ni-Ti powder by tumbler mixer

4.3 Preparation for Nanocrystalline Reaction Agent by MA

The equiatomic Ni-Ti elemental powders are mechanically alloyed in a high-energy ball milling machine at ambient temperature. A flat-ended stainless steel vial is used in order to obtain higher rates during the alloying process [13]. The ball-to-powder ratio was 15:1 and two different sizes of stainless steel balls were used (i.e. ∅10 mm and ∅20 mm) to minimize the amount of cold welding and powder coated onto the surface of the balls [59]. Process control agent ethanol was added to the initial powder load to minimize cold welding of powder particles as well as powder sticking to the balls and the vial [63]. The total milling ball-to-powder ratio was ≤ 50% of the vial. This space allowance in the vial is for the balls and the powder particles to move around freely in the vial to ensure an optimum milling process. The vial was sealed together with adhesive tape to prevent from any contamination. The ball milling speed was 200 rpm. The milling process was programmed to rest 30 min for every 1 h to prevent overheating of the powder. At regular intervals, the milling process was interrupted to collect samples for microstructural and phase analysis. Similarly, the stainless steel balls were taken out to maintain a ball-to-powder ratio of 15:1. The powder loading and other handling procedures were done in an environmentally controlled glove box. Table 4.1 tabulates the summary of mechanical alloying parameters.

Table 4.2 Mechanical alloying parameters for Ni-Ti nanocrystalline reaction agent

Material	*Ti*	*Ni*
Particle size [μm]	*74*	*5*
Weight (g)	*39.089*	*47.9109*
Mechanical Alloying		
Type of mill	*High-energy ball-milling machine*	
Milling container	*Flat-ended stainless steel vial*	
Milling Time [hrs]	*5,30,45,60,75,105,120*	
Milling Speed [RPM]	*200*	
Grinding medium	*Two type stainless steel balls at ∅10 mm and ∅20 mm*	
Ball-to-powder weight ratio	*15:1*	
Vial Material	*Stainless steel*	
Milling atmosphere	*Argon*	
Process control agent	*Ethanol*	
Amount of Process control agent	*1 wt% on the total Ni-Ti powder used*	
Temperature of milling	*25 °C*	

4.3.1 Morphological studies

The objective of MA process is to achieve nanocrystalline Ni-Ti power as a reaction agent. During the MA process, Ti and Ni particles were subjected to severe mechanical deformation from collisions with the steel milling balls. The Ni and Ti particles were repeatedly flattened, cold welded, fractured and rewelded.

Figure 4.3 shows the morphology of the equiatomic Ni-Ti powder at 0 h to 120 h of milling time as examined by SEM. Before ball milling, the Ni and Ti particles can still be identified morphologically as shown in Figure 4.3a. After 5 h of milling time, both the particle sizes were reduced as shown in Figure 4.3b. The size of the particles was further reduced till 60 h of milling time, flattening and fracturing between the powders and milling ball (as shown Figure 4.3(c-e)). The powder gained its average particle size at 75 h of milling time due to welding and rewelding that had taken place. The increasing size of powder is also due to the agglomeration of particles into larger aggregates as illustrated in Figure 4.3(f). With further processing shown in Figure 4.3(g-h) after 105 h of milling time, the internal structure of the

powder continued to become more refined. The powder particles with further milling duration became more homogenous while still keeping the granular morphology.

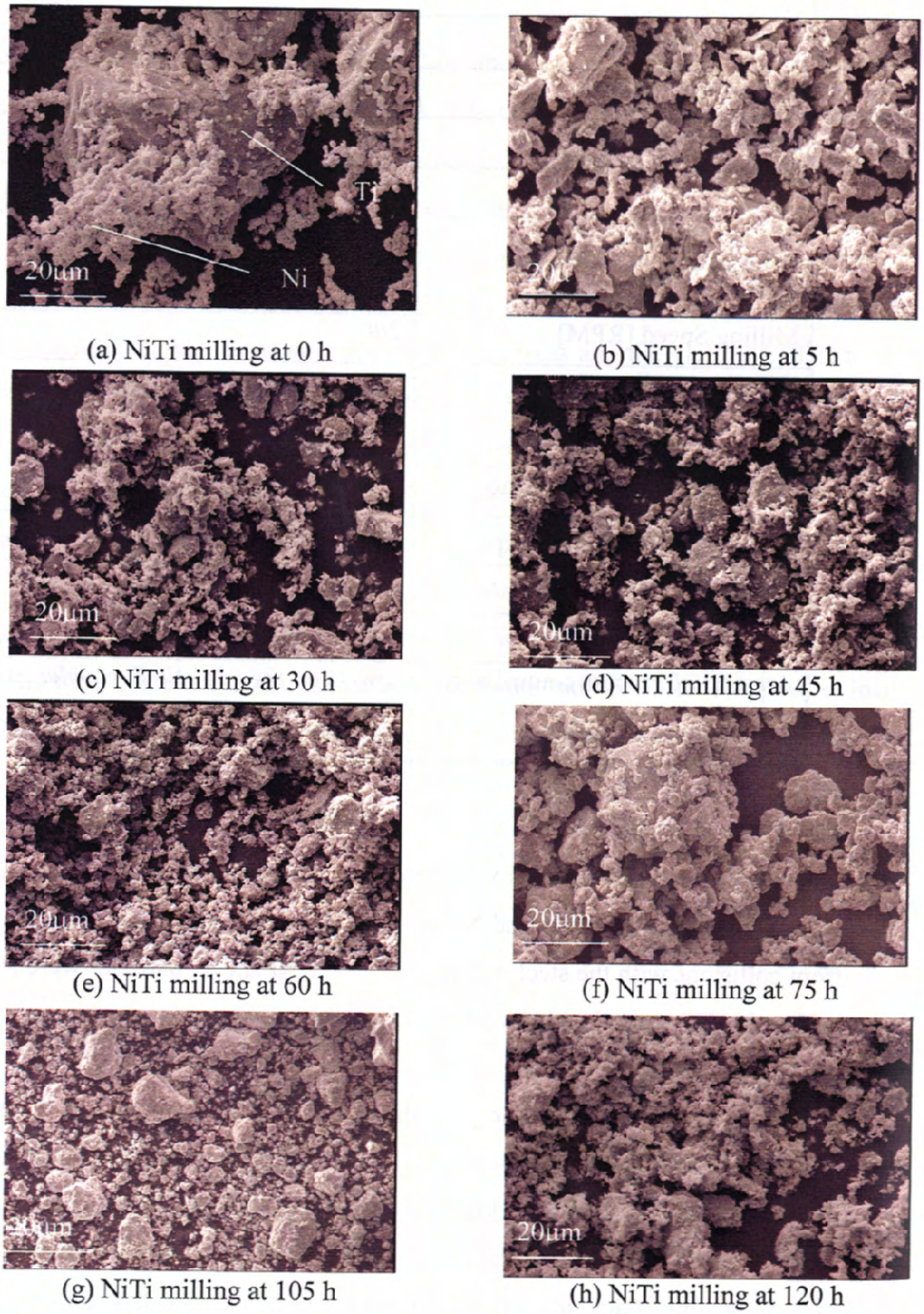

(a) NiTi milling at 0 h (b) NiTi milling at 5 h

(c) NiTi milling at 30 h (d) NiTi milling at 45 h

(e) NiTi milling at 60 h (f) NiTi milling at 75 h

(g) NiTi milling at 105 h (h) NiTi milling at 120 h

Figure 4.3 SEM morphology of mechanically alloyed NiTi powder at (a) 0 h (b) 5 h (c) 20 h (d) 45 h (e) 60 h (f) 75 h (g) 105 h (h) 120 h milling times.

4.3.2 The crystallite size and lattice strain of the MA powder

The crystallite size and lattice strain of the MA powder were established using the X-ray peak broadening techniques. Figure 4.4 shows results indicating that reduction in the crystallites size in MA powder had taken place by increasing ball-milling time. The lattice strain of the MA powder increased with increasing milling time. The values of the strain continuously increased until it reached 105 h milling time. The strain dropped and the crystallite size decreased below 10 nm. A balance between coalescence and fragmentation was reached during ball milling which led to relatively stable average crystalline particle size of 10 nm with large lattice strain of 0.85%. It can be concluded that a large number of dislocations were present in the crystals when the internal elastic strain reaches its maximum value.

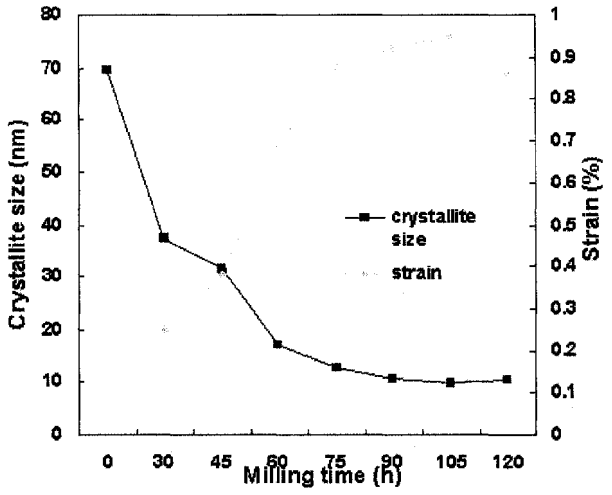

Figure 4.4 Effect of the crystallites size and strain with increasing ball-milling time.

TEM investigations were preformed in order to check the crystalline size and crystalline nature structure of the Ni-Ti ball-milled powder. Figure 4.5(a-c) show (i) bright field image (BFI), and (ii) corresponding selected-area diffraction pattern (SADP) on ball-milling Ni-Ti powder. In the observation, the particle size of the powder was found decreased to submicron level with increasing milling time. Figure 4.5 (ai) shows in TEM, the agglomerate Ni-Ti MA powder at 30 h milling time with particle sizes between 100 nm to 1 μm. The corresponding SADP in Figure 4.5 (aii) indicates a ring-spot pattern. This reveals the characteristic of polycrystalline powder is still present. Further processing to 75 h of milling time, the MA powder particles continue to reduce at around 20 to 200 nm as shown in Figure 4.5 (bi). Figure 4.5 (bii) shows the corresponding SADP of Ni-Ti alloy milled for 75 h. It revealed the

diffraction pattern containing lattice diffraction rings as well as the nearly continuous rings which suggests that the formation of nanocrystalline Ni-Ti alloy has been obtained. At the 120 h of milling duration, the corresponding SADP had shown (see Figure 4.5 (cii)) that the ring-spot pattern had disappeared totally but left existing lattice diffraction rings. This result indicate that a coexistence of crystalline and amorphous phases, which suggests the formation of nanocrystalline Ni-Ti alloy with trace amount of amorphous alloy. In addition, the corresponding BFI in Figure 4.5 (ci) showed no further reduction of crystalline size in the milled powder.

In the case of mechanical alloying, the mixing of elements takes place by diffusion. The high density of dislocations formed during mechanical alloying and increased grain boundary area. This occurrence is due to the decrease in crystallite size thus enhancing the diffusion process. Further milling at 120 h, showed no significant decrease in the Ni-Ti alloy particle size (see Figure 4.5 (ci)). This result is coherent with results obtained from the X-ray peak broadening technique.

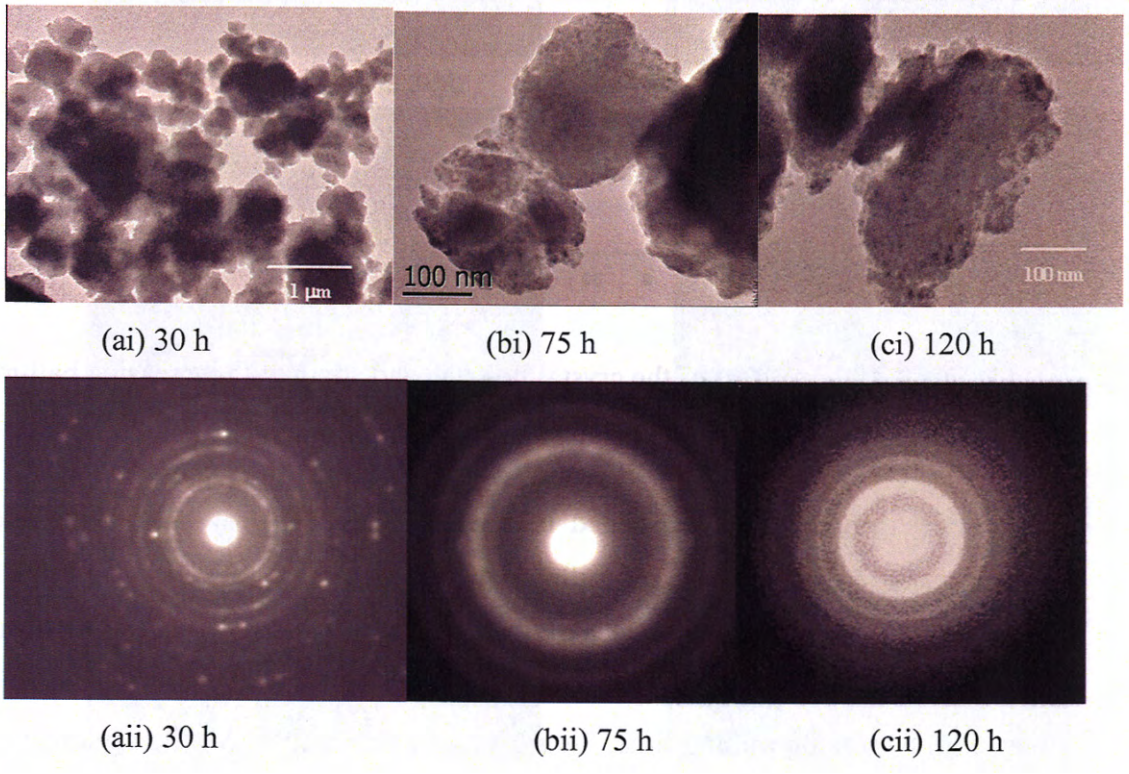

Figure 4.5 TEM results in the (a-c)i BFI and (a-c)ii and the corresponding SADP of Ni-Ti powder particle by MA at 30 h, 75 h and 120 h milling times.

4.3.3 Phase analysis

Figure 4.6 shows the XRD spectra of the Ni-Ti powder mixture after mechanical alloying for various milling times. The results revealed the increased milling period had broadened the sharp Bragg peaks remarkably. A new broad diffuse scattering halo at about $2\theta = 40\sim44^{\circ}$ after 60 h of milling time was observed implying the alloy had become partially amorphized. This occurrence is commonly attributed to the structural changes in the samples, such as the formation of amorphous phases, large lattice strains in grains, or the embedding of very small crystals in an amorphous matrix [63].

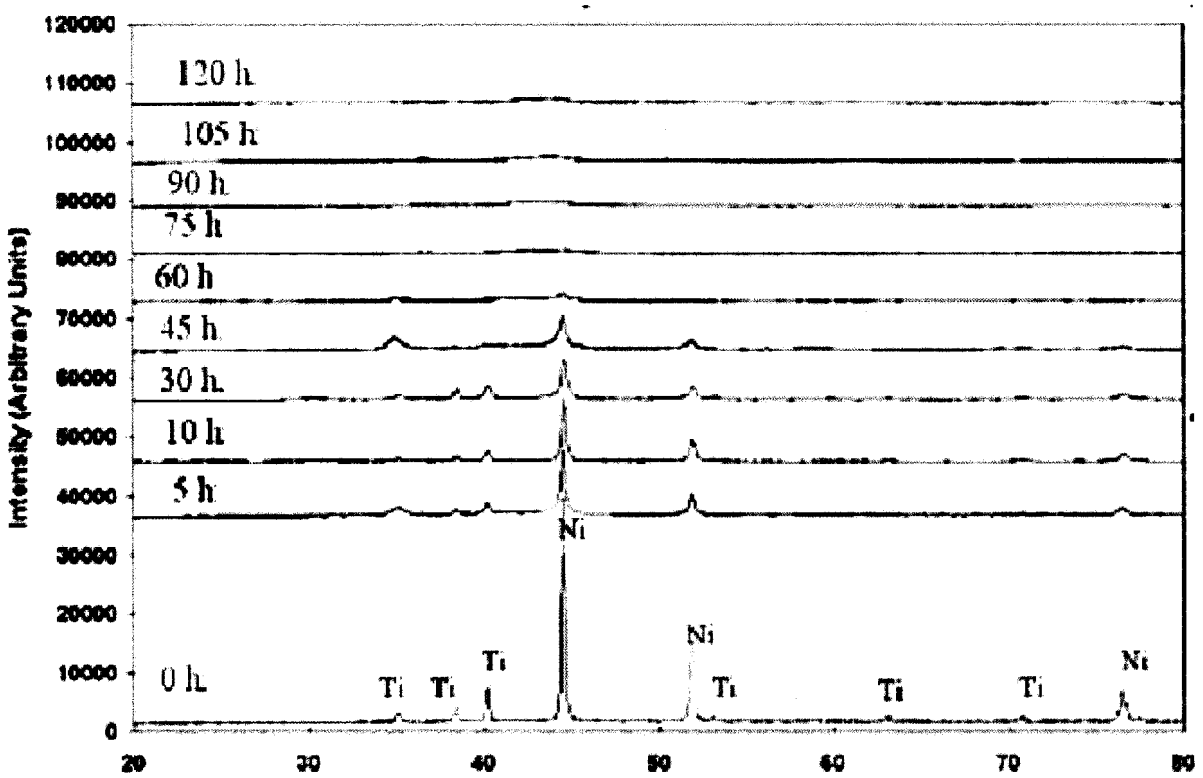

Figure 4.6 XRD spectra of MA Ni-Ti alloy for various milling durations

4.3.4 Impurities

The impurity content in MA Ni-Ti powder at different stages of milling was obtained by the EDS analysis as shown in Figure 4.7. It is evident that Fe and Cr are the main substitutional impurities at the highest hour of milling (120 h). The rate of interstitial impurity increased at the initial stage and maintained at a low impurity of Fe content at 1.45 at.% and Cr at 0.51 at.% with 75 h of milling time. However, beyond the milling time of 75 h, the amount of Fe and Cr impurity increased significantly up to Fe ~ 20 at.% and Cr to ~ 4 at.% respectively at 120 h of milling time. The main source of Fe and Cr impurity may be due to wear debris between the steel milling media such as the vial and balls throughout the milling process.

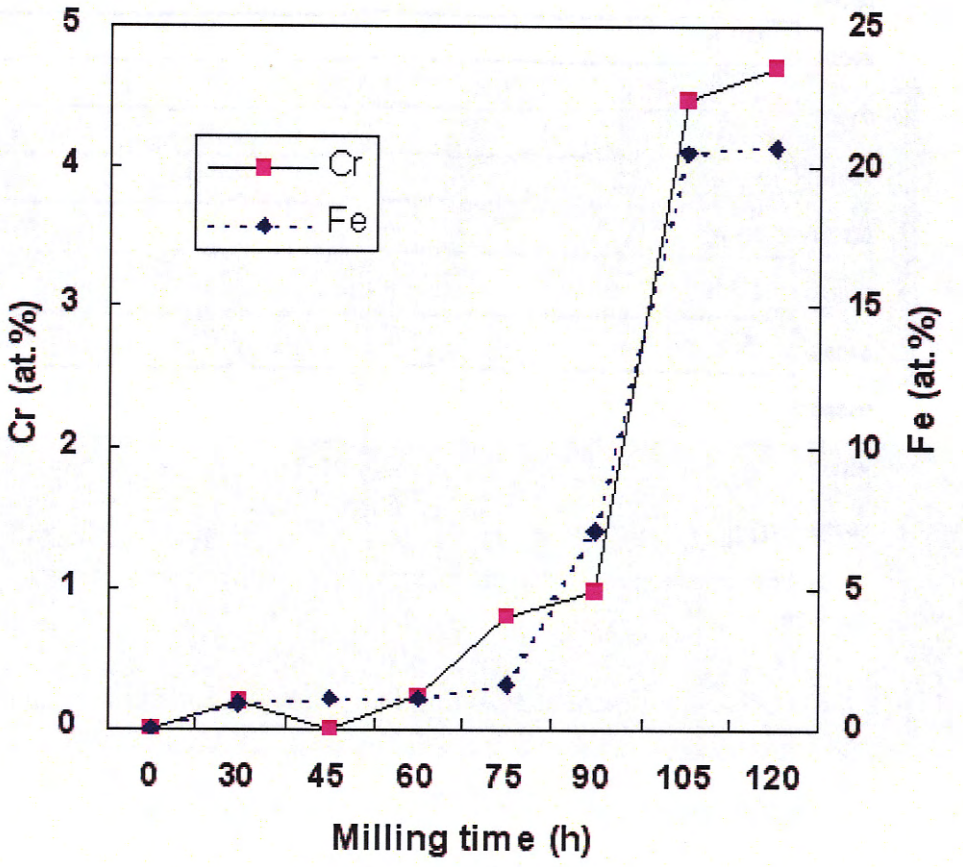

Figure 4.7 Iron (Fe) and Chromium (Cr) content with increase milling time

4.4 Conclusion

The elemental Ni-Ti powder prepared by the tumbler mixer was able to achieve homogenous mixture of reactant powders.

From the preparation studies for Ni-Ti powder by MA, nanocrystalline Ni-Ti alloy can be obtained by the MA process. The optimum duration of MA to achieve nanocrystalline Ni-Ti alloy as a reaction agent is at 75 h milling time. The least impurity contamination was also observed here. Phase analysis revealed no indication of any intermetallic phases formed. However, if the formation of intermetallics was found, this will result in decreasing reactivity during the SHS process. The purpose of achieving nanocrystalline as reaction agent powder by mechanical alloying (MA) is to increase the reactivity of the green elemental powder. This in turn may introduce a new energy into the material that will lower the activation energy barrier during SHS process.

CHAPTER 5 THE OPTIMISATION OF SELF-PROPAGATION HIGH-TEMPERATURE (SHS) SYSTEM

This chapter includes the optimisation of parameters for the ignition technique in order to produce net-shape porous parts. The compaction characteristics of the compacted reactant analysis were made during the compaction stage and were also included in this chapter.

5.1 Ignition in SHS

Figure 5.1 shows the ignition thermal arc system used in this work. This ignitor is electrically controlled and has an electrode that generates a spark to ignite the SHS. Two essential variables in controlling the spark are the power supply, P_s, which ranges from 5 to 150 W, and distance, d_e, of the electrode from the part surface at 0.5 and 1 mm. The parameters were optimised to achieve suitable modes of propagation.

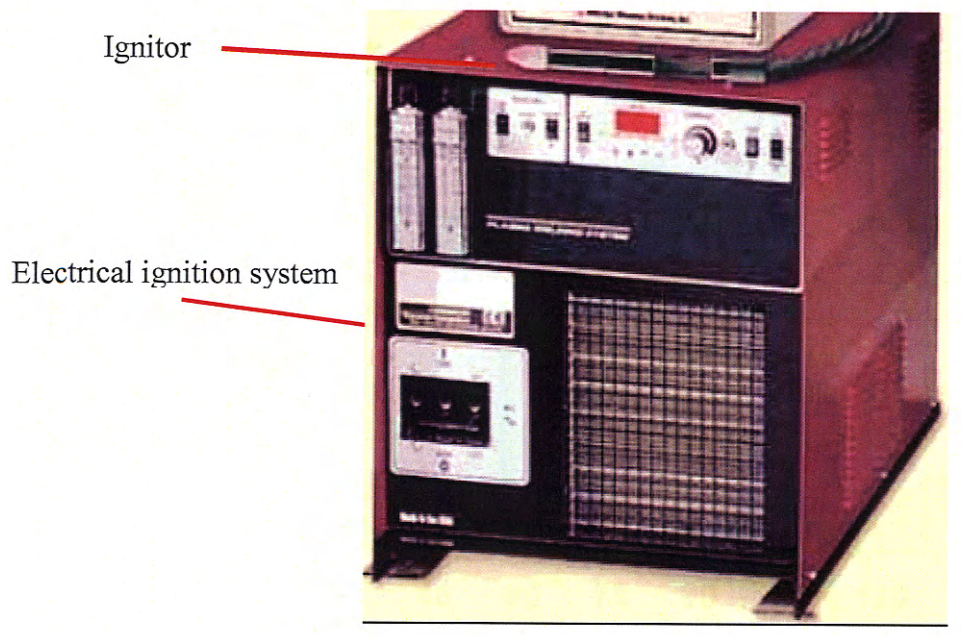

Figure 5.1 Ignition system: Thermal Arc™ Ultima 150

5.1.1 Induction furnace

Figure 5.2 shows the induction furnace (Norax Canada Inc™) used in the SHS system. An induction furnace was used to preheat the compact reactant within a short period and to maintain the compact at a constant temperature. Preheat temperature was regulated by proportional integral derivative (PID) controller to achieve a desired heat supply consistent throughout the experiment. Argon gas was supplied continuously to the sample as an atmospheric envelope to protect it from oxidation. Figure 5.3 presents the schematic layout of the SHS system.

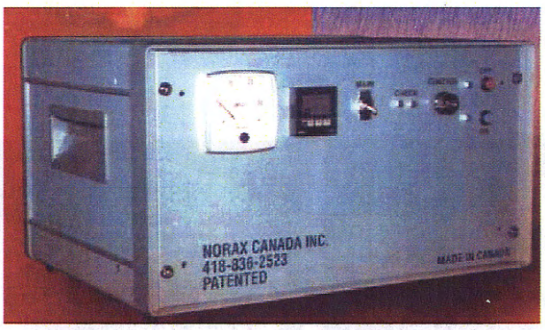

Figure 5.2 Norax Canada Inc™ induction heater

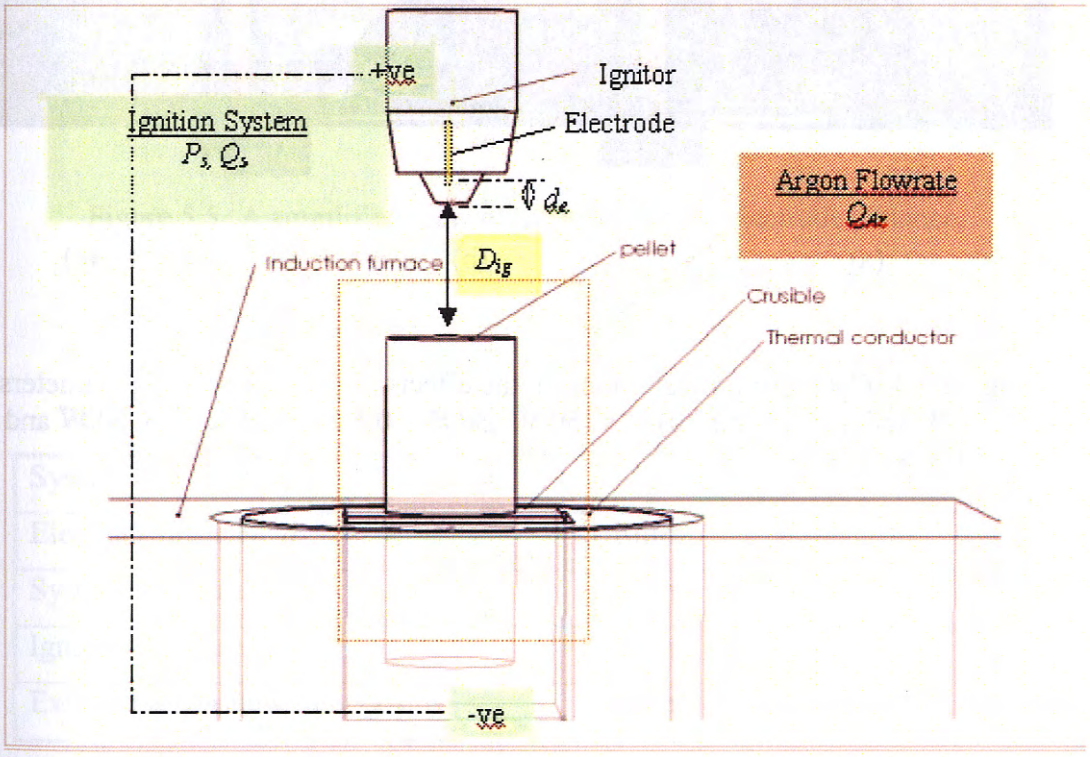

Figure 5.3 Schematic drawing of the SHS system.

5.2 Parametric optimisation of the SHS system

The photograph illustrated in Figure 5.4 displays the effects of the ignition system power P_s and electrode distance d_e on SHS porous NiTi. Ignition system power P_s was set at 100 W and 150 W at both the same electrode distance d_e of 0.5 mm as shown in Figure 5.4 a and b respectively. In both set-ups, the results had shown that the heat supplies were excessive enough to explode and deform the shape of the compacted reactant. Furthermore, no propagation reaction had occurred during the synthesis of NiTi. The propagation reaction occurred at P_s = 50 W with d_e at 1 mm and obtained a net-shape porous NiTi as shown in Figure 5.4c.

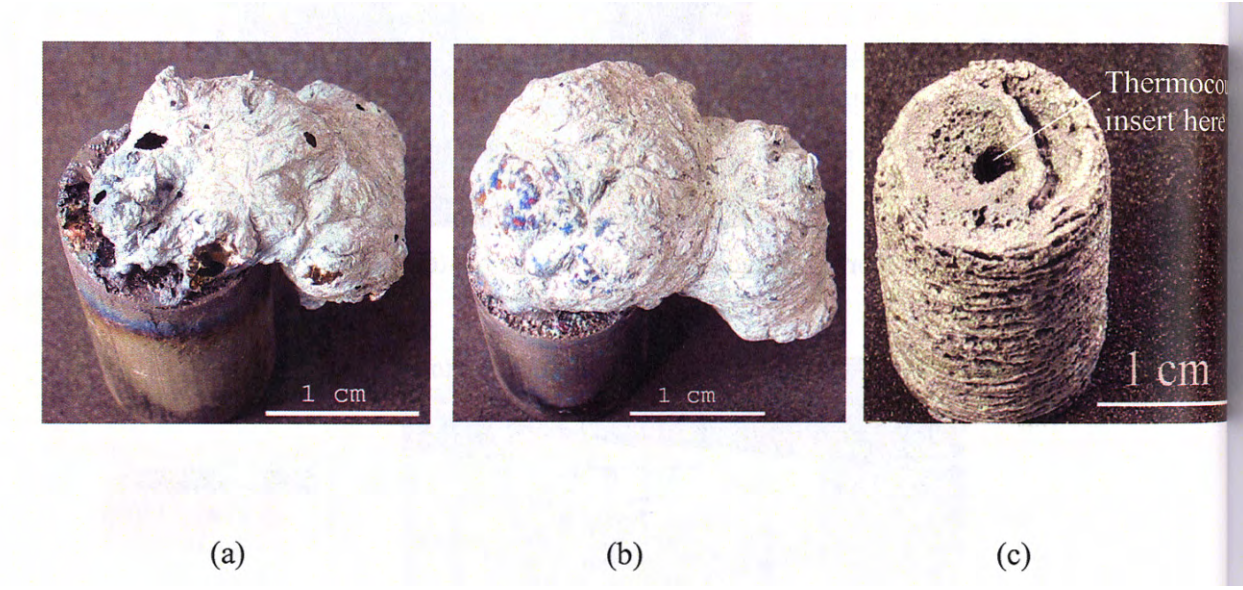

Figure 5.4 Photograph illustrations on the effects of ignition system parameters at (a) P_s =100 W and d_e = 0.5 mm (b) P_s =150 W and d_e = 0.5 mm and (c) P_s = 50 W and d_e = 1 mm on SHS Ni-Ti.

The heat intensity flux was regulated by the ignition system by varying the system power, P_s, and gas system flow rate, Q_s. The radius coverage of the ignition flame can be changed by adjusting the electrode distance, d_e, as shown in Figure 5.5. At d_e = 1 mm, the flame generated covered a greater surface area on the compacted reactant. In combination with a lower heat supply P_s at 50W, this prevented the heat intensity to be localized at the top of the compacted reactant thereby causing unwasted deformation on the final product shape. The optimum parameters for the ignition system are tabulated in Table 5.1.

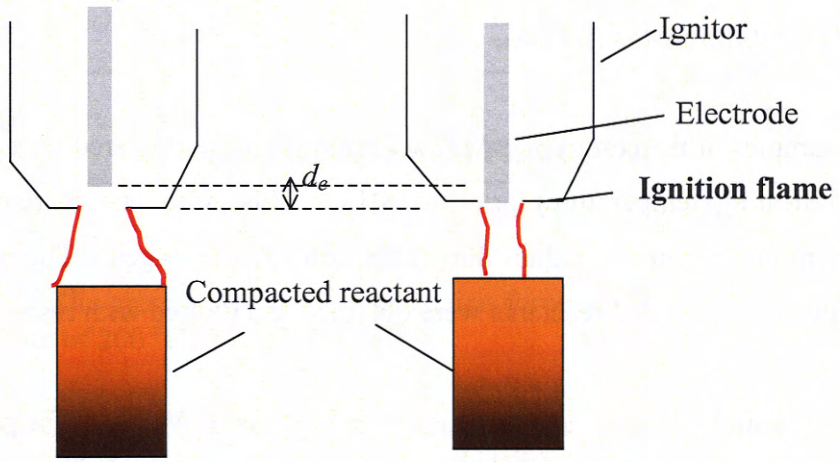

Figure 5.5 A simplified view of the effect of the electrode distance, d_e, on compacted reactant.

Table 5.1 The ignition setting for SHS process

System Power, P_s	~50 W
Electrode distance, d_e	1 mm
System flow rate, Q_s	6 *l*/min
Ignition distance, D_{ig}	~5 mm
External argon flow rate, Q_{Ar}	2 *l*/min

5.3 Compaction of reactant

The density of Ni-Ti powder after 75 h using mechanical alloying and elemental Ni-Ti were measured using a pycnometer Micromertitics™ AccuPyc 1330. The resultant mechanical alloying and elemental Ni-Ti's densities were 6.228 g/cm^3 and 6.0186 g/cm^3 respectively. The compaction behaviour of the elemental reactant ($NiTi_{100\%}$), 25% additive nanocrystalline reaction agent ($NiTi_{MA25\%}$) and 50% additive nanocrystalline reaction agent ($NiTi_{MA50\%}$) were studies in terms of green porosity, ε_g, height and diameter ratio, H/D.

5.3.1 Green porosity, ε_g

The elemental powder $NiTi_{100\%}$

Three samples of the compacted $NiTi_{100\%}$ reactants were prepared for each process parameters (i.e. preheating temperature) prior to SHS. This is to ensure reproducibility of having consistent green porosity values during the compaction stages. The mean of the three green porosities of compacted reactants were obtained and plotted with respect to compaction force.

Figures 5.6 and 5.7 show the compaction behaviour of $NiTi_{100\%}$, for preheating temperatures of 200 °C and 300 °C, respectively. The ε_g of $NiTi_{100\%}$ reactants were decreased with increasing compaction forces in both compaction behavioural studies. This is because the increased pressure enhances the packing density and leads to decrease porosity. With higher compaction force of 24 kN, the compacted $NiTi_{100\%}$, reactants for both preheating temperatures of 200 °C and 300 °C obtained an average ε_g of 45 vol.%± 2.5 vol.%. At lower compaction force of 8 kN, the average ε_g for the compacted reactant is 51 ± 1.3 vol.% at preheating temperatures of 200 °C and 300 °C. Table 5.2 tabulated the standard deviation of green porosity results at preheat 200 and 300 °C for three runs experiment.

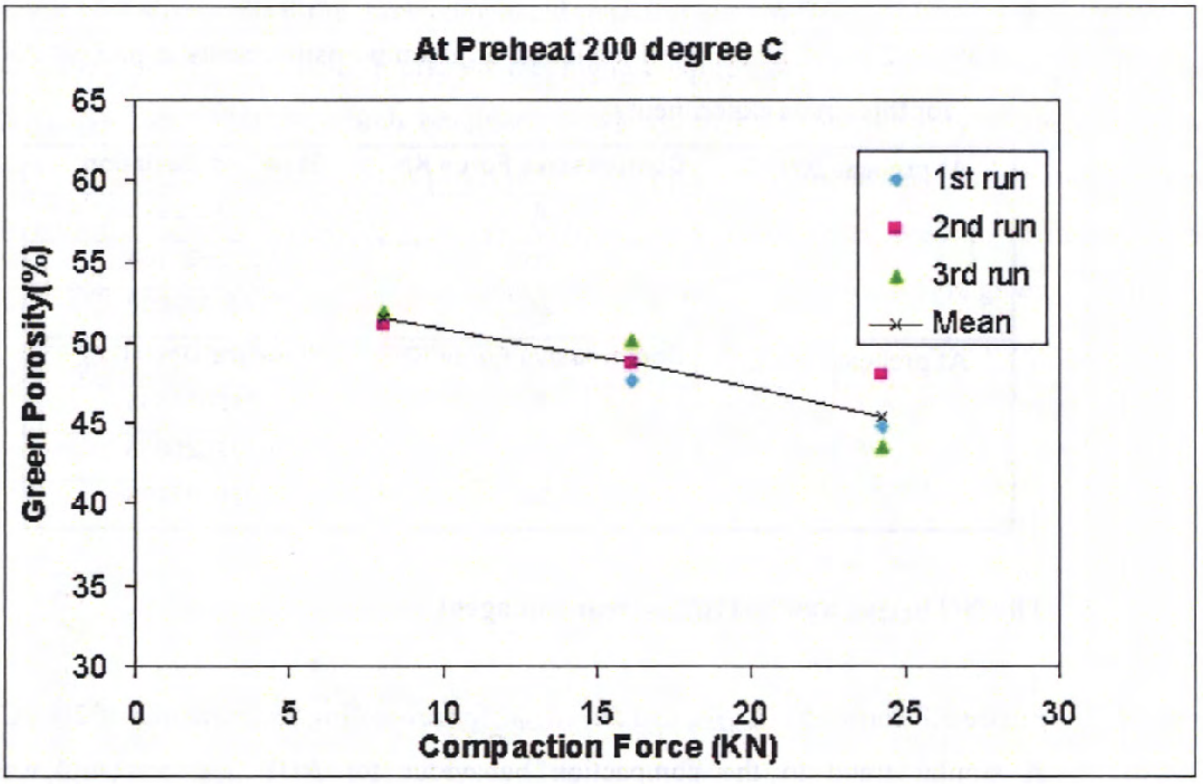

Figure 5.6 The green porosity Vs compaction force studies in $NiTi_{100\%}$, for preheating temperature of 200 °C.

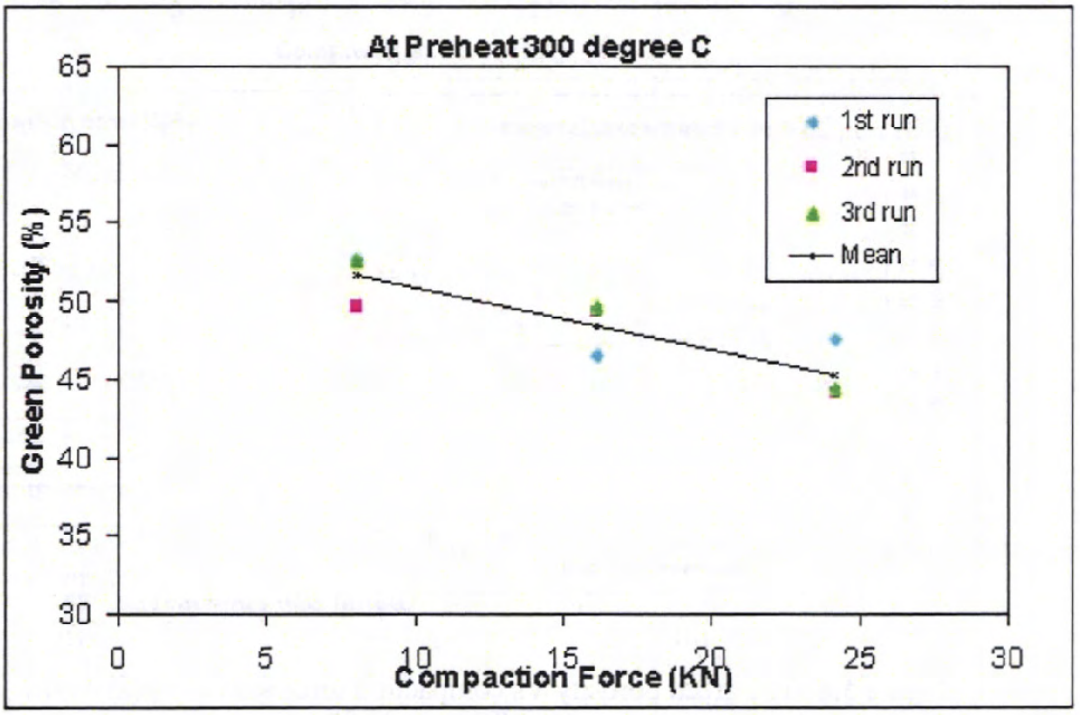

Figure 5.7 The green porosity Vs compaction force studies in $NiTi_{100\%}$ for preheating temperature of 300 °C.

Table 5.2 The standard deviation of green porosity results at preheat 200 and 300 °C for three runs experiment

At preheat 200 °C	Compressive Force KN	Standard Deviation
	8	0.408352973
	16	1.276590164
	24	2.267632888
At preheat 300 °C	**Compressive Force KN**	**Standard Deviation**
	8	1.719017385
	16	1.732625863
	24	1.956287403

The $NiTi_{MA25\%}$ and $NiTi_{MA50\%}$ reaction agent

Figure 5.8 shows $NiTi_{MA25\%}$ and $NiTi_{MA50\%}$ for preheating temperatures of 200 °C and 300 °C. A similar trend to the compaction behaviour for $NiTi_{100\%}$ reactants was noted. At compression forces from 8 to 24 kN, the compacted $NiTi_{MA25\%}$ yielded ε_g of ~ 47 ± 1.5 vol. % to 46 ± 1.0 vol.%, respectively and compacted $NiTi_{MA50\%}$ yielded ε_g of ~ 47 ± 0.5 vol. % to 44 % ± 0.5 vol.%, respectively.

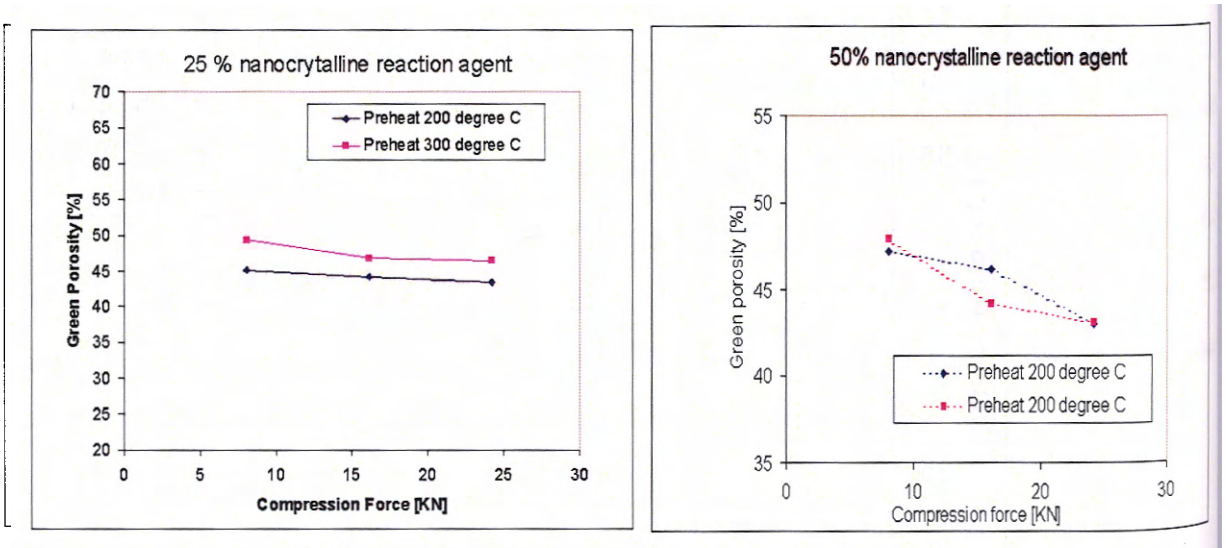

(a) (b)

Figure 5.8 The green porosity Vs compaction force studies in (a) $NiTi_{MA25\%}$ (b) $NiTi_{MA50\%}$ for preheating temperature of 200 °C and 300 °C.

Figure 5.9 shows all of the three compacted reactants (i.e. $NiTi_{100\%}$ $NiTi_{MA25\%}$, and $NiTi_{MA50\%}$) and their compaction behaviours. At the highest compression force of 24 kN, compacted $NiTi_{MA25\%}$ and $NiTi_{MA50\%}$ both obtained ~ 45 vol.% of green porosity while compacted $NiTi_{100\%}$ obtained ~ 48 vol.% of green porosity. However, at the lowest compression force of 8 kN, the compacted $NiTi_{MA25\%}$ and $NiTi_{MA50\%}$ obtained lower pressing efficiencies of ~ 51 vol.% green porosity than compared to compacted $NiTi_{100\%}$, of ~ 47% green porosity.

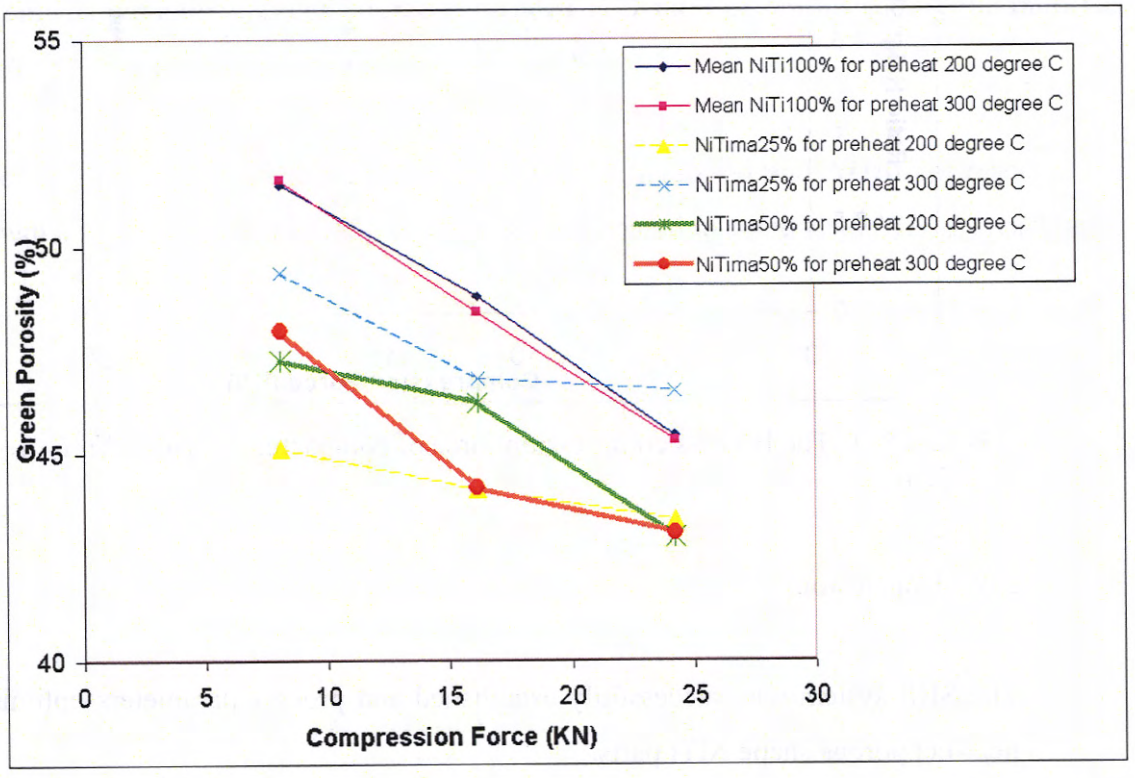

Figure 5.9 The green porosity Vs compaction force studies in $NiTi_{100\%}$ $NiTi_{MA25\%}$, and $NiTi_{MA50\%}$, for preheating temperature of 200 °C and 300 °C.

5.3.2 The height-to-diameter ratio, (H/D)

The height-to-diameter ratio, (H/D) of the compacted $NiTi_{100\%}$, $NiTi_{MA25\%}$ and $NiTi_{MA50\%}$ were recorded in Figure 5.10. A minimal variation of H/D range ~ 1.3 to 1.6 in all compacted reactants were obtained at the highest compaction force of 24 kN. However, at the lowest compaction force of 8 kN, a slightly more avid variation of H/D range ~ 1.3 to 1.9 in all of the three compacted reactants was noted.

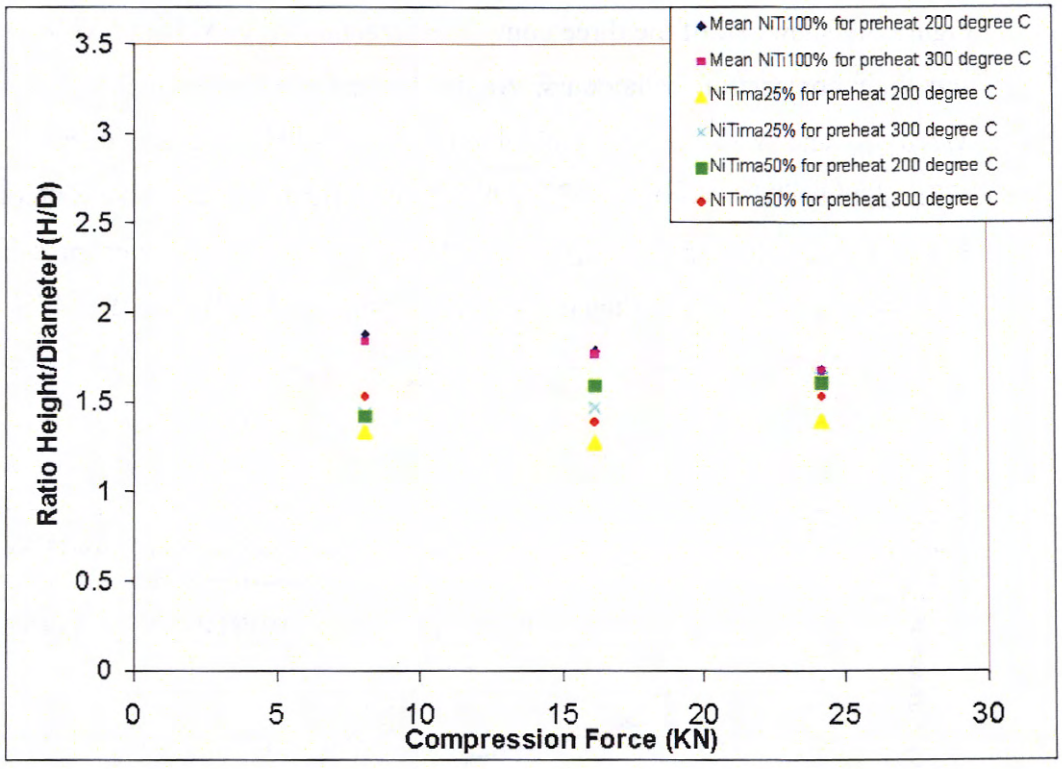

Figure 5.10 The H/D Vs compression force of compacted $NiTi_{100\%}$, $NiTi_{MA25\%}$ and $NiTi_{MA50\%}$.

5.4 Conclusion

The SHS system was successfully established and process parameters optimised to produce near-net porous shape NiTi parts.

The compression characteristics of compacted reactants were studied to determine the pressing efficiency during compaction stages. Minimal variation was also desired in the green porosity variation during compaction to ensure uniformity in properties and dimension of the final product after SHS process. The variation in the green porosity compacted reactant will influence the propagation of the SHS reaction and eventually affect the final as-SHS product properties (ref. chapter 2).

From the compression behavioural studies in compacted elemental Ni-Ti reactants ($NiTi_{100\%}$), it was shown that there were only slight variations amongst green porous samples. In comparison of all the three different compacted reactants, the reactants by MA process (i.e. $NiTi_{MA25\%}$ and $NiTi_{MA50\%}$) resulted in better packing densities during compaction stage. This is because the smaller particles (i.e. 25 or 50% nanocrystalline powder) could be used as

"fillers" between the interstitial spaces of larger particles (elemental powder) thus increasing the packing density. This in turn leads to the significant reduction of porosity and pore sizes.

The height-to-diameter ratio, (H/D) is an important evaluation parameter which reveals how uniform the compacted reactant density gradient is. The density gradient in the compacted reactant had resulted from a pressure gradient. Nevertheless, all the compacted reactant specimens were done under the recommended H/D ratio of not exceeding the ratio value 5 [53].

The smaller mean particle sizes from compacted $NiTi_{MA25\%}$ and $NiTi_{MA50\%}$ reactant had not shown any salient deviation of green porosity compared to compacted $NiTi_{100\%}$ reactants.

CHAPTER 6 SHS USING ELEMENTAL POWDER REACTANTS ($NITI_{100\%}$)

This chapter describes the study of green porosities obtained by the compacted reactants and H/D ratio during the compaction stage in terms of pore morphology and phase formation in the as-SHS final product. In addition, the study of the effect of increasing compression forces and preheating temperatures on pore morphology and phase formation in the as-SHS final product is also included in this chapter.

6.1 Pore morphology of porous $NiTi_{100\%}$,

Figures 6.1 (a), (b) and (c) show the macrographs of a typical pore morphology and distribution of porous $NiTi_{100\%}$ in the uncut top view, cut top view and front view directions, respectively. In general, the pore morphology and distribution exist perpendicularly along the propagation direction and its cavities appear as arrays of circular conduits. This exhibited characteristics of isotropic and uniform banded structure of channels with smaller near circular or elliptical shape pores in between. The spin combustion that was described is similar to that used by Munir et. al. [49] and has shown to result in layered structure of porous parts (Figure 6.1 (a – b)). The porous $NiTi_{100\%}$ was examined in the cross-sectional direction and has found most of the pore characteristics existing three-dimensionally as interconnected pore structures in the final specimen porous as shown in Figure 6.1 (d).

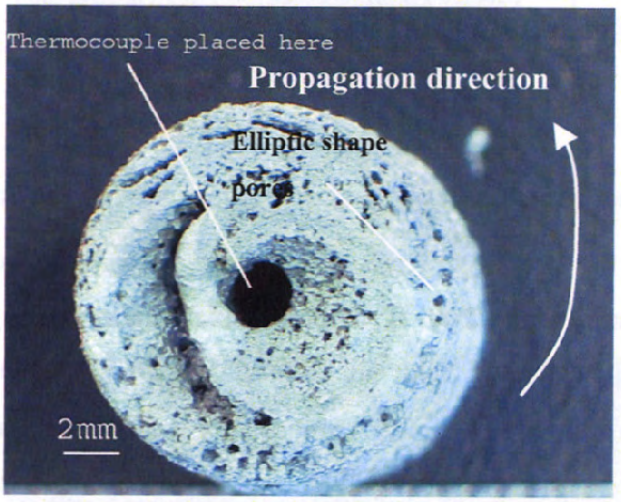

(a)

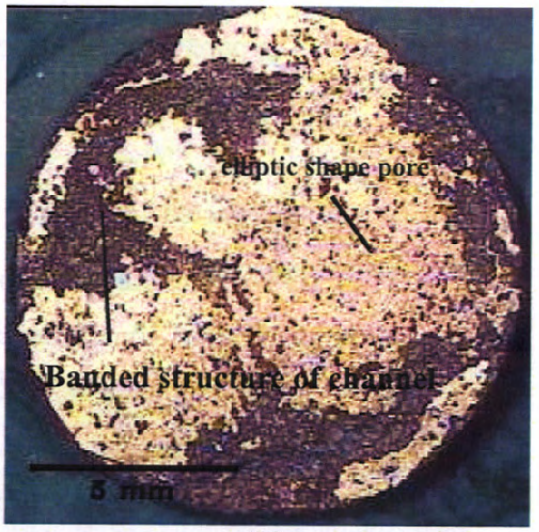

(b)

(c)

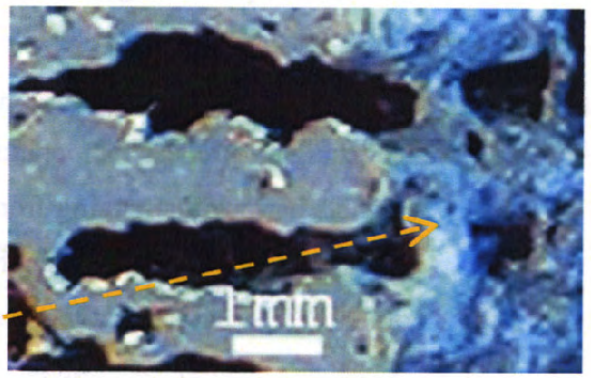

(d)

Figure 6.1 The pore morphology of typical porous $NiTi_{100\%}$, on (a) top view (b) cross-sectional top view (c) front view and (d) interconnected pore structure from micrograph.

6.2 The influence of green porosity, ε_g, on porous $NiTi_{100\%}$,

6.2.1 The pore size formation of porous $NiTi_{100\%}$ using reactants compacted at compression force of 8 kN

When compacted at 8 kN, the green compacted reactants had an average ε_g of 51 ± 1.3 vol.%. Figure 6.2 shows the interior structure of three porous $NiTi_{100\%}$ compacted at 8 kN synthesized constantly at temperature 200 °C. A closer examination of Figure 6.2 (i) shows ramification forming dendritical pore with smaller circular pores in between. The channels aligned normal to the direction of the combustion wave propagation which contradicted to the porous SHS NiTi by Li et. at [4]. Figure 6.3 shows the scatter plot chart for dimensions of the pores for the three compacts synthesised under identical conditions. Three porous $NiTi_{100\%}$ had channel widths ranging from 1 to 4.5 mm. The pore sizes of the near circular pores ranged from 100 to 800 μm. In addition, the average height of channels for the porous $NiTi_{100\%}$ at preheat temperature of 200 °C was 0.5 to 1.8 mm.

At the higher preheat temperature of 300 °C as shown in Figure 6.4, the band structure of channels had widths ranging from of 1 to 4 mm and average heights from 0.5 to 2.5 mm. A decrease in the width and height of the channel was observed when compared to that of porous $NiTi_{100\%}$ at preheat temperature of 200 °C.

The small deviation of ε_g had not influenced the final pore morphology formation in the final $NiTi_{100\%}$. However, the increase of preheating temperature influenced the pore morphology of the $NiTi_{100\%}$ which was due to the occurrence of surface tension energy in the melting phase at the higher preheat temperature.

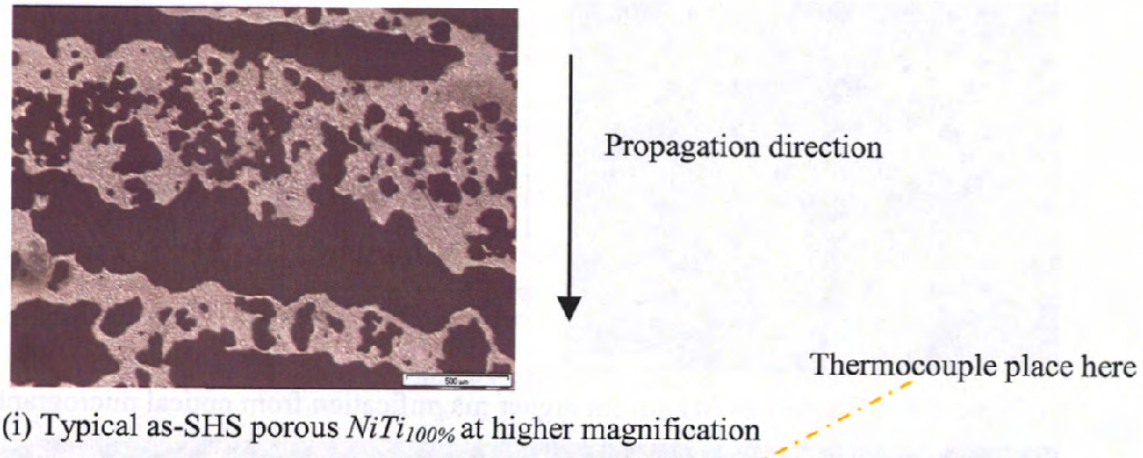

(i) Typical as-SHS porous $NiTi_{100\%}$ at higher magnification

(i) (a) Test run 1 (b) Test run 2 (c) Test run 3

Figure 6.2 The (i) optical micrograph and (ii) macrographs of porous $NiTi_{100\%}$ at compression force of 8 kN with deviation ± 1.3 vol.% of ε_g at three different test runs (ii a- c) at preheat temperature 200 °C.

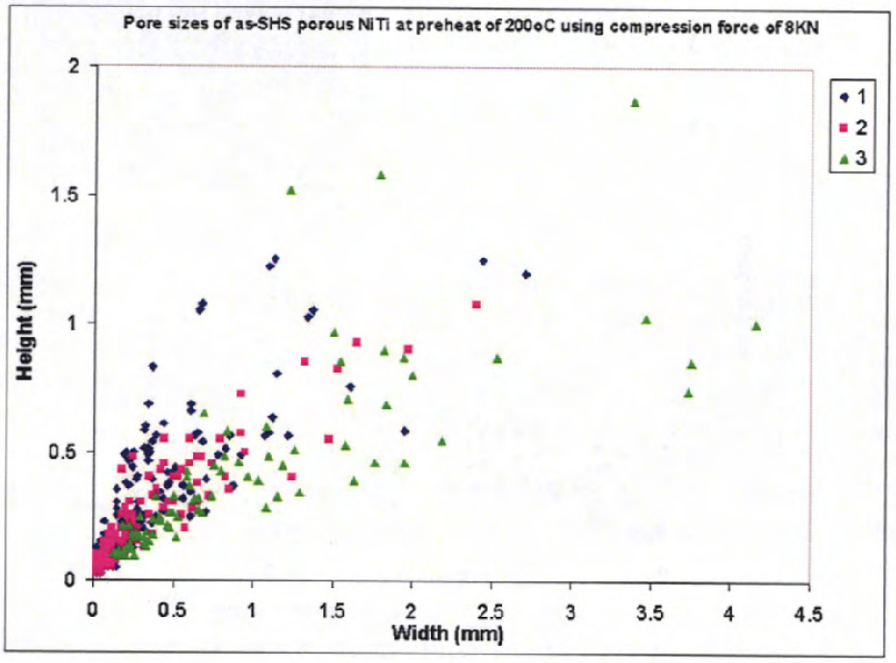

Figure 6.3 The scatter plot of pore sizes for the three test runs on porous $NiTi_{100\%}$ at preheat of 200 °C with deviation ± 1.3 vol.% of ε_g

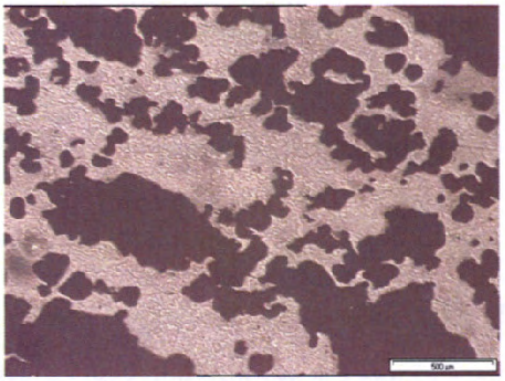

Propagation direction

(i)Typical as-SHS porous $NiTi_{100\%}$ at higher magnification from optical micrograph

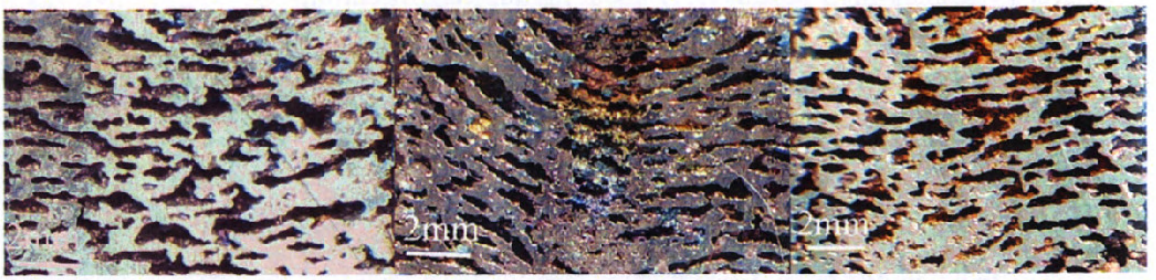

(ii) (a) Test run 1 (b) Test run 2 (c) Test run 3

Figure 6.4 The (i) optical micrograph and (ii) macrographs of porous $NiTi_{100\%}$ at compression force of 8kN with deviation ± 1.3 vol.% of ε_g for three different test runs (ii a- c) at preheat temperature 300 °C

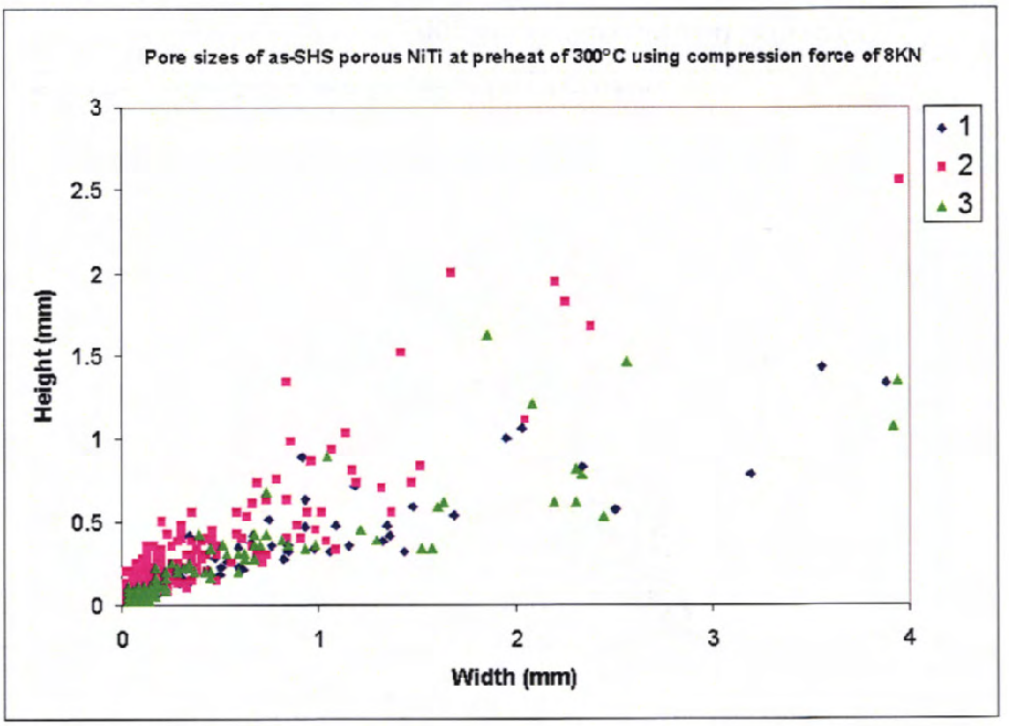

Figure 6.5 The scatter plot of pore sizes for the three test runs on porous $NiTi_{100\%}$ at preheat of 300°C with deviation ± 1.3 vol.% of ε_g.

6.2.2 The pore size formation of porous $NiTi_{100\%}$ using reactants compacted at compression force of 24 kN

The compression force of 24 kN for preheat 200°C, the compacted reactants obtained an average ε_g of 45 vol.% with a deviation of ± 2.5 vol.%. At the higher deviation of ε_g, there is still no major significant effect on the pore morphology of porous $NiTi_{100\%}$ as shown in Figures 6.6ii(a-c). Figure 6.7 shows the average width of channels ranging between 1 and 3.5 mm with an average height of 0.5 to 1.6 mm. Figure 6.6(i) shows presence of smaller and circular pores and lesser channels in the final porous $NiTi_{100\%}$. It is due to higher packing densities of compacted reactant obtained under higher compression forces. Increased preheating temperature to 300 °C resulted in additional smaller and circular pores formed in the final porous $NiTi_{100\%}$ as showed in Figure 6.8. In addition, the final porous $NiTi_{100\%}$ at preheating temperature of 300 °C had obtained an average width of channels ranging between 1 and 2.5 mm with a height ranging between 0.5 and 1.8 mm.

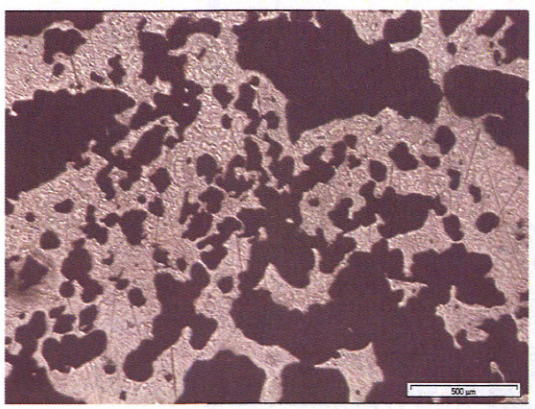

(i)Typical as-SHS porous $NiTi_{100\%}$ at higher magnification

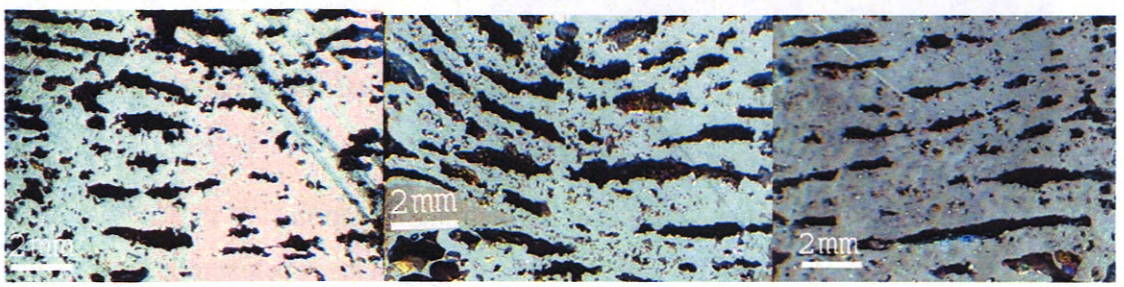

ii(a) Test run 1 ii(b) Test run 2 ii(c) Test run 3

Figure 6.6 The (i) optical micrograph and (ii) macrographs of porous $NiTi_{100\%}$ at compression force of 24 kN with deviation ± 2.5 vol.% of ε_g at three different test runs (ii a- c) at preheat temperature 200 °C.

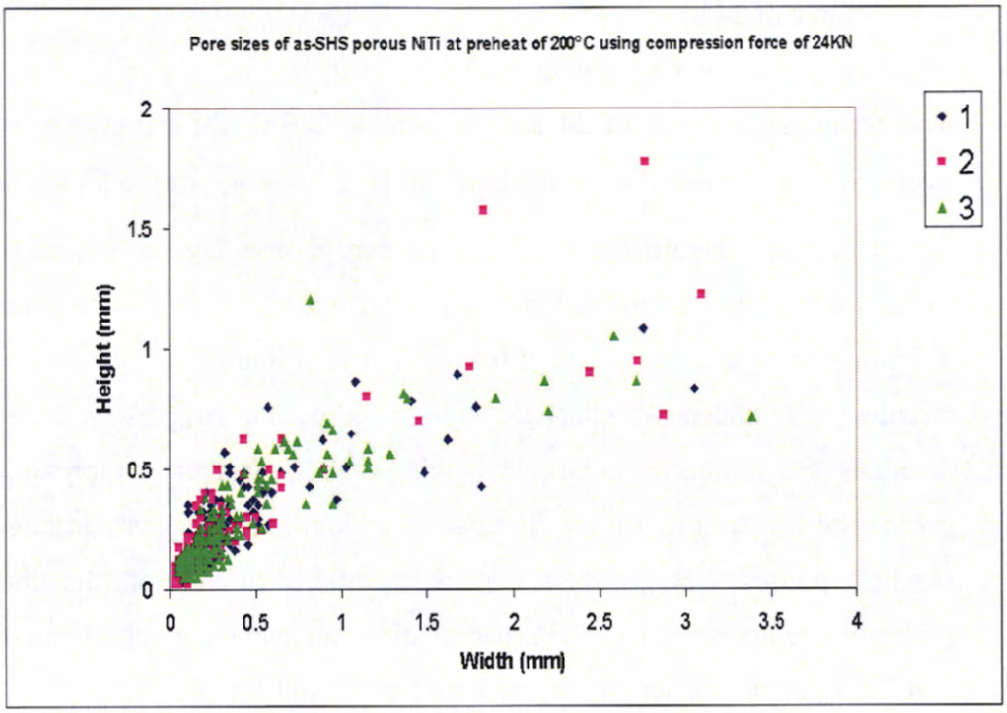

Figure 6.7 The scatter plot of pore sizes for the three test runs on porous $NiTi_{100\%}$ at preheat of 200 °C with deviation ± 2.5 vol.% of ε_g.

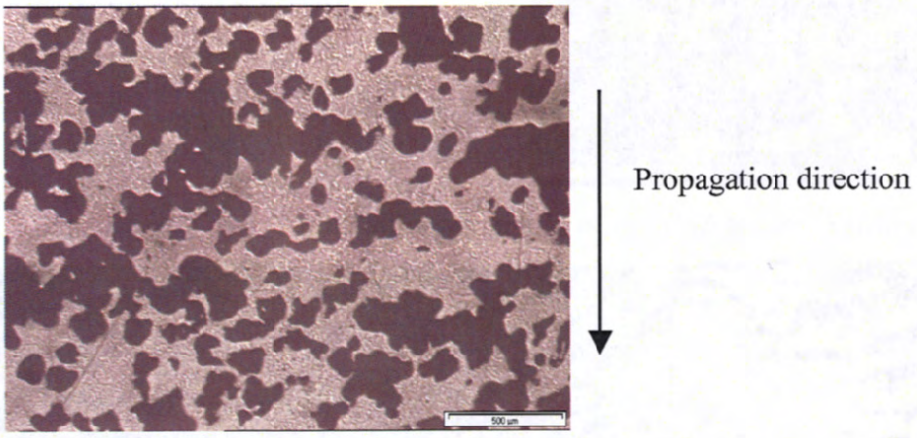

(i) Typical as-SHS porous $NiTi_{100\%}$ at higher magnification

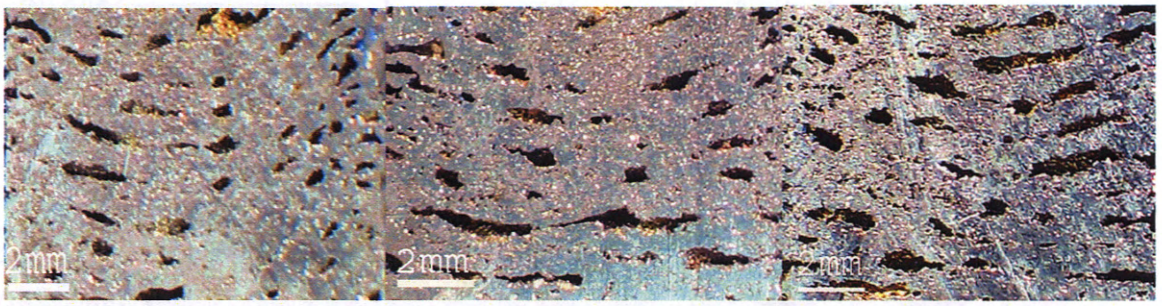

(a) Test run 1 (b) Test run 2 (c) Test run 3

Figure 6.8 The (i) optical micrograph and (ii) macrographs of porous $NiTi_{100\%}$ at compression force of 24 KN with deviation ± 2.5 vol.% of ε_g at three different test runs (ii a- c) at preheat temperature 300 °C.

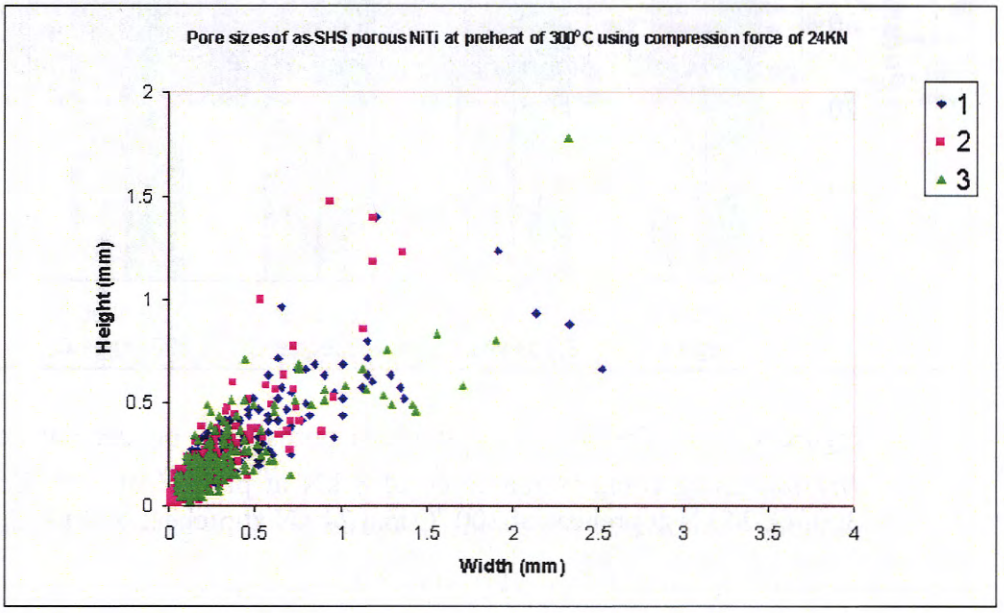

Figure 6.9 The scatter plot of pore sizes for the three test runs on porous $NiTi_{100\%}$ at preheat of 300 °C with deviation ± 2.5 vol.% of ε_g.

6.2.3 The general porosity ε of porous $NiTi_{100\%}$

The effects of ε_g on ε of porous $NiTi_{100\%}$ are shown in Figure 6.10. In most situations, having lower ε_g of compacted reactant will lead to lower ε of porous $NiTi_{100\%}$ in the final product.

A lower deviation of ε_g with ± 1.3 vol.% at the compression force of 8 kN obtained a ε of 58 ± 0.5 vol.% and 52 ± 2 vol.% in the final porous $NiTi_{100\%}$ at preheat temperatures of 200 °C and 300 °C, respectively. These are shown in Figure 6.10. The higher deviation of ε_g with ± 2.5 vol.% at the compression force of 24 kN obtained ε of 52 ± 1.4 vol.% and

43 ± 0.9 vol.% in the final porous $NiTi_{100\%}$ at preheat temperatures of 200 °C and 300 °C, respectively. The three similar compacted reactants used, had obtained a relatively consistent general porosity in the final porous $NiTi_{100\%}$.

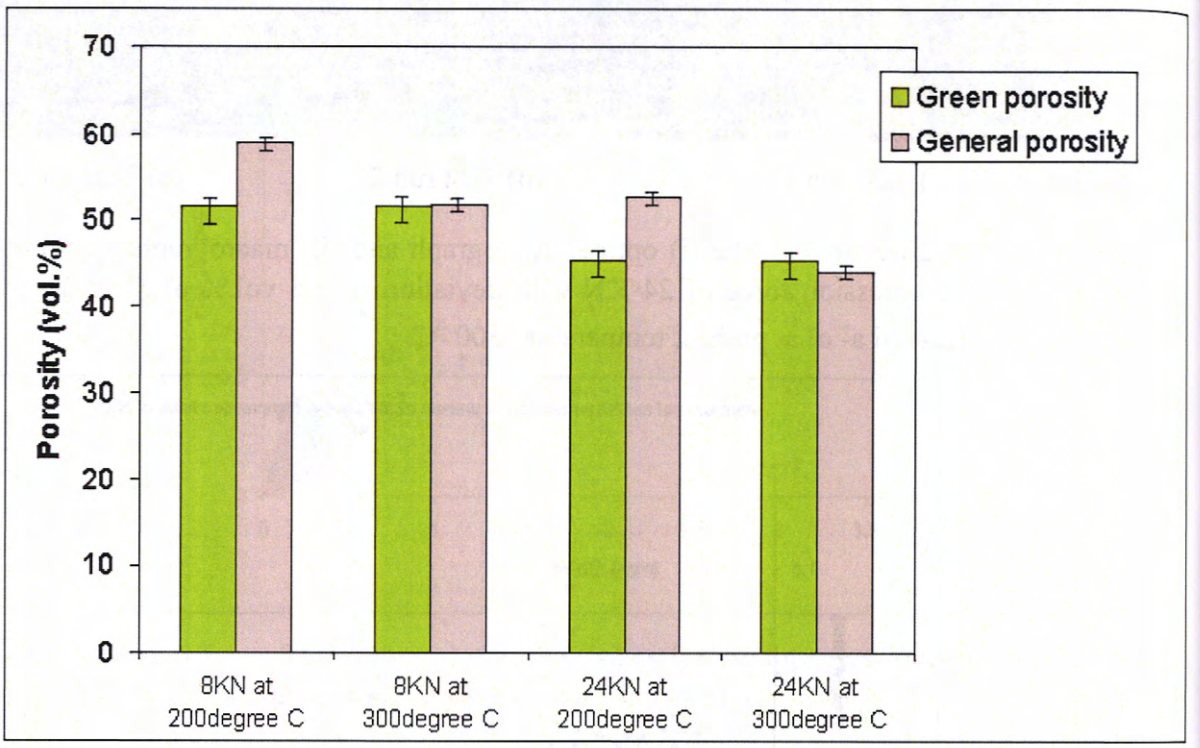

Figure 6.10 The influence of green porosity ε_g on general porosity ε of porous $NiTi_{100\%}$ using compression force of 8 kN at preheat of 200 °C, 8 kN at preheat of 300 °C, 24 kN at preheat of 200 °C and 24 kN at preheat of 300 °C.

6.2.4 The influence-of-height to diameter ratio, H/D

The effect of H/D ratio on the pore morphology of the final porous $NiTi_{100\%}$ using compacted reactants is shown in Figure 6.11. Generally, the pores in porous $NiTi_{100\%}$ are homogenously distributed in the final part. The smaller and circular pores mostly appeared at the outer sides of the final products which may be due to greater heat removal by the constant argon flow rate from the environment. The higher melting formation occurred at the higher temperature region from the ignitor results in most of the top segment of final product to be denser.

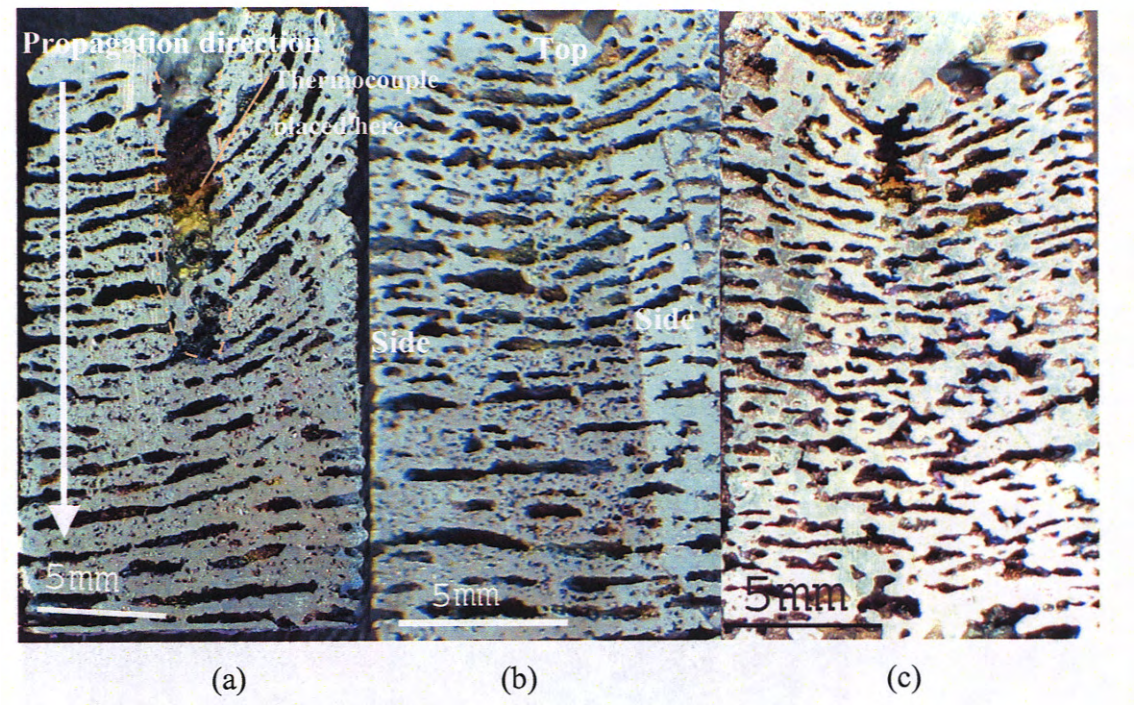

Figure 6.11 The macrographs of porous $NiTi_{100\%}$ with H/D ratio (a) 1.7 (b) 1.8 (c) 1.9 of compacted reactants.

6.3 The influence of compression force at 8,16 and 24 kN

The cross-sectional view from the macrographs of as-SHS porous $NiTi_{100\%}$ final products were presented in the Figure 6.12. Figure 6.12 shows the optical macrographs with a "X" to mark the locations of micrographs taken Figure 6.13. The outcome showed that an increase in compression force from 8 and 16 to 24 kN at preheating temperature of 200 °C had significantly decreased the sizes of the channels and ramification forming of dendritical pore structure presence in the final $NiTi_{100\%}$ products. This phenomenon can be seen in the Figures 6.13(a), (c) and (e). Likewise, this can also be observed in Figures 6.13(b), (d) and (f), showing that the decrease of pore sizes at the increased preheating temperature of 300 °C.

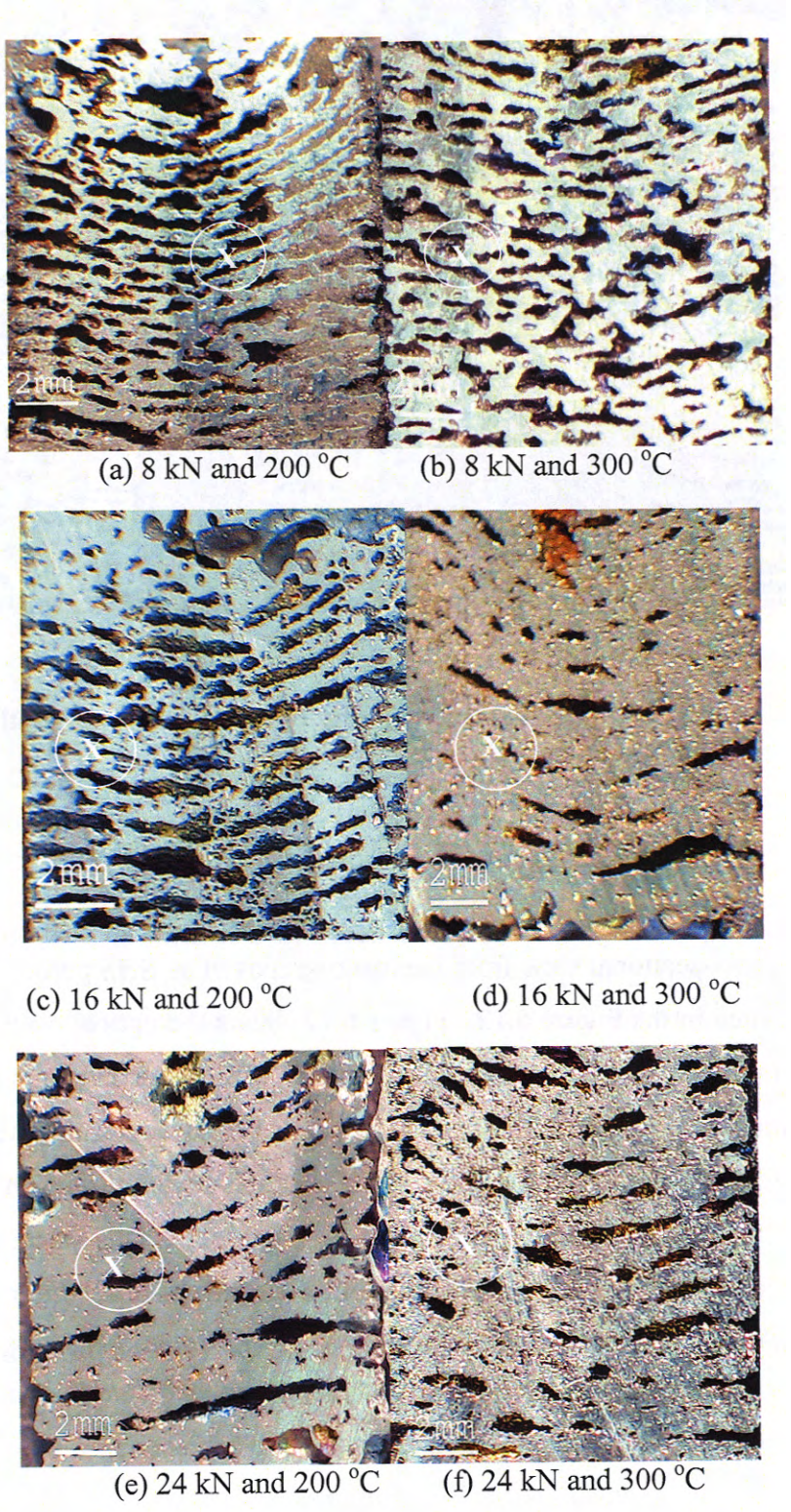

Figure 6.12 The pore morphology of porous $NiTi_{100\%}$ at various compression forces and preheat temperatures: (a), (b), (c), (d), (e) and (f) from the macrograph

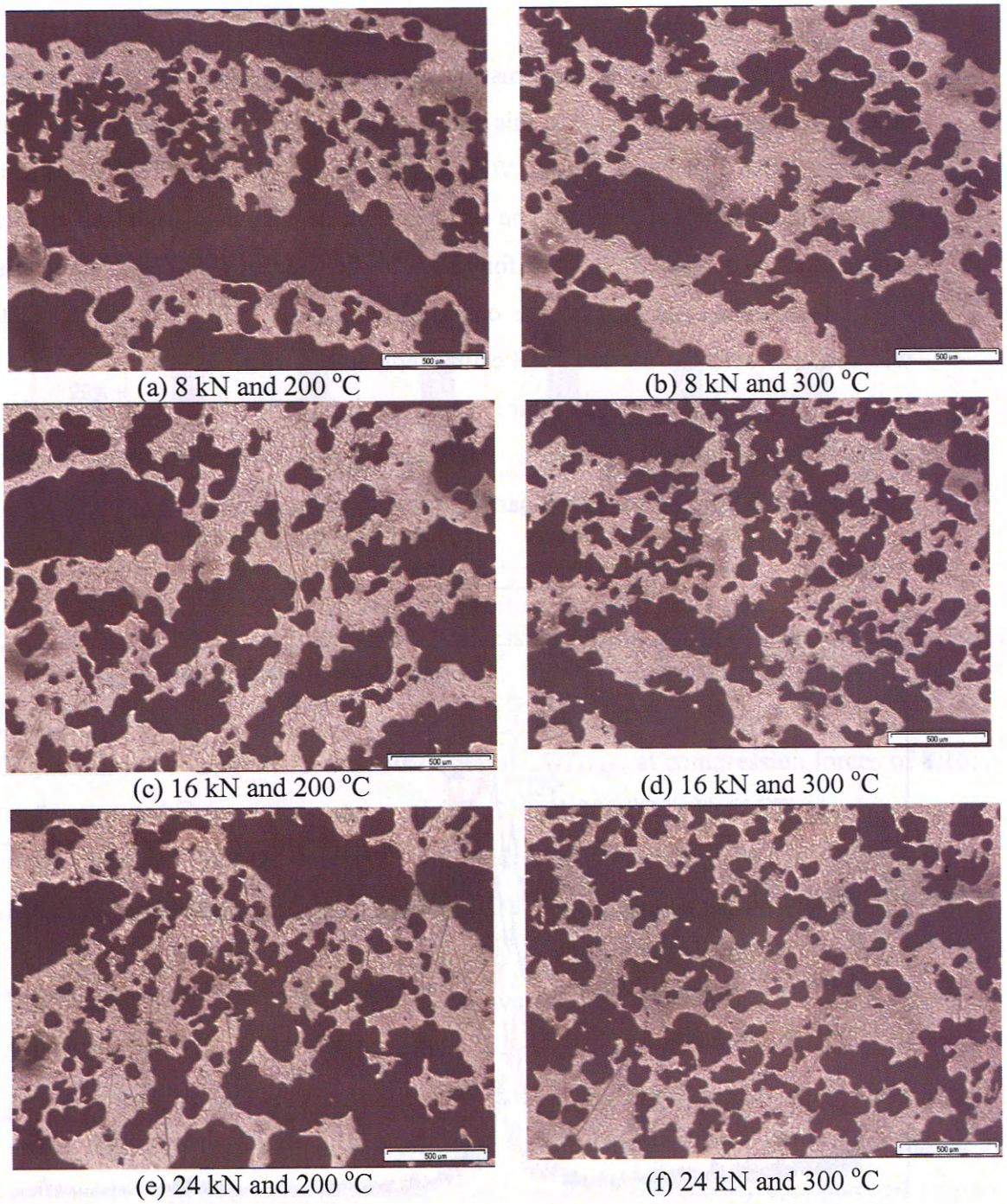

Figure 6.13 The pore morphology of porous $NiTi_{100\%}$ at various compression forces and preheat temperatures: (a), (b), (c), (d), (e) and (f) from the optical micrograph at the "X"-marked locations from Figure 6.12.

6.4 Analysis of phase formation of porous $NiTi_{100\%}$

Figure 6.14 shows the XRD patterns of the porous $NiTi_{100\%}$ at different compression forces and preheating temperatures. In this study, NiTi (B2) and NiTi (B19) were found to be the dominant phases in final porous $NiTi_{100\%}$ product in all cases. This dominant phases are generally desired in the product. The secondary phases like Ti_2Ni and undesirable by-product phase such as unreacted Ni were found in the final porous $NiTi_{100\%}$ product as shown the Figure 6.15. The unreacted Ni was observed in all cases. However, the unreacted Ni phase was reduced with the increase preheating temperature from 200 °C to 300 °C. This clearly indicated that preheating temperature has a great influence on the phase formation in the final product. In addition, by increasing compression forces, there was less influence on the phase formation in the final synthesized part.

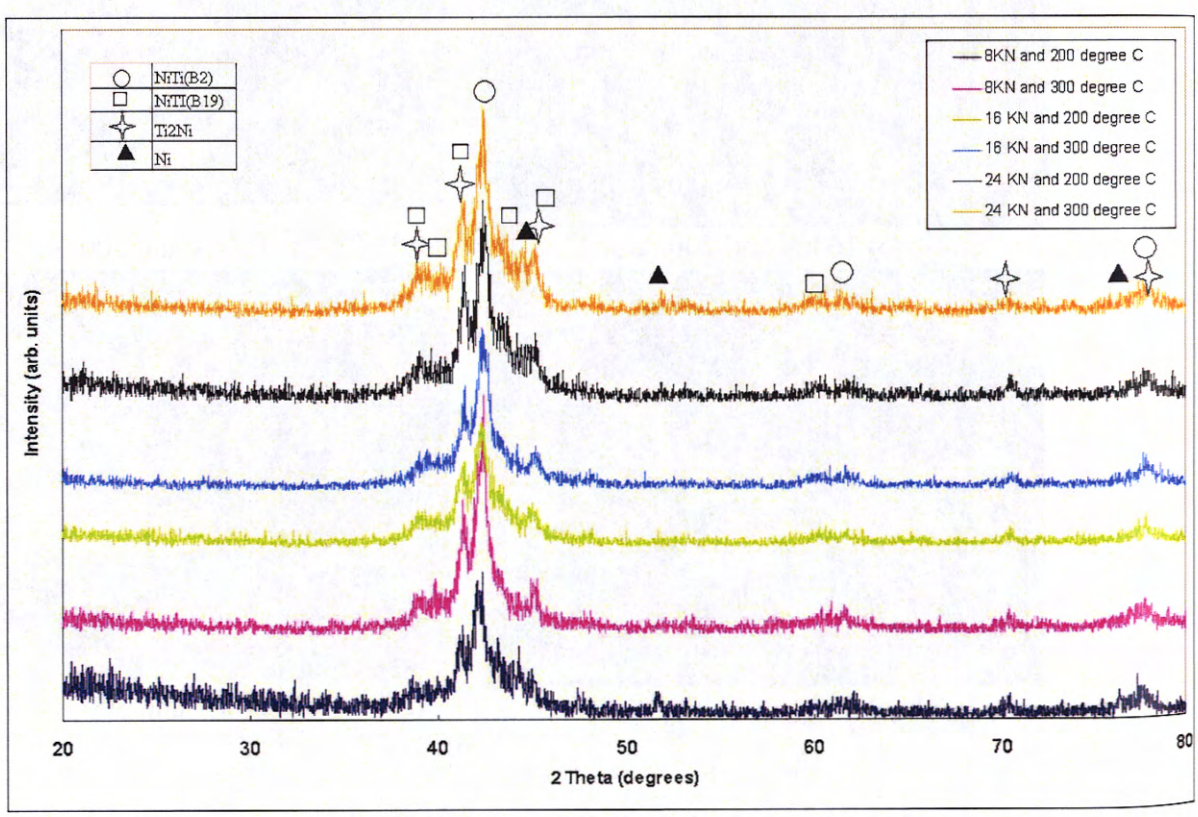

Figure 6.14 XRD spectra of porous $NiTi_{100\%}$ at compression forces of 8,16,24 kN and under preheating temperatures of 200 °C and 300 °C

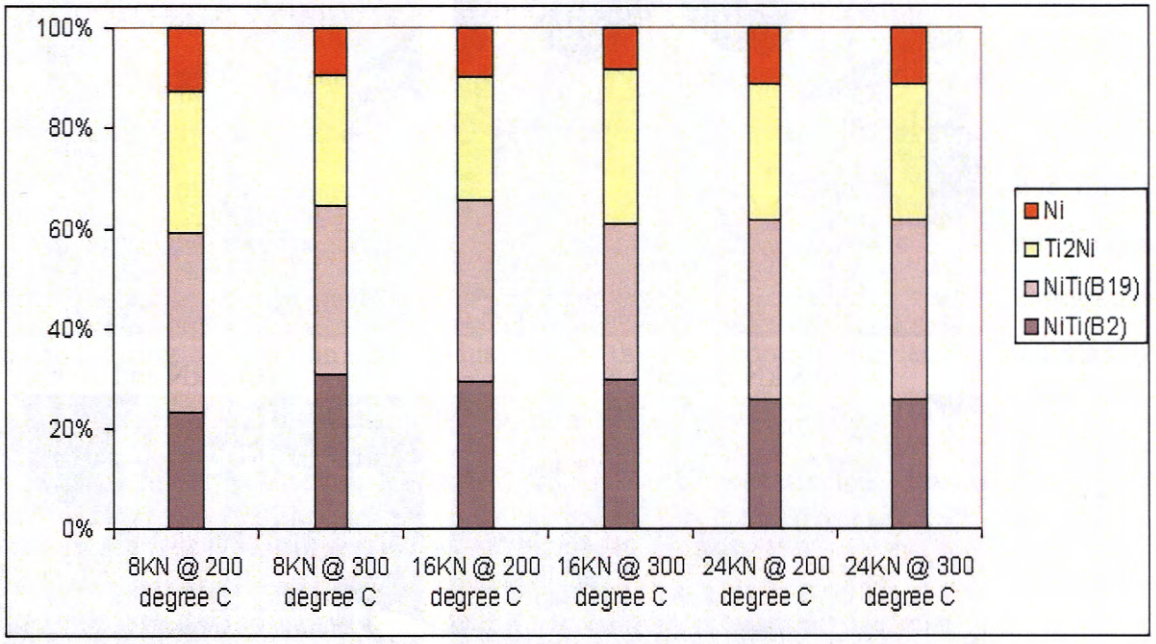

Figure 6.15 The chemical composition ratios in percentage of porous $NiTi_{100\%}$ from corresponding XRD results at compression forces of 8,16, 24 kN and under preheating temperatures of 200 °C and 300 °C.

Figure 6.16 shows the EDS analysis of porous $NiTi_{100\%}$ at compression forces of 8,16, 24 kN and under preheating temperatures of 200 °C and 300 °C. The NiTi phase appears in light grey colour and the EDS composition provided by EDS analysis is about Ti – 46 ± 2 at.% Ni which indicates slight excess of Ti. By EDS analysis, the composition Ti - 35 at.% Ni and Ti - 25 at.% Ni was found to be dark grey in dendritical shape and darker grey in elliptic shape respectively. From the EDS quantitative analysis, it can be concluded that the light grey colour corresponds to NiTi phase which covers most of the specimens shown in Figure 6.16 a-f. The dark grey dendritical shape and darker grey elliptic shape correspond to the Ti_2Ni phase. Figures 6.16 a-b show that the increase in preheating temperature from 200 to 300 °C significantly reduced the Ti_2Ni phase. This result corresponds to the chemical composition obtained from XRD patterns as shown in Figure 6.15.

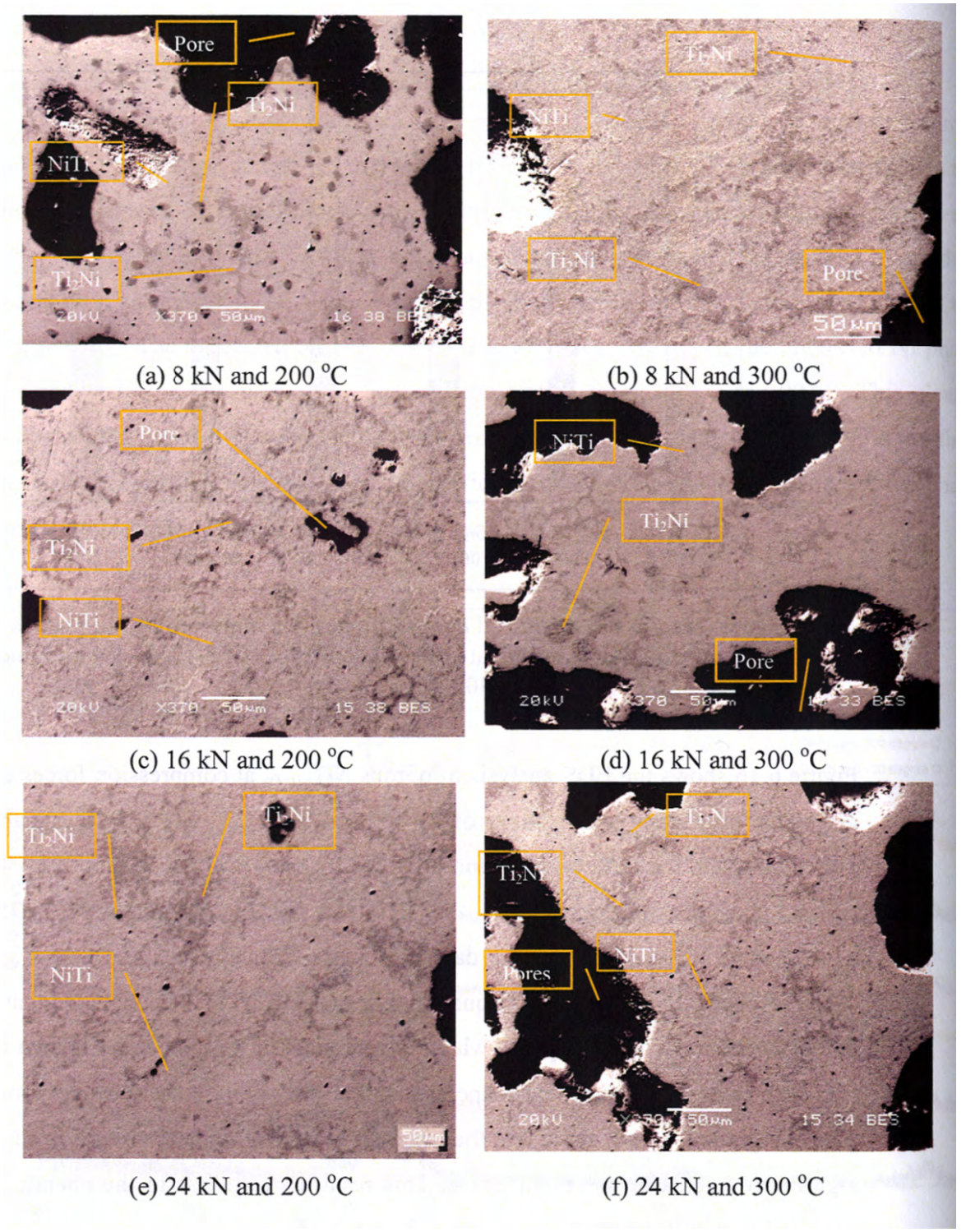

Figure 6.16 Back-scattered electron imaging (BEI) of porous *$NiTi_{100\%}$* at compression forces of 8,16, 24 kN and under preheat temperatures of 200 °C and 300 °C.

6.5 Conclusions

The pore morphology and distribution of most porous $NiTi_{100\%}$ specimens exhibited characteristics of three-dimensional interconnected uniform banded structures of channels consisting of smaller near circular or elliptic shape pores along the transverse direction (normal to the wave propagation direction). The powder shape and size of Ni and Ti powder particles used here may have caused the problem of agglomeration and size segregation occurred during compaction stage. This may be the main contribution leading to a maximum deviation of ε_g ± 2.5 vol.% obtained from the compacted reactants. However the deviation of ε_g and maximum setting H/D ratio of 1.9 had not affected pore morphology and distribution in the final porous $NiTi_{100\%}$ specimens significantly.

The increase of compression forces from 8 and 16 to 24 kN and preheating temperatures of 200 °C to 300 °C had significantly decreased the sizes of the channels and forming of dendritical pore presence in the final porous $NiTi_{100\%}$ products. In addition, the increase of compression force and preheating temperature decreased the general porosity of the synthesised final product.

The XRD results were confirmed by corresponding SEM and EDS investigations. In this study, NiTi (B2) and NiTi (B19) were found to be the dominant phases in the final porous $NiTi_{100\%}$ product in all cases due to the equiatomic Ni-Ti composition. The secondary phase such as Ti_2Ni and unreacted Ni were also found in the final product. The undesirable by-product phases of unreacted Ni was not eliminated with increased preheating temperature from 200 to 300 °C. However, the XRD and EDS results had indicated that preheating temperature has significant effected phase formation in the final product. However, the increase of compression forces showed little effect on the phase formation in the synthesised final product.

Based on the observation from the responses on the pore morphology and phase formation in the synthesized porous $NiTi_{100\%}$, Table 6.1 summaries the effect of variables on their pore morphology and phase formation responses.

Table 6.1 The parametric effects on the response of synthesized porous $NiTi_{100\%}$ products

Variables	**Responses**	
	Pore Morphology	*Phase Formation*
Increase in compression forces	• Pore size and ε decreased	• NiTi major phase increased
Increase in preheating temperatures	• Pore size and ε decreased	• Unreacted Ni decreased

CHAPTER 7 SHS USING NANOCRYSTALLINE REACTION AGENT

This chapter reports the effects of using nanocrystalline powder (as additive reaction agents) on the pore morphology and phase formation in SHS process.

7.1 The pore morphology of porous $NiTi_{MA25\%}$

Figure 7.1 shows the typical pore morphology and distribution of porous $NiTi_{MA25\%}$. The pores appeared typically small shaped as near-circular or elliptic pores were observed. The porous $NiTi_{MA25\%}$ was examined in the cross-sectional direction and found most of the pore characteristics existing three-dimensional interconnected pore structures in the final porous product.

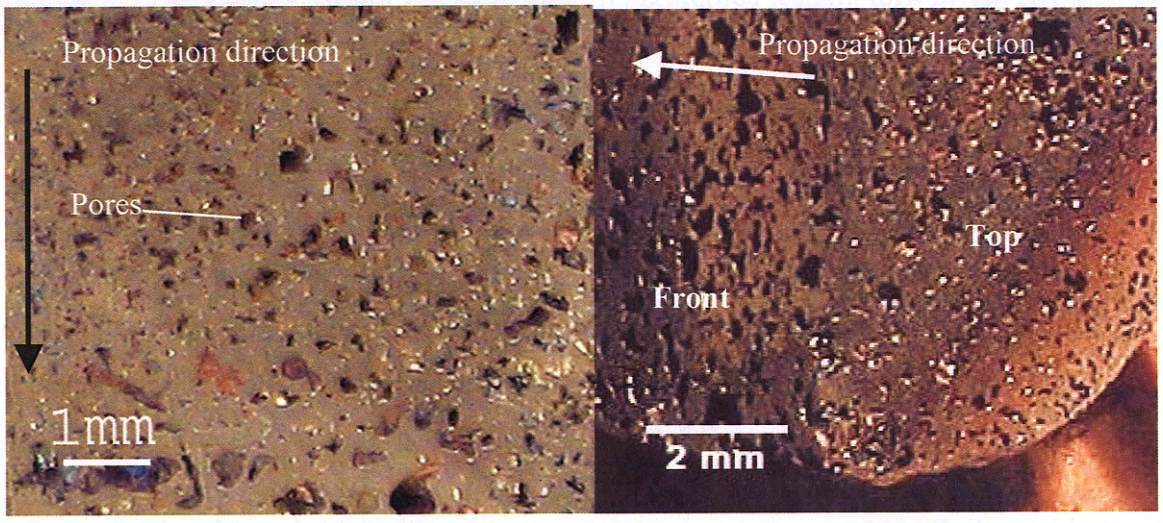

(a) (b)

Figure 7.1 Typical pore morphology and distribution of porous $NiTi_{MA25\%}$ in (a) cross-sectional plane, and (b) top with front directional views.

7.2 The pore morphology of porous $NiTi_{MA25\%}$ at compression forces of 8,16 and 24 kN

7.2.1 The effect of 200 °C preheat temperature in pore sizes of porous $NiTi_{MA25\%}$ specimens

Figures 7.2 (a)-(c) show SEM photography showing the pore morphologies of SHS porous $NiTi_{MA25\%}$ compacted at 8,16 and 24 kN and synthesised under preheat temperature of 200 °C. It can be seen from the micrographs that the pore shapes were similar to the ramification forming of dendritical pore structures surrounded by numerous smaller near-circular or elliptic pores shape as shown in Figure 7.2 (c). Figure 7.2 (d) shows that increased compression forces in the compact reactant have produced larger dendritical pore sizes and reduced the amount of the elliptic pores in the final porous $NiTi_{MA25\%}$ significantly. The porous $NiTi_{MA25\%}$ product at 8 kN compression force obtained a range of pore sizes between 100 μm and 550 μm. At compression forces of 16 kN and 24 kN, both the porous $NiTi_{MA25\%}$ obtained dendritical structured pores between 100 μm and 600 μm in size. The porous $NiTi_{MA25\%}$ with highest compression force of 24 kN formed the lowest general porosity.

7.2.2 The effect of 300°C preheat temperature on pore sizes in porous $NiTi_{MA\ 25\%}$ specimens.

Similarly, for parts synthesised at preheat temperature of 300 °C, there was an increased production of larger dendritical pore structures and reduction of elliptical pores in the porous part as shown in Figures 7.3 (a-c). Figure 7.3 (d) shows that porous $NiTi_{MA\ 25\%}$ obtained dendritical pore structures ranging from 100 to 300 μm, 100 to 490 μm and 100 to 500 μm at 8, 16, 24 kN compression forces respectively. The porous $NiTi_{MA25\%}$ obtained circular pores less that 100 μm under preheating temperatures of 200 °C and 300 °C.

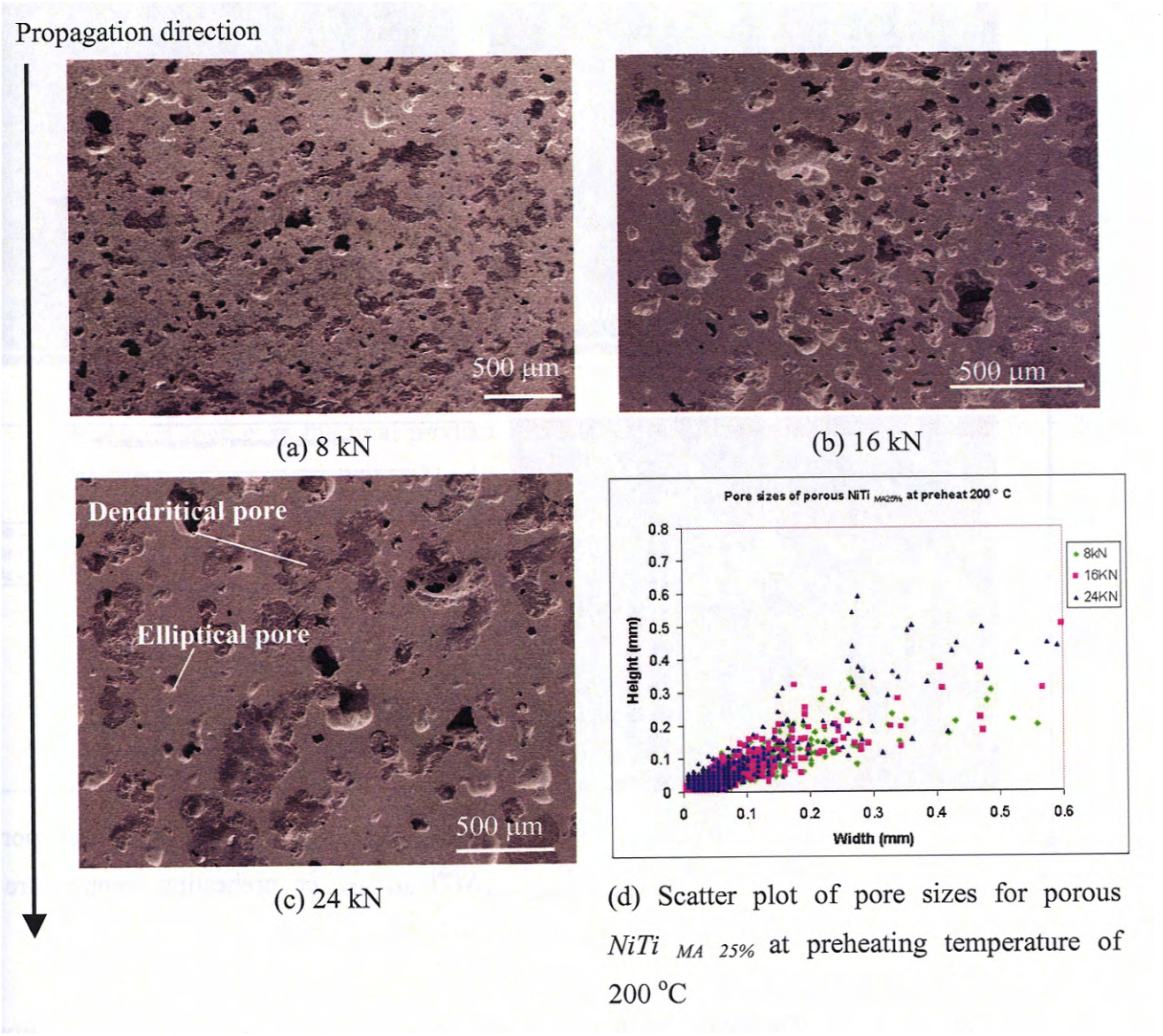

Figure 7.2 The pore morphologies of porous $NiTi_{MA25\%}$ at compression forces of: (a) 8 kN, (b) 16 kN, and (c) 24 kN with preheating temperature of 200 °C observed using from the SEM and (d) corresponding pores size distribution results from image analysis.

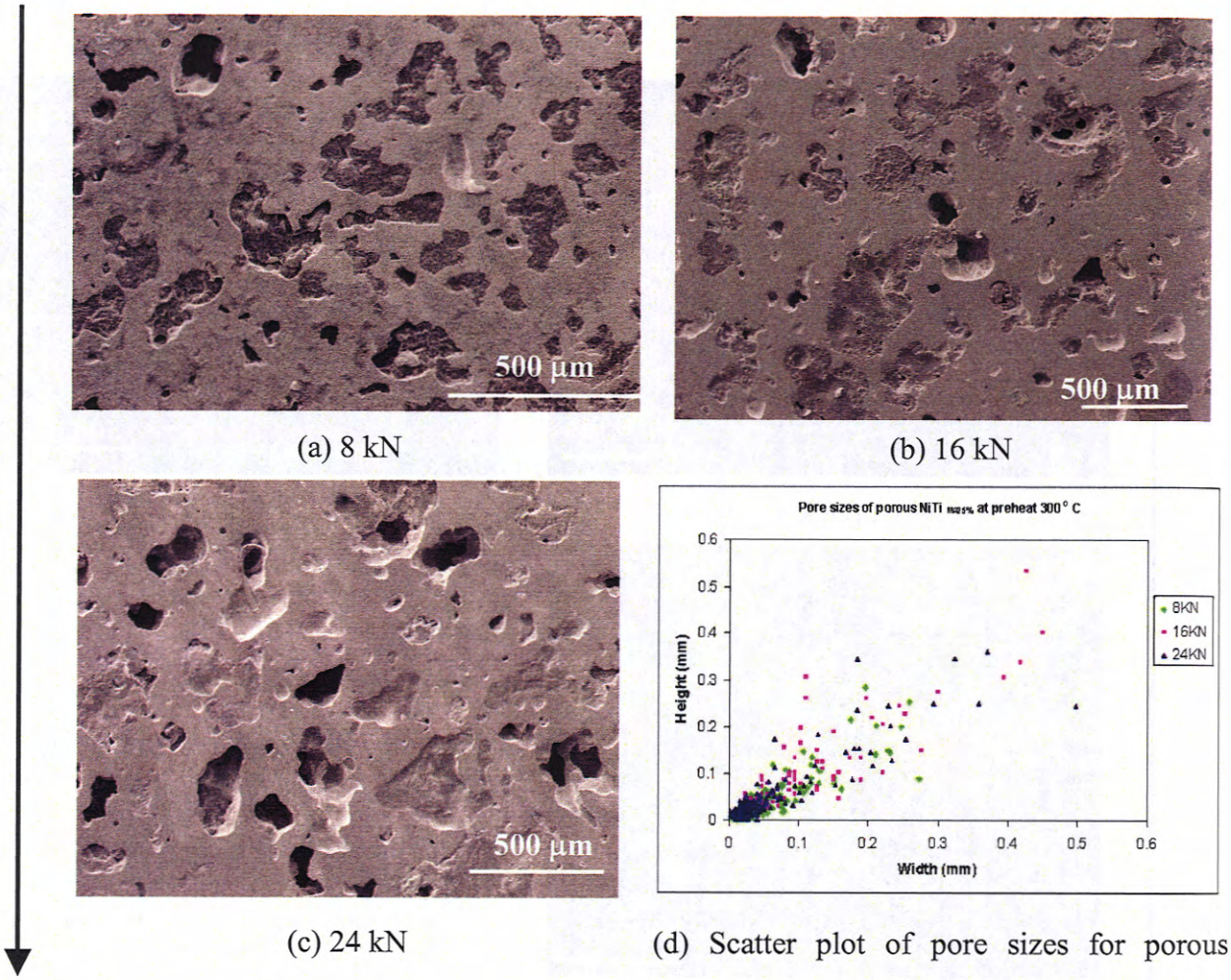

(a) 8 kN

(b) 16 kN

(c) 24 kN

(d) Scatter plot of pore sizes for porous *NiTi* $_{MA\ 25\%}$ *at* preheating temperature of 300 °C

Figure 7.3 The pores morphology of porous $NiTi_{MA25\%}$ at compression forces of: (a) 8 kN, (b) 16 kN, and (c) 24 kN with preheating temperature of 300 °C observed using from the SEM and (d) corresponding pores size distribution results from image analysis.

7.2.3 The general porosity, ε, of porous $NiTi_{MA25\%}$

Figure 7.4 shows the effects of compression force and preheating temperature on ε. At preheating temperature of 200 °C, the general porosities of 58, 55 and 52.53 vol.% were obtained in porous $NiTi_{MA25\%}$ specimens at compression forces of 8, 16, and 24 kN, respectively. At preheating temperature of 300 °C, the general porosities of 59, 57 and 55 vol.% were obtained in porous $NiTi_{MA25\%}$ specimens where compression forces at 8, 16, and 24 kN respectively. Thus, in most of the cases, a low ε_g in compacted reactant would lead to a low ε in the final product. As the preheating temperature increased from 200 to 300 °C, ε also decreased in the as-SHS parts.

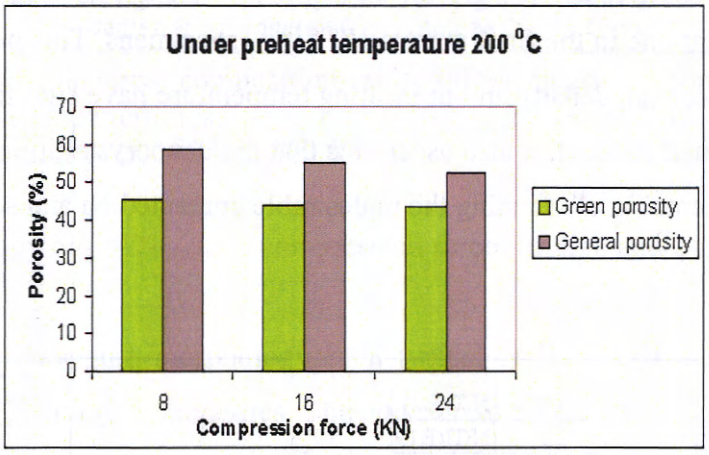

(a)

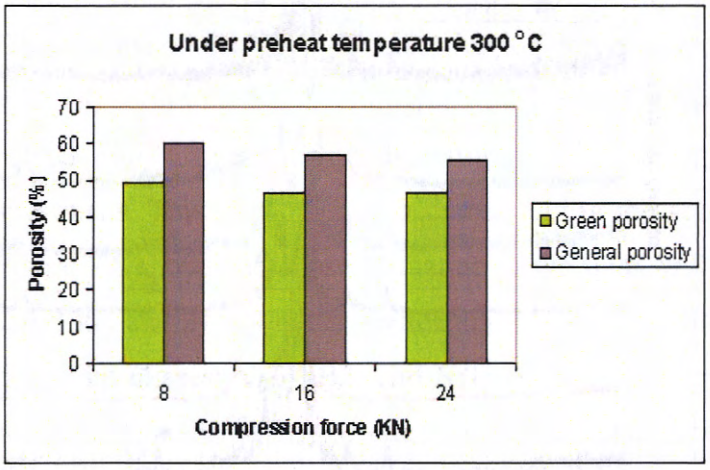

(b)

Figure 7.4 The influence of green porosity, ε_g, on general porosity, ε, of porous $NiTi_{MA25\%}$ using compression forces of (a) 8, 16 and 24 kN at preheat temperature of 200 °C, and (b) 8, 16 and 24 kN at preheat temperature of 300 °C.

7.3 Analysis of phase formation of porous $NiTi_{MA25\%}$

Figure 7.5 shows the XRD patterns of porous $NiTi_{MA25\%}$ specimens compacted at various compression forces and synthesised at different preheating temperatures. The analysis shows that NiTi (B2) and NiTi (B19) were found to be dominant phases with secondary phases (Ti_2Ni and Ni_3Ti) present in all cases. Porous parts prepared by 8 kN of compression force and synthesised at preheating temperatures of 200 and 300 °C were found to have the Ni_3Ti phase. The undesirable unreacted Ni was detected in the final product at low compression forces of 8 and 16 kN under preheating temperature of 200 °C. However, by increasing the compaction force and preheating temperature, the unreacted Ni and secondary phase Ni_3Ti were eliminated as shown in Figure 7.5. In doing so, the desired NiTi phase existed as the dominant one in the final porous $NiTi_{MA25\%}$ specimens. This not only clearly indicates that the initial reactant density and preheating temperature have significant effects on phase formation in the final product, it also ascertains that the nanocrystalline reaction agent by MA process is instrumental in eliminating the undesirable unreacted Ni and secondary phases.

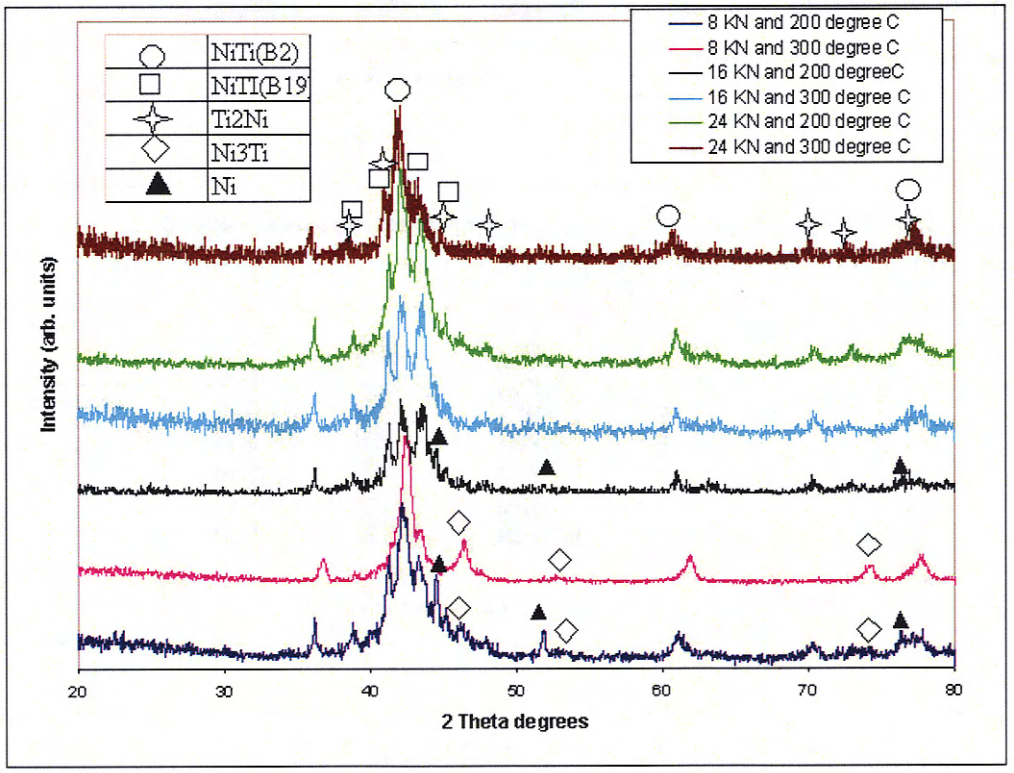

Figure 7.5 XRD spectra of porous $NiTi_{MA25\%}$ at compression forces of 8,16, 24 kN and preheating temperatures of 200 °C and 300 °C

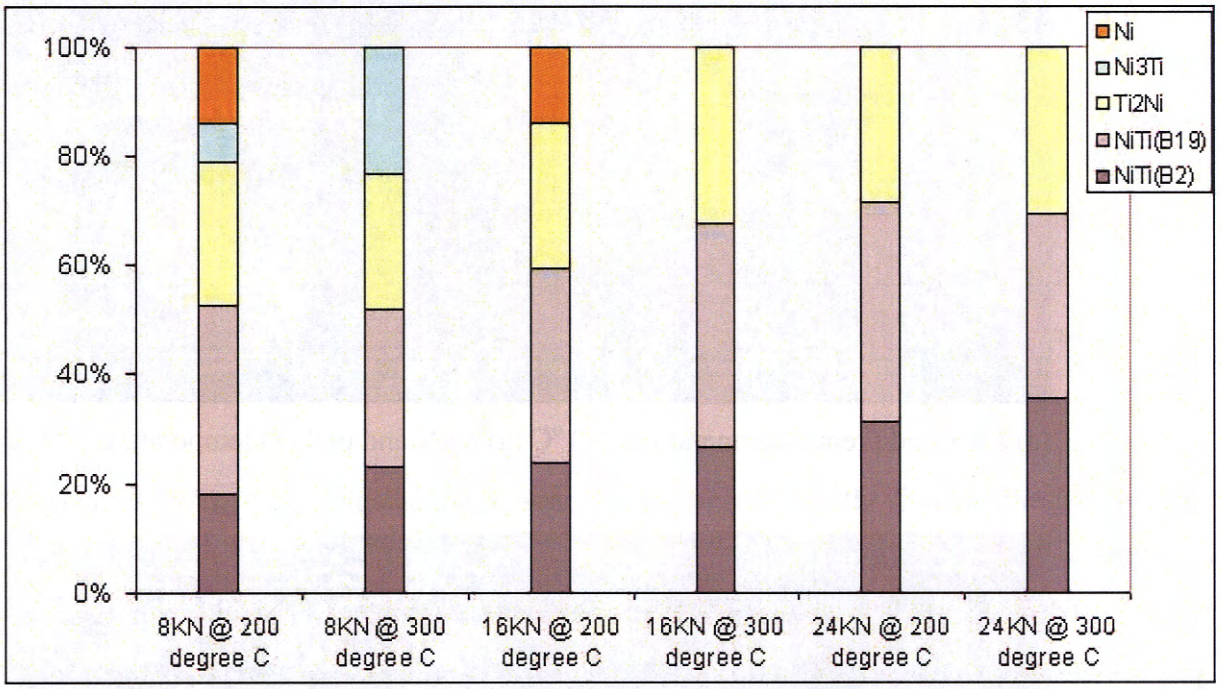

Figure 7.6 The chemical composition ratios in percentage of porous $NiTi_{MA25\%}$ from correspondence XRD pattern results at compression forces of 8,16, 24 kN and under preheating temperatures of 200 °C and 300 °C.

7.4 The morphology on $NiTi_{MA50\%}$ at compression forces of 8,16 and 24 kN

Figures 7.7 (a)-(d) show the morphology of a typical $NiTi_{MA50\%}$ at different compression forces and under preheating temperatures. The addition of 50% volume fraction mechanically alloyed nanocrystalline Ni-Ti powders in the reactant generally produced dense parts as shown in Figure 7.7 (a). Figure 7.7 (b) shows spatial dendrite structures and nodules that lie within the final $NiTi_{MA50\%}$ specimens at 8 kN compression force under 200 °C preheating temperature. Figure 7.7 (d) shows the SEM micrograph of final $NiTi_{MA50\%}$ specimen at 24 kN compression force under 300 °C preheating temperature. A dendrite structure is generally observed in these specimens. This phenomenon occurred during the solidification stages of the SHS process. Figure 7.8 shows the phase formation in the final $NiTi_{MA50\%}$ product at the compression forces of 8 kN and 24 kN under preheating temperatures of 200 °C and 300 °C respectively. The dominant phases: NiTi (B2) and NiTi (B19) and secondary phases: Ti_2Ni and Ni_3Ti are observed in the final $NiTi_{MA50\%}$ product. No undesirable unreacted Ni was found in the $NiTi_{MA50\%}$ final product in all specimens.

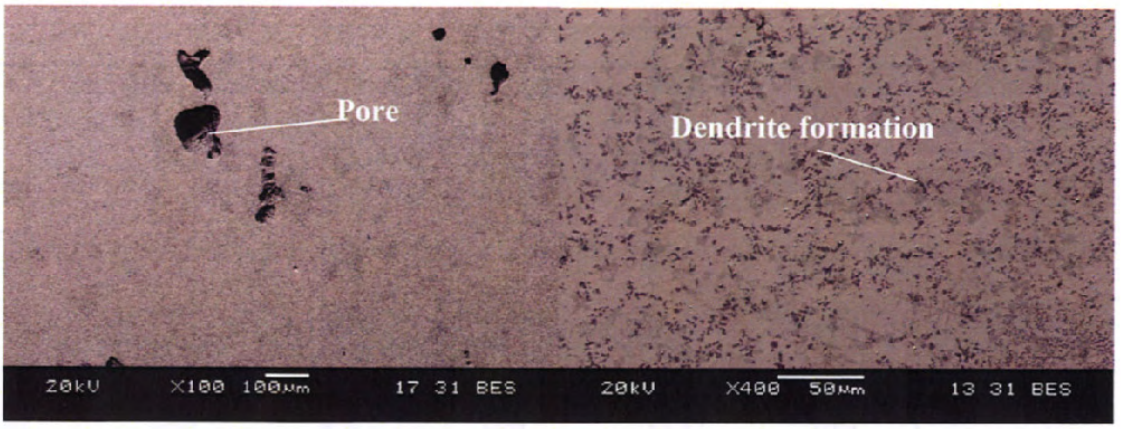

(a) 8 kN and preheat temperature 200 °C (a) 8 kN and preheat temperature 300 °C

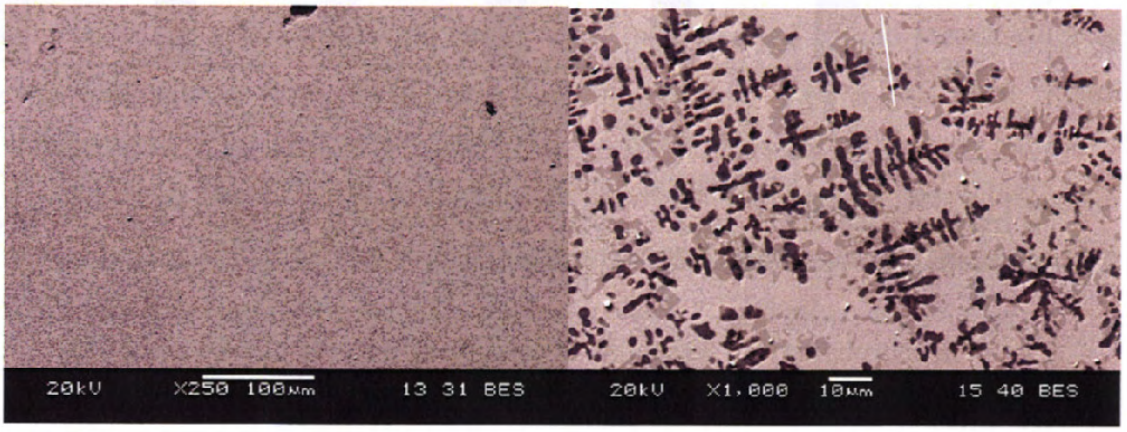

(c) 24 kN and preheat temperature 200 °C (d) 24 kN and preheat temperature 300 °C

Figure 7.7 The typical morphology of $NiTi_{MA50\%}$ products at different compression forces and preheating temperatures: (a), (b), (c) and (d) from SEM micrograph.

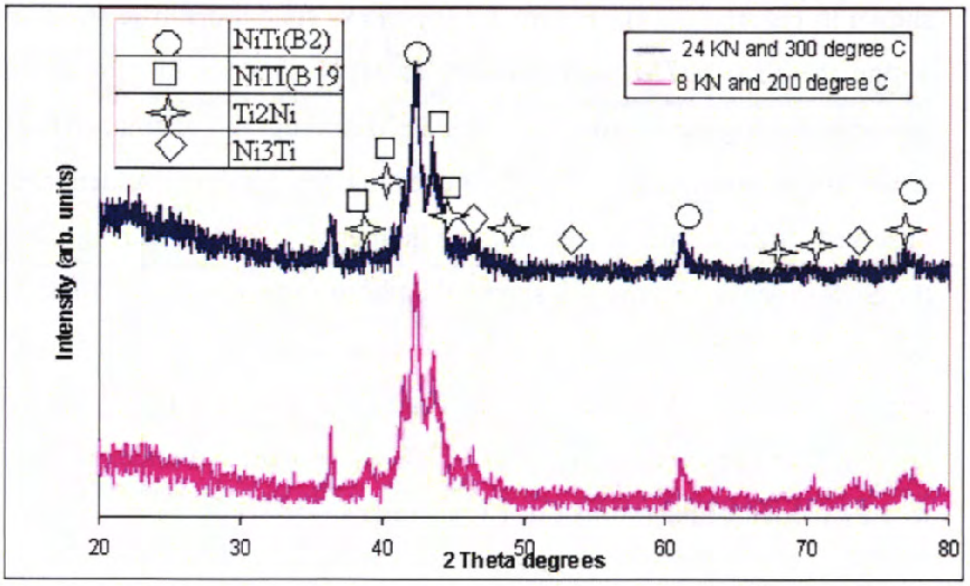

Figure 7.8 XRD spectra of porous $NiTi_{MA50\%}$ at compression forces of 8 and 24 kN and under preheating temperatures of 200 °C and 300 °C respectively

7.5 Conclusions

SHS parts of 25% additive of nanocrystalline reaction agent in the reactant ($NiTi_{MA25\%}$) produced porous parts with dendritical pore shaped like ramifications surrounded with numerous smaller near-circular or elliptic pores. The average pore size ranged from 100 to 600 μm with general porosities of between 52 and 58 vol.% obtained at compression forces from 8 to 24 kN under preheating temperatures of 200 °C and 300 °C.

Reactant of $NiTi_{MA25\%}$ eliminated the presence of unreacted Ni in the final synthesized product at both preheating temperatures of 200 °C and 300 °C. The synthesized $NiTi_{MA25\%}$ increased proportionally the NiTi main phase and reduced the secondary phase of Ti_2Ni. Further increase of nanocrystalline reaction agent to 50% volume fraction eliminated the unreacted Ni but formed an overly dense NiTi part. This phenomenon is due the to increase exothermic energy within the higher-content MA NiTi that leads to an increased melting of the product during the second stages of combustion synthesis by capillary mode. Thus, most of the melt has rapidly wet and spread throughout the reaction front due to capillary forces and filled up the voids between the particles.

Based on the observations in the addition of nanocrystalline reaction agent on the final SHS product, the effects of process parameters on the pore and phase formations are summarized in Table 7.1.

Table 7.1. The parametric effect on the responses by nanocrystalline reaction agent

Variables	**Responses**	
	Pore Morphology	*Phase Formation*
Increase in compression forces	• Pore size increased • ε decreased	• NiTi content phase increased • Decreased of Unreacted Ni
Increase in preheating temperatures	• Pore size decreased • ε decreased	• NiTi major phase increased • Unreacted Ni eliminated

CHAPTER 8 MECHANISMS OF PORE AND PHASE FORMATION

This chapter discusses the mechanisms of pore morphology and phase formation using elemental reactants. In addition, the hypothetical explanation of additive nanocrystalline reaction agent and its influence on SHS process is also included in this chapter.

8.1 Pore formation

Pore formation in SHS could be contributed to gas phase flow, original porosity, diffusion reaction and liquid phase during combustion synthesis. Pore formation in porous NiTi when using elemental powder could be attributed to the following reasons:

1) The volatilization of low melting impurities in the raw powder which was blended by tumbler mixer.

2) The entrapped gas in the powder during outgassing, the material particle will flow and this generated pores. If the entrapped gas pressure was low, then closed pores are formed.

3) The compaction process involves not only both rearrangement and deformation of particles, it also leads to the development of interparticle bond. This decreases the porosity and increases the coordination number of powder particles. Therefore the number of contact points between Ti and Ni particles is increased. The original pores formed during the compaction process then create the pore in the final porous product during the combustion process.

4) When the combustion temperature is lower than the temperature to form a liquid phase, the solid–solid diffusion of the reactants become dominant during processing. The diffusion rate of nickel atom in titanium atom is 4000 times than vice-versa at 900 °C [37]. Once nickel is ignited, which has a melting point of 1455 °C, the volumetrically lower refractory element of the reactant mixture commences to diffuse as compared to Ti which has a meting point of 1670 °C. This was then followed by the diffusion of the molten element into the more refractory element (i.e. Ti) forming NiTi intermetallics. This leaves a vacancy at the Ni site,

hence the creation of pores in the final SHS synthesised part occurs as illustrated in Figure 8.1 (a) to (b).

This phenomenon occurs during the different diffusion rates of these two species (Ni and Ti) at an elevated temperature which known as "Kirkendall effect". The pores that were created by this effect are named "Kirkendall pores".

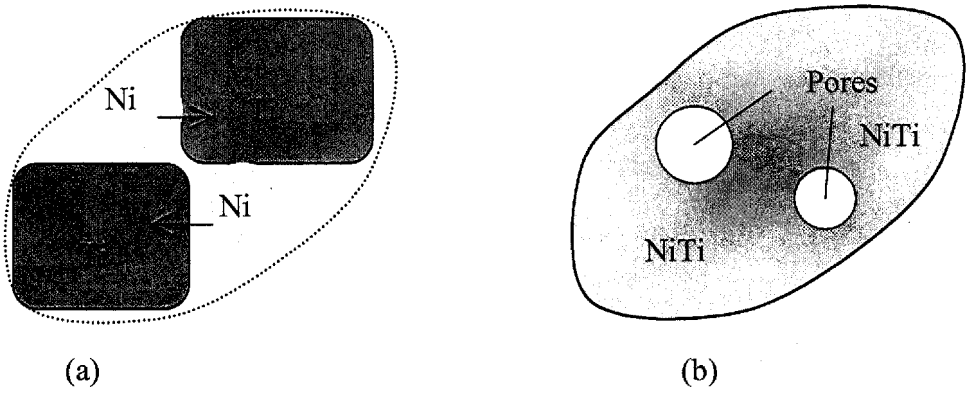

Figure 8.1 The simplified of illustration of the Kirkendall effect during solid-solid diffusion reaction.

8.1.1 The proposed explanation on the mechanisms of pore morphology formation using elemental reactant and nanocrystalline reaction agent

There are two stages in the combustion synthesis of SHS process [5]. The first stage corresponds to the propagation of the self-sustained flame-front where the reaction takes place. The second stage signifies a prolonged bulk combustion period during the SHS process.

Because of the high combustion temperature, there is a high thermal gradient across the combustion in the direction of propagation. Any liquid phase generated during combustion will inevitably flow along the propagating direction. As the liquid flows, pores were formed. Under ideal condition (along the propagation direction), arrays of circular conduits will form. However in practice, any perturbation due to the heat loss of inhomogeneous chemical composition could cause ramification resulting in dendritical pores which were seen in the final $NiTi_{100\%}$ product when using of elemental reactant (ref. chapter 6).

If preheating temperature was sufficient, the reactant absorbed adequate energy. This could have proper fraction of liquid phase causing enough expansion of gas and proper resistance of liquid flow. With this a porous NiTi sample with isotropic, uniform pore morphology and distribution can be obtained.

If the preheating temperature was too high, the reactant absorbed superfluous energy. This could have yielded a bigger fraction of the liquid phase for exceeding expansion of gas and resistance of liquid flow. This results in porous NiTi containing an anisotropic and asymmetric pore morphology and distribution in the final ($NiTi_{MA25\%}$ product using of nanocrystalline reaction agent as reactant).

Based upon the results obtained from increasing nanocrystalline Ni-Ti reaction agent to 50% in the reactant, it is recommended that a higher combustion temperature can be obtained from the highly stored enthalpy of reaction agent during SHS [13, 64]. Subsequently, this causes large amounts of molten liquid to form at the combustion front and diffuse within the porous reactant, which enhances both heat and mass transfer thus leading the second combustion stage. At this flame propagation stage, dense sample products in final $NiTi_{MA50\%}$ were produced.

The capillary mode: second stage of combustion synthesis.

The influence of the green porosity of the reactant is more significant at the second stage which is dominated by capillary spreading mode and leads the prolonged bulk combustion. This capillary mode has similar analogue as the capillary tube. In the capillary tube, capillary rising in the narrow tube is based on the balance surface energy and the gravitational force.

In capillary mode, the combustion synthesis is controlled by the rate of the capillary spreading of the molten phase (metal) through the reactant particle. The magnitude of the capillary force depended on the surface energy due to contact angle (wettability) between the liquid and solid phase. In addition, the capillary force also depends on the liquid volume fraction. If the contact angle (θ) is large, the liquid between two solid particles form a convex shape as shown in Figure 8.2(a). This will generate a repulsion by compressive forces. In contrast, an attractive force is generated when the liquid has low θ with respect to the solid as shown in

Figure 8.2b. The magnitude of the capillary force depends on the curvature of the liquid phase shape, the surface energy and the liquid volume fraction. The more curved the surface, the greater the attractive force. Thus, a smaller volume of liquid gives a greater force. Likewise, higher surface energies increase capillary forces.

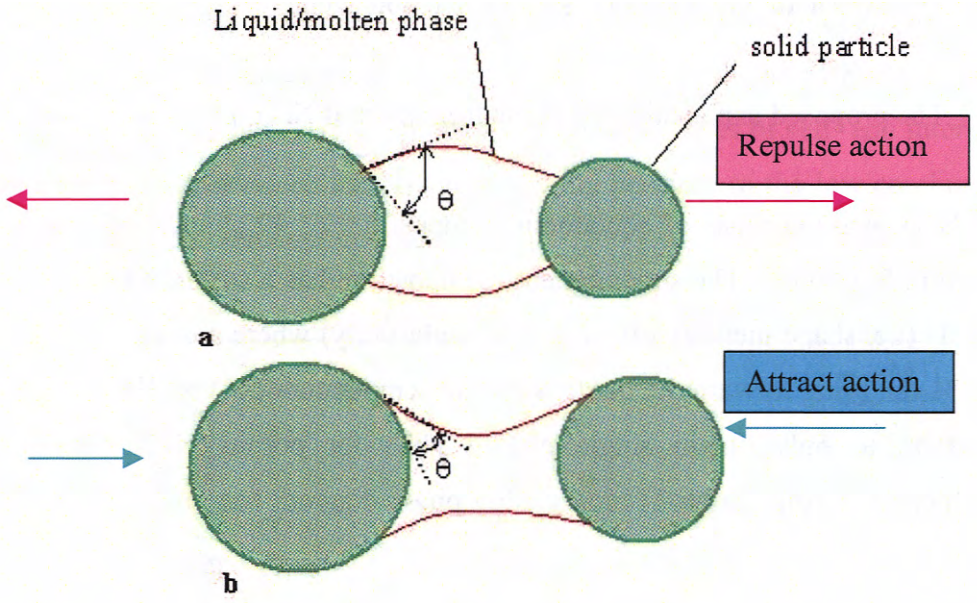

Figure 8.2 The schematic illustration on the effect of wettability on the force between particle (a) repulsion at large θ (b) attraction at a low θ.

By understanding the capillary mode behaviour in the combustion synthesis, this can lead to the explanation of the effect of nanocrystalline reaction agent in the SHS process.

In mechanically alloyed nanocrystalline Ni-Ti powder, a higher level of energy was introduced in the particles as atoms re-arranged themselves in the cores of defects in the grain boundaries, interphase boundaries or dislocations [13]. As the highly exothermic reaction was generated with the small crystallite size (in the order of 10 nm), a greater fraction of molten liquid during SHS was achieved. With the addition of nanocrystalline reaction agent, the contact angle (wettability) between the solid and liquid in the reactant increases with greater formation of molten liquid. This will then bring forth greater capillary forces to attract the particles in the reactant together [1]. Hence, this transforms most of the elongated channels into smaller pores. As the amount of nanocrystalline reaction agent increases to 50 wt.% (i.e. $NiTi_{MA50\%}$), the reactant mixture absorbs the superfluous energy from the reaction agent and results in an even larger fraction of liquid phase. This liquid phase rapidly wets and spreads throughout the reaction front via capillary mode. The voids are then filled by

spreading the liquid to produce a dense NiTi which consists of dendritic forms after solidification. In this experiment, by using $NiTi_{MA50\%}$ which contained greater energy, the SHS process can be initiated at a much lower temperatures (i.e. 25 °C instead of > 200 °C). This has shown that the activation barriers for combustion synthesis reaction can be effectively lowered by the addition of nanocrystalline reaction agent.

8.2 The proposed explanation on phase formation of NiTi binary alloy system.

The NiTi phase consists of equiatomic composition of 49 atom.% Ni and 51 atom.% Ti as shown in Figure 8.3. The stoichiometry composition has a strong influence on the properties of NiTi (i.e. shape memory effect and superelasticity) where a deviation in the Ni content of 1 at. % can bring forward the martensite-start temperature (M_s) by 100 K [19]. Therefore, it is important to only obtain single phased NiTi for porous NiTi. However, the narrow stoichiometric range in Ni-Ti binary alloy phase diagram has made this harder to achieve in practice.

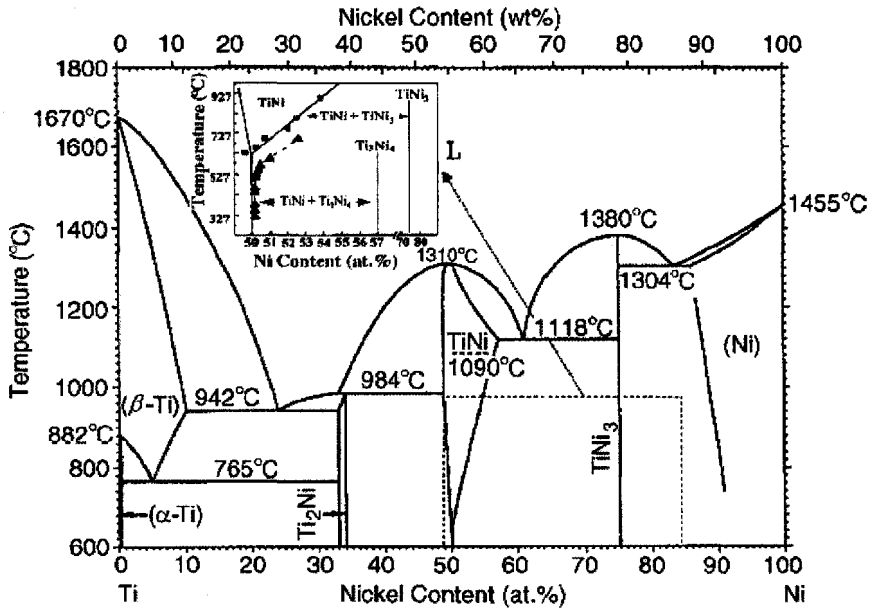

Figure 8.3 The Ni-Ti binary alloy phase diagram [19]

An examination of the Ni-Ti binary alloy diagram shows two neighbouring stable intermetallic phases of Ti_2Ni and Ni_3Ti. The Gibbs free energies of NiTi, Ti_2Ni and Ni_3Ti indicate that the driving force for the formation of Ti_2Ni and Ni_3Ti are stronger than that of NiTi as shown in Figure 8.4. [52]. Therefore, once the formation of NiTi occurs, it is unlikely that these secondary phases of Ti_2Ni and Ni_3Ti will entirely disappear. This explains the presence of the secondary phases of Ti_2Ni and Ni_3Ti in the as-SHS final product. Unreacted Ni was found in porous $NiTi_{100\%}$ probably because the rates of self- and inter-diffusion are not proficient enough between the Ni and Ti owing possibly to the low combustion temperature obtained from the elemental reactant.

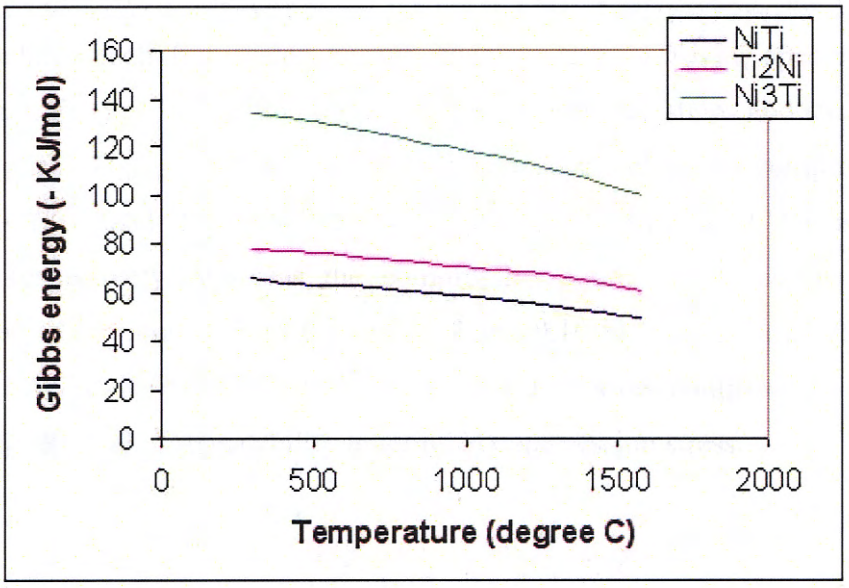

Figure 8.4 The Gibbs free energy of formation for possible NiTi, Ti_2Ni and Ni_3Ti phases at relevant temperatures.

On the other hand, MA is known for its ability to store high enthalpy in the MA powder in the form of lattice and point defects which cannot be achieved by other traditional processing techniques for nanocrystalline material [61]. The mechanically alloyed Ni-Ti powder at 75 h milling had obtained a crystallite size of 10 nm with large lattice strain of 0.85%. Thus, the hypothetical explanation of using MA Ni-Ti powder at 75h as a nanocrystalline reaction agent is that grain refinement in the MA powder will increase the grain boundary area, which leads to a disordered structure with increased grain boundaries. Hence, new additional total energy can be introduced into the material as an atomic disorder and/or grain boundaries during milling [13]. This total energy can be estimated using equation (8.1). Consequently, the use of nanocrystalline reaction agents will effectively lower the activation barriers for combustion

synthesis reaction. The nanocrystalline reaction agent will then modify the phase transformation kinetics induced by the final SHS process. This structural relaxation will then lead to the formation of NiTi phase at a lower temperature (i.e. NiTi formed at ambient temperature with the addition of nanocrystalline Ni-Ti). Hence, the addition of 50 wt.% nanocrystalline Ni-Ti reaction agent in SHS process results in the increase of NiTi major phase by approximately 30%, the reduction of the by-product phase and the elimination of the unreacted Ni (as compared to $NiTi_{100\%}$).

$$\Delta G(milling) = \Delta G(disorder) + \Delta G(grain\ boundaries) \tag{8.1}$$

CHAPTER 9 EVALUATING THE MECHANICAL PROPERTY OF THE POROUS $NITI_{100\%}$ AND NITI $_{MA25\%}$

This chapter reports the mechanical properties of SHS-synthesized porous $NiTi_{100\%}$ and $NiTi_{MA25\%}$ before undergoing thermal treatment. Thus, this study evaluates the strength characteristics of the synthesized porous NiTi such as ultimate compressive strength and Young's Modulus.

9.1 The stress-strain curve of synthesized porous $NiTi_{100\%}$ and $NiTi_{MA25\%}$ specimens

Table 9.1 tabulates each five tested porous $NiTi_{100\%}$ and $NiTi_{MA25\%}$ specimens from the compression test. Figures 9.1 (a) and (b) show the compressive stress and strain of the each five tested porous $NiTi_{100\%}$ and $NiTi_{MA25\%}$ specimens respectively. The compressive stress of the porous $NiTi_{100\%}$ and $NiTi_{MA25\%}$ tested ranged from 63.80 to 37.97 and 171.92 to 132.98 MPa, respectively. Whereas the compressive strain of the porous $NiTi_{100\%}$ and $NiTi_{MA25\%}$ tested to be ranging from 0.21 to 0.07 and 0.10 to 0.06 mm/mm respectively. It was noted that $NiTi_{MA25\%}$ produced more uniformed pore sizes compared to $NiTi_{100\%}$. This resulted in a higher level of repeatability in terms of compression stress.

Table 9.1 The compression test results from each five tested porous $NiTi_{100\%}$ and $NiTi_{MA25\%}$ specimens.

Specimen name	**Porous $NiTi_{100\%}$**		**Porous $NiTi_{MA25\%}$**	
	Compressive strain at Max compression load (mm/mm)	Compressive stress at Max compression load (MPa)	Compressive strain at Max compression load (mm/mm)	Compressive stress at Max compression load (MPa)
1	0.17	45.48	0.09	132.98
2	0.21	37.97	0.09	169.25
3	0.07	63.80	0.10	171.92
4	0.09	45.55	0.08	163.47
5	0.18	48.47	0.06	137.11
Mean	0.14	48.26	0.08	154.95

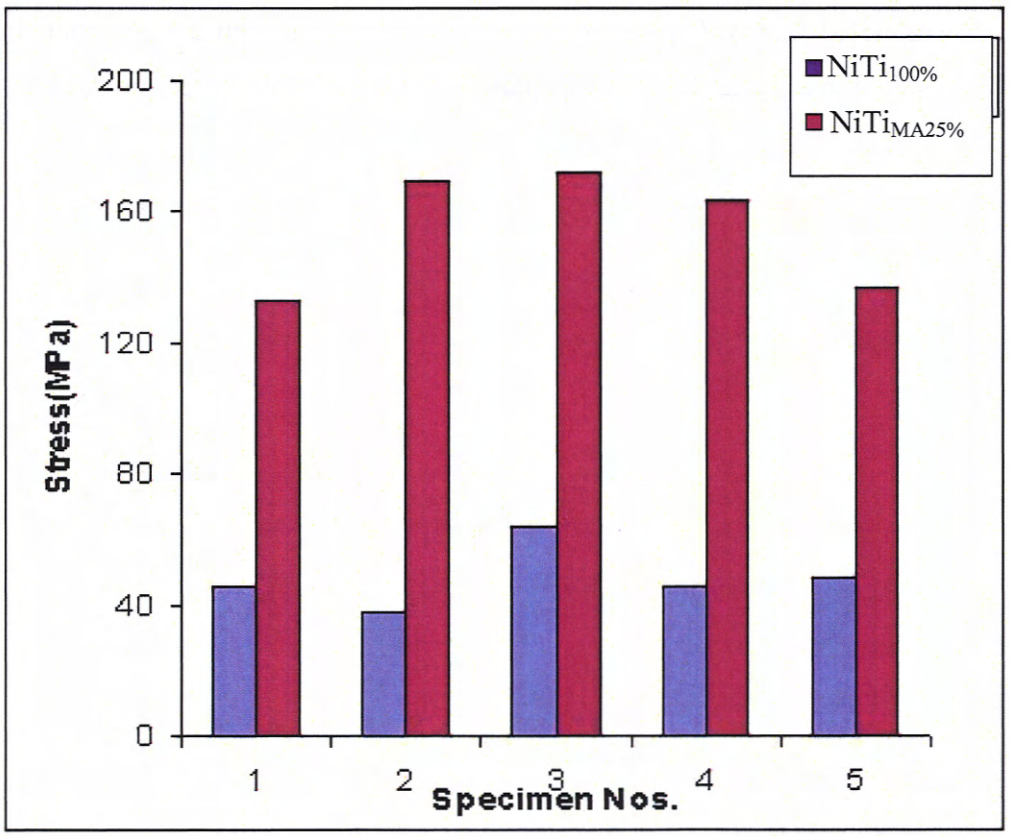

(a)

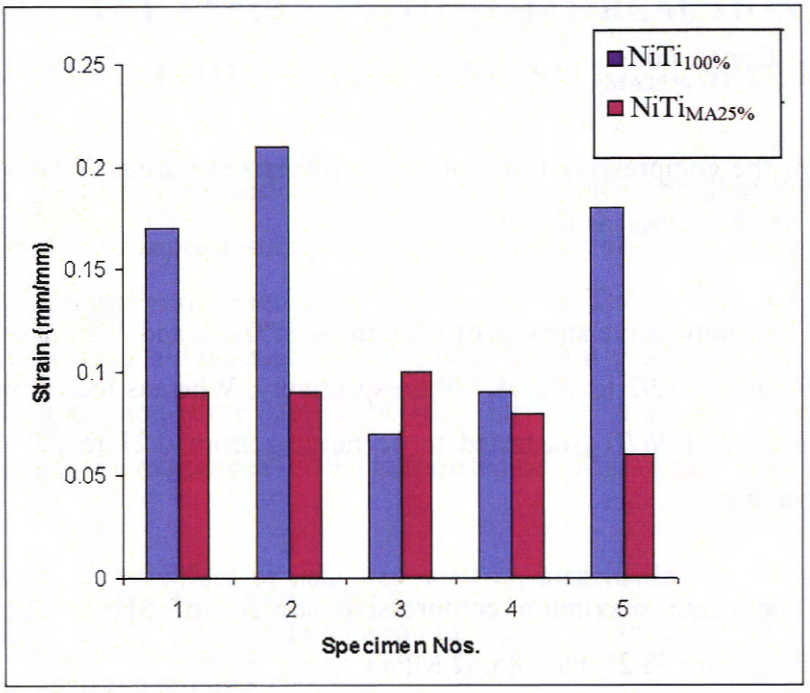

(b)

Figure 9.1 The compressive (a) stress and (b) strain of porous $NiTi_{100\%}$ and $NiTi_{MA25\%}$ specimens.

The compressive stress–strain mean curve of the SHS-synthesized porous $NiTi_{100\%}$ and $NiTi_{MA25\%}$ specimens is shown in Figure 9.2. The mean maximum compressive stress of SHS-synthesized porous $NiTi_{100\%}$ and $NiTi_{MA25\%}$ are 48.26 and 148.32 MPa respectively. The mean Young's modulus of porous $NiTi_{100\%}$ and $NiTi_{MA25\%}$ are 0.402 and 1.854 GPa, respectively.

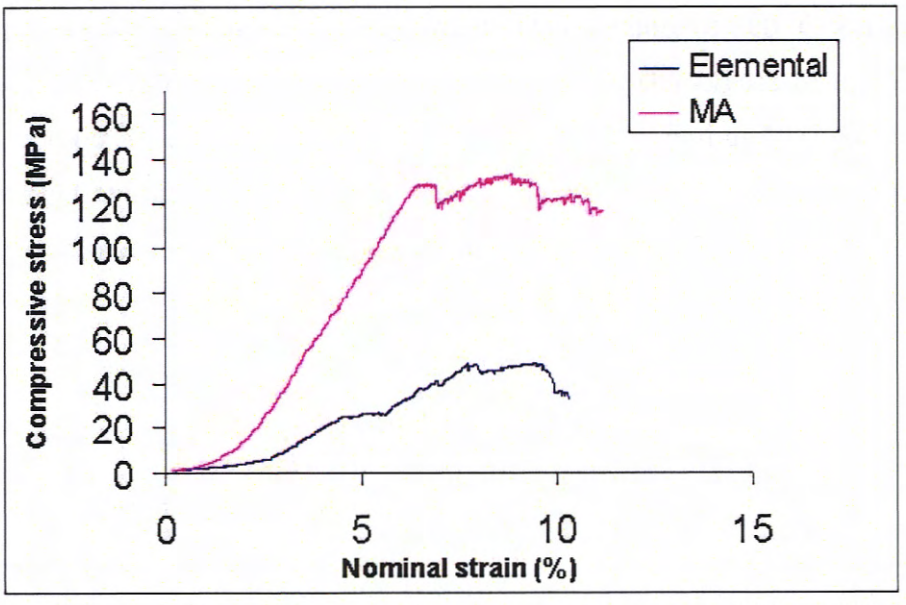

Figure 9.2 Mean stress–strain curve of porous $NiTi_{100\%}$(Elemental) and $NiTi_{MA25\%}$ (MA) in compression.

9.2 Conclusions

From the compressive tests for SHS-synthesized porous $NiTi_{100\%}$ and $NiTi_{MA25\%}$, the results can be summaried as follows:

1) The compressive stresses of the porous $NiTi_{100\%}$ and $NiTi_{MA25\%}$ tested ranged from 63.80 to 37.97 and 171.92 to 132.98 MPa respectively. Whereas the compressive strain of the porous $NiTi_{100\%}$ and $NiTi_{MA25\%}$ tested to be ranging from 0.21 to 0.07 and 0.10 to 0.06 mm/mm, respectively.

2) The mean maximum compressive stresses of SHS-synthesized porous $NiTi_{100\%}$ and $NiTi_{MA25\%}$ are 48.26 and 148.32 MPa respectively.

3) The mean Young's modulus of SHS-synthesized porous $NiTi_{100\%}$ and $NiTi_{MA25\%}$ are 0.402 and 1.854 GPa, respectively.

CHAPTER 10 THE EFFECT OF THERMAL REACTION TREATMENT ON POROUS $NITI_{100\%}$ AND $NITI_{MA25\%}$ SPECIMENS

The essential factors that affect performance of the shape memory alloy (SMA) with shape memory effect (SME) or superelasticity (SE) included transition temperatures, nature of the martensite phase, R-phase and austenite phase [28, 65, 66]. These issues are important when porous NiTi is used as a biomaterial. In the heat treatment process, the cooling rate, heat treatment temperature and time determine the forward and reverse phase transition temperatures between the martensite (B19') and austenitic phases (B2') [65].

This study focuses on the effect of heat treatment on austensitic phase transition (reverse martensitic transformation) and to manipulation of the phase transition transformation of the porous NiTi through heat treatment.

10.1 Solid solution treatment on porous $NiTi_{100\%}$

Figure 10.1 shows the phase constituents of SHS-synthesized porous $NiTi_{100\%}$ before (0) and after undergoing solid solution treatment at 800 and 1000 °C (800 and 1000 respectively). As shown in Figure 10.2, the B2(NiTi) and B19'(NiTi) as predominant phases of SHS-synthesized porous $NiTi_{100\%}$ treated at solid solution temperature of 800 °C were significantly increased by 10% but unreacted Ni was still present. Further increase of the solid solution temperature to 1000 °C, eliminated Ni in the SHS-synthesized porous $NiTi_{100\%}$. However, the solution treatment had little effects on the amount Ti_2Ni. This has shown the possibility to perform homogenisation through solution treatment for the reduction of free-nickel residues.

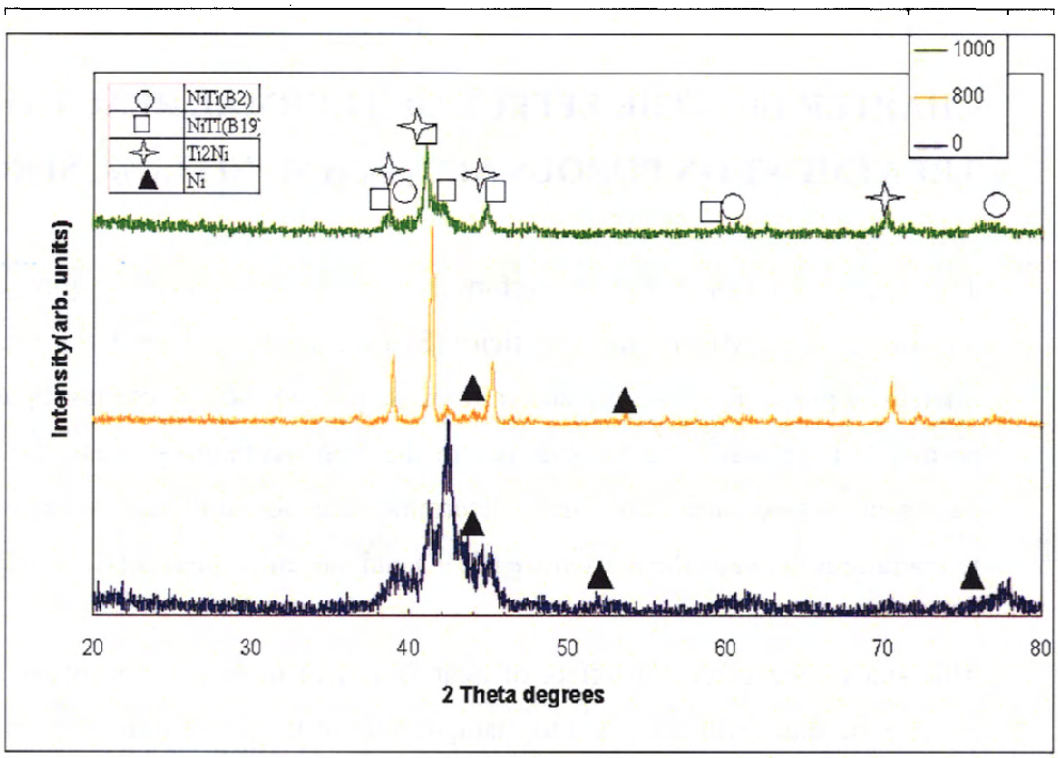

Figure 10.1. XRD spectra of porous $NiTi_{100\%}$ on solid solution temperatures at 800, 1000 °C and non-solid solution treatment (i.e. 0).

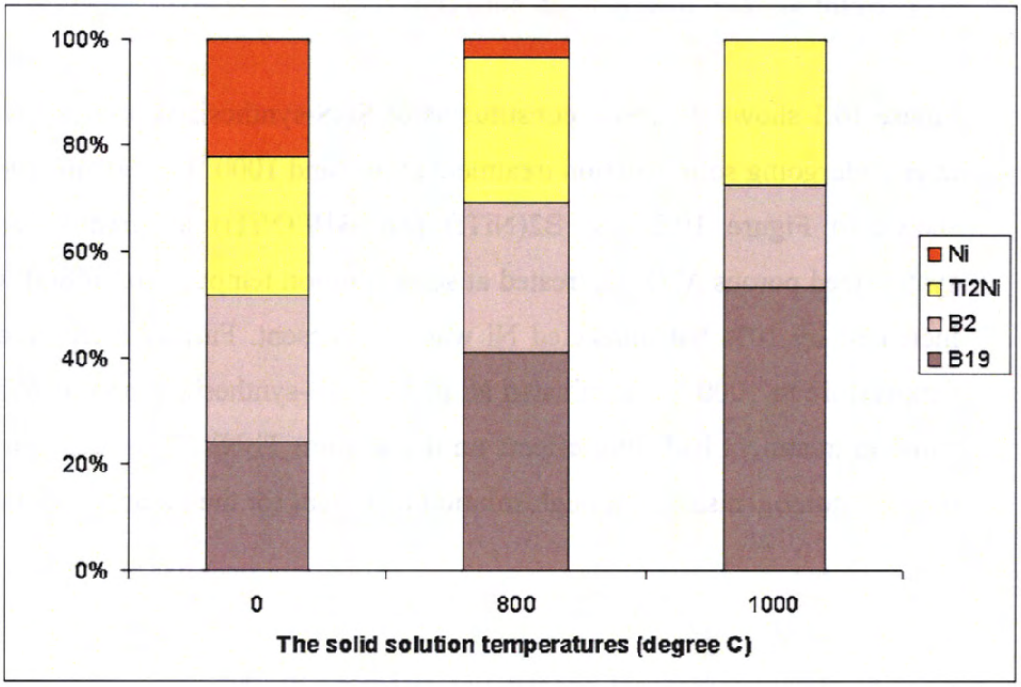

Figure 10.2. The chemical composition ratios from XRD of porous $NiTi_{100\%}$ on solid solution temperatures at 800, 1000 °C (800 and 1000) and non-solid solution treatment (0).

10.2 Solid solution treatment on porous $NiTi_{MA25\%}$

Figure 10.3 shows the phase constituents of SHS-synthesized porous $NiTi_{MA25\%}$ before (0) and after undergoing the solid solution treatment of 800 and 1000 °C (800 and 1000 respectively). At solid solution temperature of 800°C, Ni_3Ti and Ti_2Ni were observed as shown in Figure 10.4. The further increase of the solid solution temperature to 1000°C has increased the B2(NiTi) and B19'(NiTi) as predominant phases by almost 20% as compared to untreated SHS-synthesized porous $NiTi_{MA25\%}$. In addition, only Ti_2Ni as the secondary phase was found. Another observation in this solid solution treatment studies is that the SHS-synthesized porous $NiTi_{MA25\%}$ with nanocrystalline reaction agent additive has increased 10% more of the predominant phases (i.e. B2(NiTi) and B19'(NiTi)) as compared to without nanocrystalline reaction agent additive (i.e $NiTi_{100\%}$) at solid solution temperature of 1000 °C.

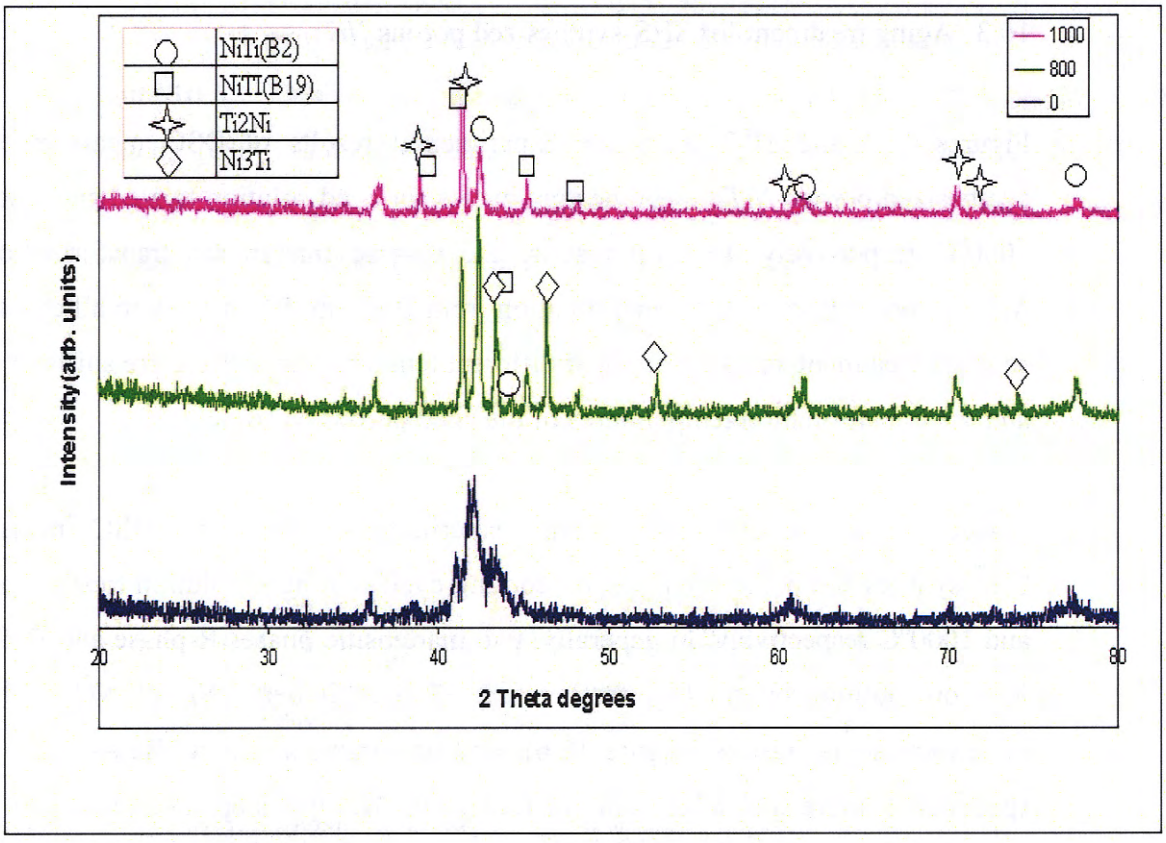

Figure 10.3. XRD spectra of porous $NiTi_{MA25\%}$ on solid solution temperatures at 800, 1000 °C (800 and 1000) and non solid solution treatment (0).

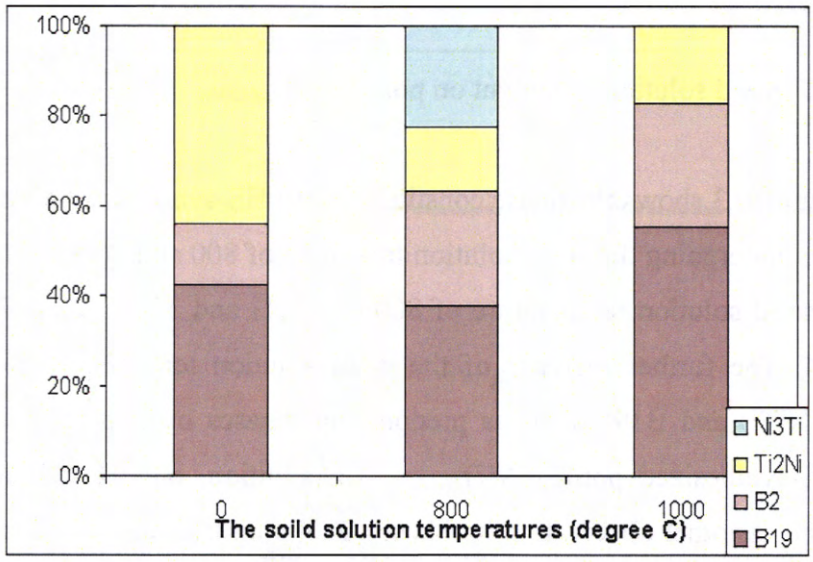

Figure 10.4. The chemical composition ratios from XRD of porous $NiTi_{MA25\%}$ on solid solution temperatures at 800,1000 °C (i.e. 800 and 1000) and non solid solution treatment (0) from XRD results.

10.3 Aging treatment for SHS-synthesized porous $NiTi_{100\%}$

Figures 10.5 and 10.7 show the experimental results of DSC measurements for SHS-synthesized porous $NiTi_{100\%}$ on heating cycles for aged solution treated specimens at 800 and 1000°C respectively. In both results, the reverse martensitic transformations in porous $NiTi_{100\%}$ occur in one-step transformation from B19'into B2 directly in all cases (before, after solution treatment and after aging at different temperatures). There are shifts in peak positions and the transformation temperatures of the aged porous $NiTi_{100\%}$.

Figures 10.6 and 10.8 show the experimental results of DSC measurements for SHS-synthesized porous $NiTi_{100\%}$ on cooling cycles for aged solution treated specimen at 800 and 1000°C respectively. In generally, two martensitic phases R-phase and B19' are prone to form on cooling from the high temperature B2 phase in dense Ni-rich NiTi SMAs [28]. From the experimental results (Figure 10.6), one-step transformation (B2↔B19') was observed specimens before and after solution treatment. Multiple-step transformation was observed specimen after aging at 400 and 450 °C. With the increase aging temperature from 500 to 550 °C, the two-step transformation (B2↔R-phase and R-phase↔B19') was observed. The range of the overall transformation temperature changes from small (i.e. after solution treatment) through large (i.e. after aged treatment at 400 to 550°C). As for solution

temperature at 1000°C, one-step transformation (B2↔B19') was observed in all aged porous $NiTi_{100\%}$ (Figure 10.8).

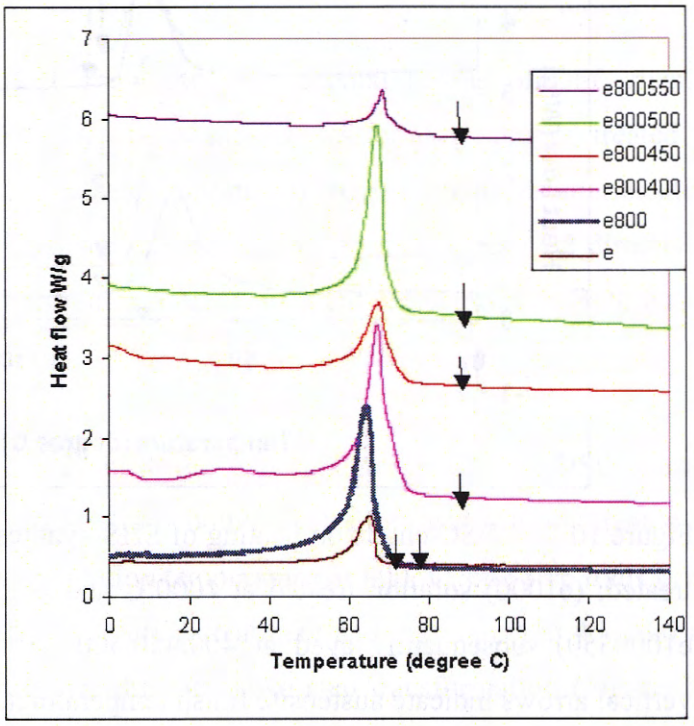

Figure 10.5. DSC charts on heating of SHS-synthesized porous $NiTi_{100\%}$ at (e) non-treated; (e800) solution treated at 800°C and (e800400, e800450, e800500 & e800550) subsequently aged at 400,450,500 and 550°C respectively. The small vertical arrows indicate the austensite finish temperature(A_f).

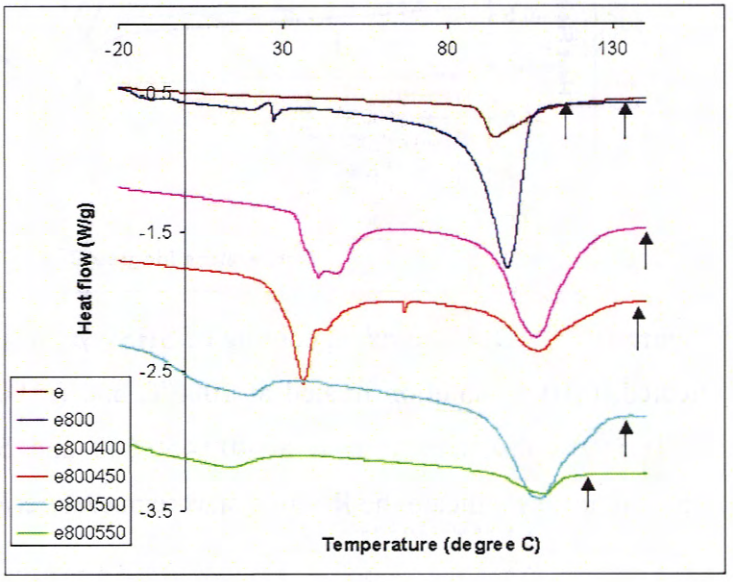

Figure 10.6. DSC charts on cooling of SHS-synthesized porous $NiTi_{100\%}$ at (e) non-treated; (e800) solution treated at 800°C and (e800400, e800450, e800500 & e800550) subsequently aged at 400,450,500 and 550°C respectively. The small vertical arrows indicate the R-phase start temperature(R_s).

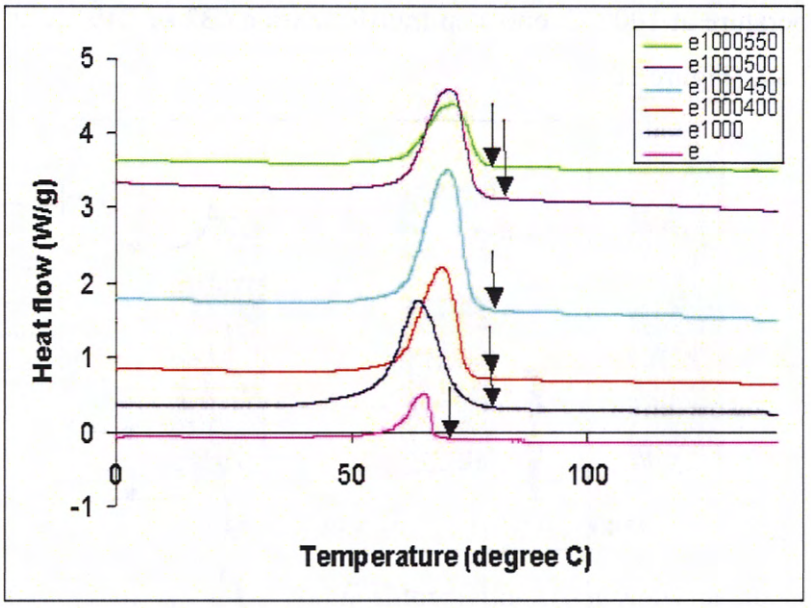

Figure 10.7. DSC charts on heating of SHS-synthesized porous $NiTi_{100\%}$ at (e) non-treated; (e1000) solution treated at 1000°C and (e1000400, e1000450, e1000500 & e1000550) subsequently aged at 400,450,500 and 550°C respectively. The small vertical arrows indicate austensite finish temperature(A_f).

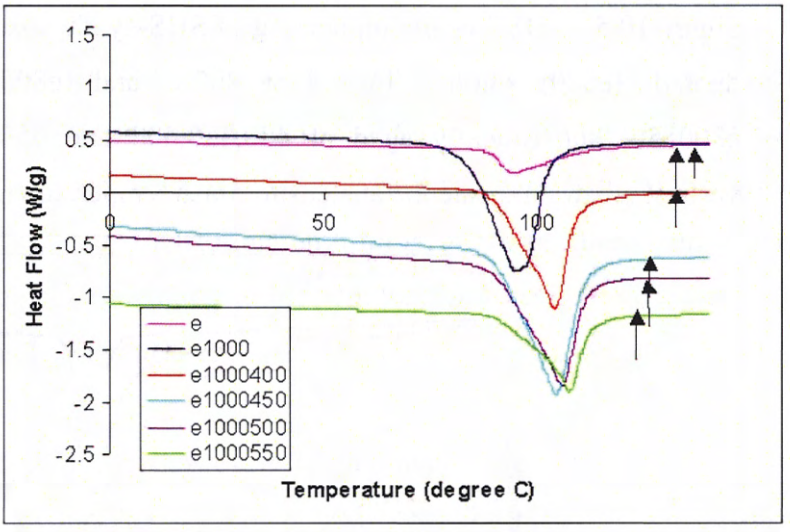

Figure 10.8. DSC charts on cooling of SHS-synthesized porous $NiTi_{100\%}$ at (e) non-treated; (e1000) solution treated at 1000°C and (e1000400, e1000450, e1000500 & e1000550) subsequently aged at 400,450,500 and 550°C respectively. The small vertical arrows indicate the R-phase start temperature(R_s).

10.4 Aging treatment for SHS-synthesized porous $NiTi_{MA25\%}$

Figures 10.9 and 10.11 show the experimental results of DSC measurements for SHS-synthesized porous $NiTi_{MA25\%}$ on heating cycles for aged solution treated specimen at 800 and 1000°C respectively. The aged porous $NiTi_{MA100\%}$, reverses martensite transformations in porous $NiTi_{MA25\%}$ in one-step transformation from B19' into B2 directly in all cases (before, after solution treated and after aged at different temperatures). Both austenite finish (A_f) and peak temperature positions of the aged porous $NiTi_{MA25\%}$ are shifted.

Figures 10.10 and 10.12 show the experimental results of DSC measurements for SHS-synthesized porous $NiTi_{MA25\%}$ on cooling cycles for aged solution treated specimen at 800 and 1000°C respectively. In solution temperature of 800 °C, one-step transformation was observed in specimens before, after solution treatment and after aging at 450,500 and 550°C. Only the sample aging at 400 °C resulted in a two-step transformation (Figure 10.10). Similarity, in solution temperature of 1000 °C, it has similar phase transformation behavior as solution treated specimens at 800 °C for porous $NiTi_{MA25\%}$ (Figure 10.12).

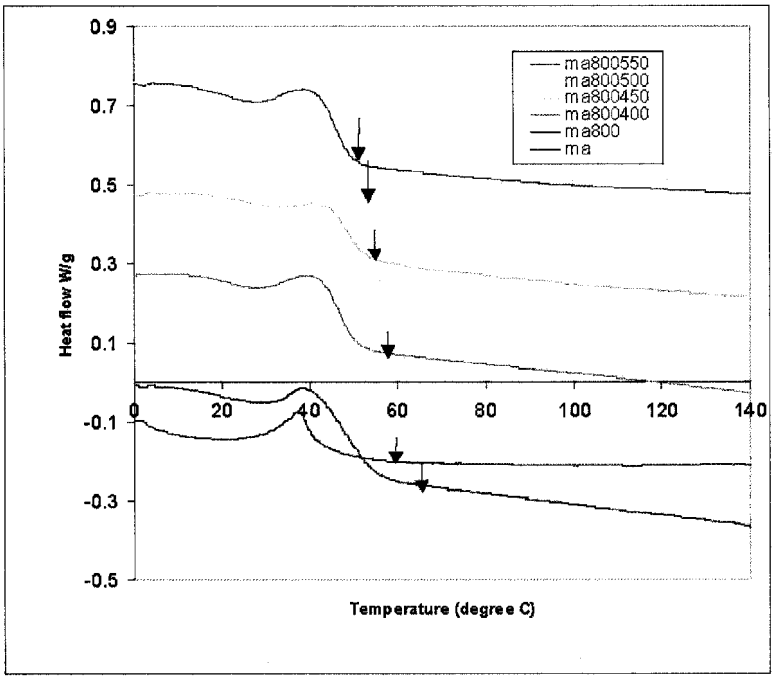

Figure 10.9. DSC charts on heating of SHS-synthesized porous $NiTi_{MA25\%}$ at (e) non-treated; (ma800) solution treated at 800°C and (ma800400, ma800450, ma800500 & ma800550) subsequently aged at 400,450,500 and 550°C respectively. The small vertical arrows indicate the austensite finish temperature (A_f).

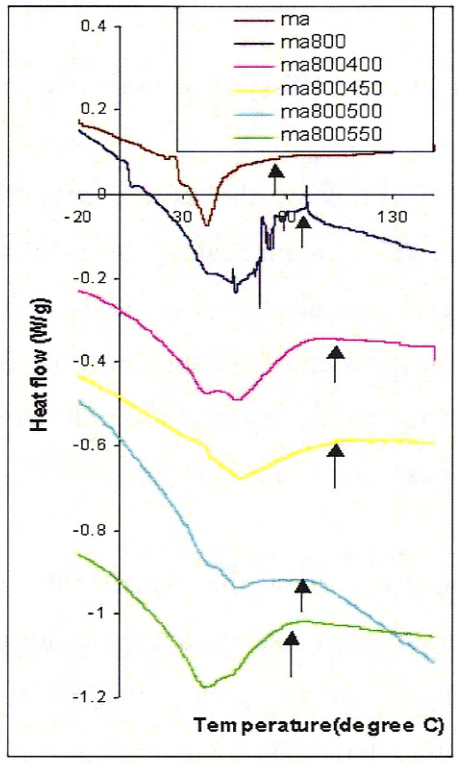

Figure 10.10. DSC charts on cooling of SHS-synthesized porous $NiTi_{MA25\%}$ at (e) non-treated; (ma800) solution treated at 800°C and (ma800400, ma800450, ma800500 & ma800550) subsequently aged at 400,450,500 and 550°C respectively. The small vertical arrows indicate the R-phase start temperature(R_s).

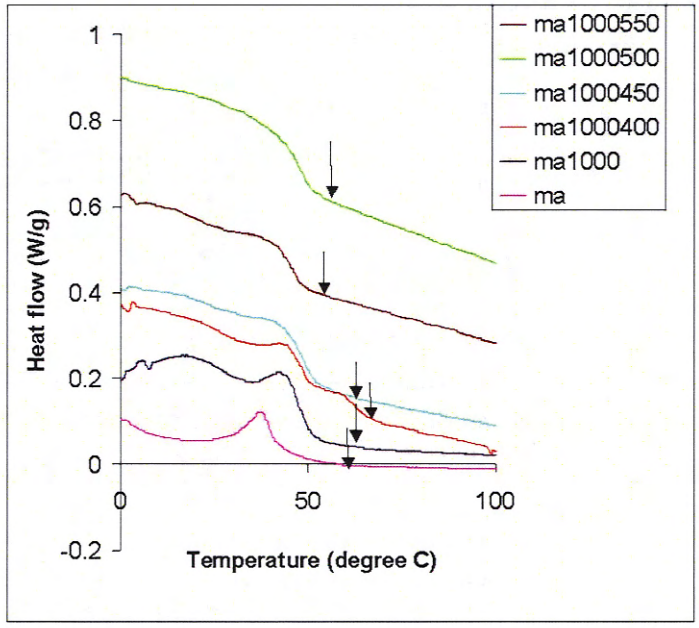

Figure 10.11. DSC charts on heating of SHS-synthesized porous $NiTi_{MA25\%}$ at (e) non-treated; (ma1000) solution treated at 1000°C and (ma1000400, ma1000450, ma1000500 & ma1000550) subsequently aged at 400,450,500 and 550°C respectively. The small vertical arrows indicate austensite finish temperature(A_f).

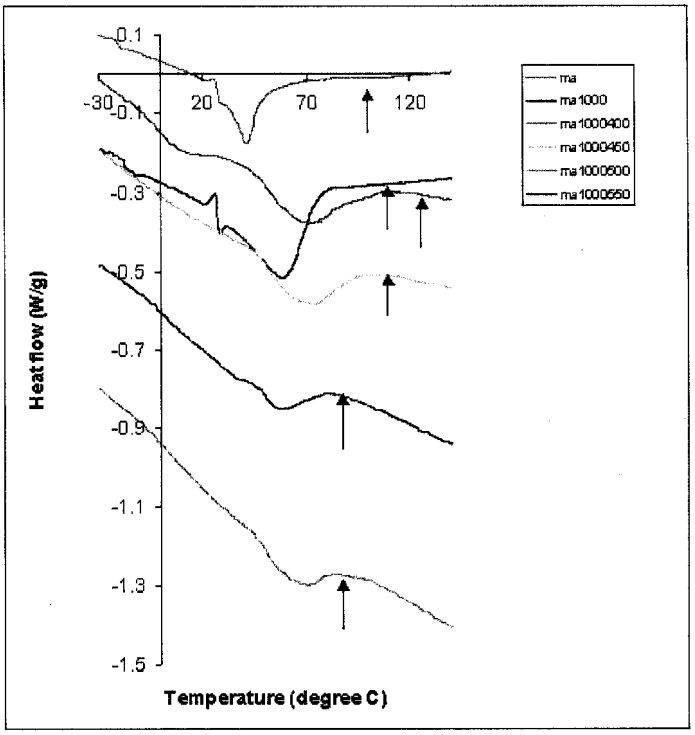

Figure 10.12. DSC charts on cooling of SHS-synthesized porous $NiTi_{MA25\%}$ at (e) non-treated; (ma1000) solution treated at 1000°C and (ma1000400, ma1000450, ma1000500 & ma1000550) subsequently aged at 400,450,500 and 550°C respectively. The small vertical arrows indicate the R-phase start temperature(R_s).

10.5 Correlation between the transition and aging temperatures

After aging treatment on SHS-synthesized porous $NiTi_{100\%}$ and $NiTi_{MA25\%}$, results were collected from the DSC charts (Figures 10.5, 10.6, 10.7 and 10.8) and plotted against austenite finish temperature (A_f) and R-phase start temperature (R_s) against temperatures as shown in Figure 10.13 and 9.14 respectively. Figure 10.13 displays the effects of aging temperature (400-550°C) on A_f temperature. Both SHS-synthesized porous $NiTi_{100\%}$ had received 800 and 1000 °C solid solution treatment (e800 and e1000 respectively) and similarly the porous $NiTi_{MA25\%}$ received 800 and 1000 °C solid solution treatment (ma800 and ma1000 respectively). NA in the graph represents SHS-synthesized porous $NiTi_{100\%}$ (e) and $NiTi_{MA25\%}$ (ma) before undergoing any heat treatment. Generally in all cases, with an increase aging temperature, a decrease A_f in both specimens of porous $NiTi_{100\%}$ and $NiTi_{MA25\%}$. Specimens were observed. Referring to the effects of after-aging temperature on R-phase start temperatures (*Rs*), similar increase in aging temperature and decrease in *Rs* on both porous $NiTi_{100\%}$ and $NiTi_{MA25\%}$ (Figure 10.14) were observed.

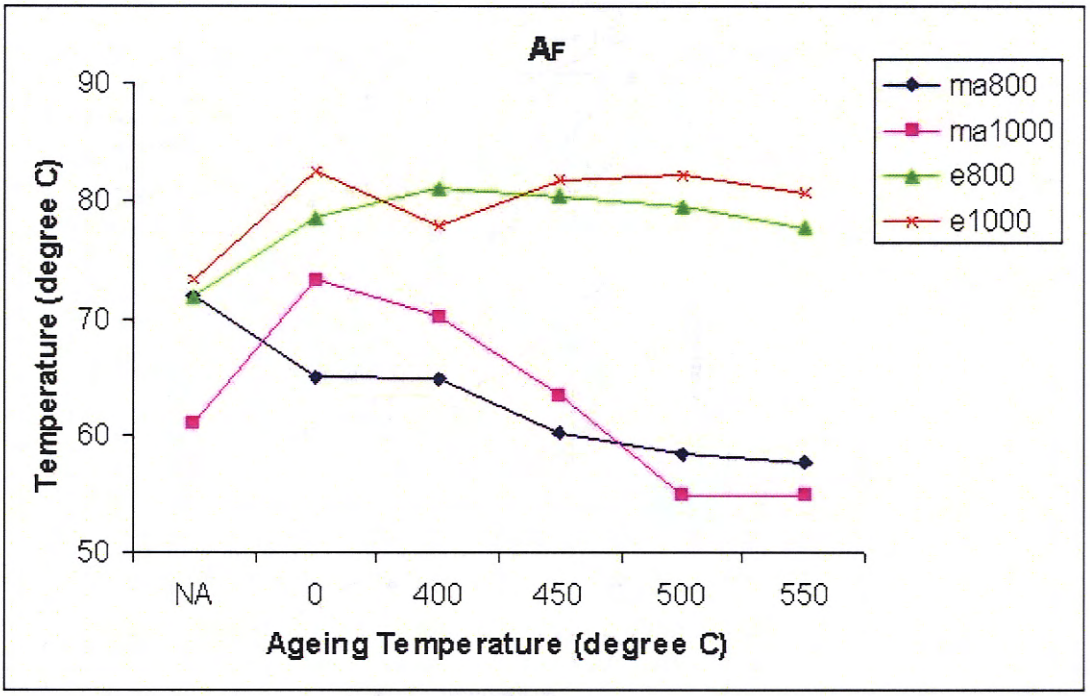

Figure 10.13. The effects of after-aging temperature (400-550°C) on A_f temperature for SHS-synthesized porous $NiTi_{100\%}$ which had received solution treatment temperatures of 800 and 1000°C.

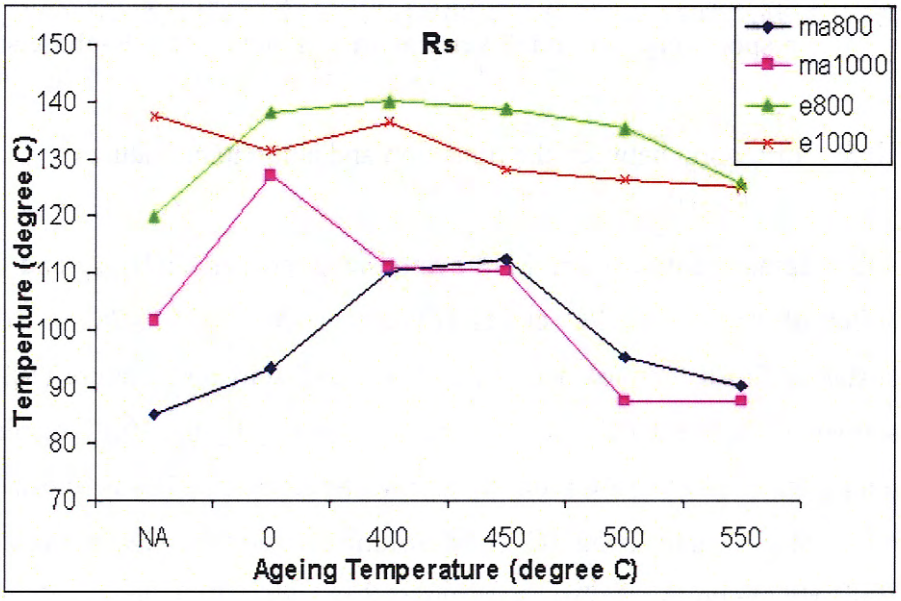

Figure 10.14. The effects of after aging-temperature (400-550°C) on *Rs* temperature for SHS-synthesized porous $NiTi_{100\%}$ which had received solution treatment temperatures of 800 and 1000°C.

10.6 Conclusions

There are different alterative methods to change the austenitic phase transition temperature. Such methods include alloying, adding ternary element and thermal-mechanical treatment [65, 67]. The rationality of employing heat treatment parameters over other alterative methods is that the using of ternary element may introduce undesirable phases into the material that causes risk of bio-incompatibility for medical purposes. As for thermal-mechanical treatments such as cold and hot working, these are not suitable for medical implants if the final shape must be fixed in the factory. Heat treatment is convenient and simple for use to manipulate the transition temperature of the porous NiTi alloy. Therefore, from the thermal treatment of porous $NiTi_{100\%}$ and $NiTi_{MA25\%}$ studies, the results can be summarized as follows:

1) In the solid solution treatment studies, the solution treated SHS-synthesized porous $NiTi_{100\%}$ and $NiTi_{MA25\%}$ has increased its predominant phase (B2 and B19') as solution temperature increased from 800 to 1000 °C. Figures 10.2 and 10.4 show solution treatment at 1000 °C for SHS-synthesized porous $NiTi_{100\%}$ and $NiTi_{MA25\%}$ which has increased by around 17% and 27% of the predominant phase, respectively compared to non-solution treated specimens. This has shown the possibility to perform homogenisation through solution treatment to reduce the nickel residues in the SHS-synthesized porous $NiTi_{100\%}$.

2) The phase transition temperatures (A_f and R_s) of SHS-synthesized porous $NiTi_{100\%}$ and $NiTi_{MA25\%}$ have decreased as the after-aging temperatures increased. In solution treatment at 1000 °C with subsequently aging of porous $NiTi_{100\%}$ at 550°C, this obtained a high A_f temperature at around 76 °C was obtained. With similar heat treatment, the porous $NiTi_{MA25\%}$ (with additive of nanocrystalline reaction agent) has A_f temperature at around 53 °C, which has shown higher possibility of achieving at a human body temperature for biomaterial purposes.

CHAPTER 11 CONCLUSIONS

The elemental Ni-Ti reactant powder by tumbler mixing and nanocrystalline Ni-Ti reactant powders by mechanical alloying were employed for SHS process in this research. The nanocrystalline Ni-Ti powder used had a crystallite size of 10 nm and lattice strain of 0.85% at 75h of milling time. In addition, the elemental Ni-Ti powder prepared by tumbler mixer has achieved a homogenous mixture of reactant powder.

The SHS system was successfully established. System parameters (i.e. P_s and d_e) were optimised by which near-net shape parts could be produced. Characteristics of the compacted reactant were analysed during the compaction stage. The results obtained a maximum variation of green porosity ε_g of ± 2.5 vol.% and a height-to-diameter ratio (H/D) of 1.9 in compacted reactant. However the deviation of ε_g and maximum setting H/D ratio of 1.9 did not have significant effect on the final morphology and distribution pores in porous $NiTi_{100\%}$.

The final porous $NiTi_{100\%}$ obtained arrays of cavity-like circular conduits (i.e. banded structure of channels) distributed along the perpendicular direction to the propagation direction. These banded structure of channels ranged between 1 and 4.5 mm at compression forces of 8, 16 and 24 KN and under preheating temperatures of 200 and 300 °C. The porous $NiTi_{100\%}$ has an average general porosity ranging from 43 and 58 vol.%. Phase analysis revealed that the NiTi (B2') and NiTi (B19') were the dominant phases in the final porous $NiTi_{100\%}$ product. In addition, the secondary phases such as Ti_2Ni and unreacted Ni were detected in all cases.

The pore morphology of most porous $NiTi_{MA25\%}$ obtained shape like ramification forming of dendritical pore structure surrounded with numerous smaller near-circular or elliptic pores. The average pore size ranged from 100 to 600 μm with general porosity ranging between 52 and 58 vol.%. In the phase analysis, formation of dominant phases (NiTi (B2') and NiTi (B19')) and secondary phase (Ti_2Ni) were noticed in the final porous $NiTi_{MA25\%}$. The metastable phases of Ni_3Ti and unreacted Ni product were only observed in the final porous $NiTi_{MA25\%}$ at compression forces of 8 and 16 kN under preheating temperature of 200 °C. However, at a higher initial compacted reactant density by higher compression force and preheating temperature with addition of 25% nanocrystalline reaction agent, unreacted Ni was

eliminated. In addition, there was an increased dominant phase of NiTi formation by 13% as compared to without using reaction agent.

The increased nanocrystalline reaction agent to 50% produced dense parts in the final $NiTi_{MA50\%}$. The dominant phases; NiTi (B2) and NiTi (B19) and secondary phases; Ti_2Ni, Ni_3Ti were observed in the final $NiTi_{MA50\%}$ product. In addition, no undesirable unreacted Ni was found in the $NiTi_{MA50\%}$ final product in all results.

Based on the present study, it has been established that not only the morphology and the product composition are affected by the green porosity and preheating temperature, but also the addition of the reaction agent. Hence, a proposed mechanism for the additive reaction agent influence on the morphology and phase formation in the SHS product was investigated and proposed.

The use of nanocrystalline Ni-Ti powder as reaction agent confirmed the advantage of introducing new additional total energy into the material the form of lattice and point defects. This has effectively lowered the activation barriers for combustion synthesis reaction which helps advance the reaction and "energized" chemical evolution. It has modified the phase transformation kinetics induced by the final SHS process.

The mean maximum compressive stress of as-SHS porous $NiTi_{100\%}$ and $NiTi_{MA25\%}$ were 48.26 and 148.32 MPa respectively. This has revealed the influence of additive nanocrystalline NiTi in porous $NiTi_{100\%}$ increased almost 300% of its maximum compressive stress.

In the solid solution treatment studies, the predominant phases (B2 and B19') of solution treated as-SHS porous $NiTi_{100\%}$ and $NiTi_{MA25\%}$ increased by almost 17% and 27% respectively as compared to the parts before solution treatment. It has shown the possibility to reduce the free-nickel residues in the as-SHS porous $NiTi_{100\%}$ through solution treatment during homogenisation. The phase transition temperatures (A_f and R_s) of as-SHS porous $NiTi_{100\%}$ and $NiTi_{MA25\%}$ decreased as the aging temperature was increased. Solution treatment at 1000 °C and the subsequently aging of porous $NiTi_{100\%}$ at 550°C, a high A_f temperature at around 76 °C was obtained. With same heat treatment, the treated porous $NiTi_{MA25\%}$ (with additive of nanocrystalline reaction agent) has A_f temperature around 53 °C.

The use of nanocrystalline NiTi reaction agent has shown great potential to reduce unwanted secondary intermetallic phases, eliminate unreacted Ni, lower the austensite transition temperature and increase the compressive strength in the final SHS product. It also has the possibility to manipulate suitable pore size morphology in the final porous NiTi part.

11.1 Recommedation

From the results, using additive nanocrystalline reaction agent has produced a homogenous part with suitably ranged of pore sizes to favour bio-applications. The biocompatibility of such porous NiTi implants can be studied both in vitro and in vivo. Studies of various techniques of coating such as plasma-spraying and dip-coating methods [68] for porous NiTi may also be carried out. This is because the nickel–titanium alloys contain nickel, which remains a reservation for the long-term performance of implants. To extend the potential for porous nickel–titanium shape-memory alloys (NiTi-SMA), coating the part with calcium phosphate may further improve the biocompatibility in bone contact. On the other hand, because human body fluid is a complex system, porous NiTi maybe studied on corrosion problem aspects. This will involve using simulated body fluid (SBF) such as physiological solution, Ringer's solution or Hank's solution which is commonly used to simulate human body fluid when corrosion tests are performed. The study on the effects of porosity on the osteointegration of NiTi implants in the animal may benefit to this research.

As in Chapter 2.2, porous NiTi can be used potentially as dampers and shock by utilizing the energy absorption. Vibration analysis [69] can be done to evaluate the Young's modulus and the loss factor of materials. A long cylinder porous material is forced into vibration and such longitudinal, transverse or torsional excitations can be created. The sample can be clamped at one or two ends, or be supported by or suspended from thin wires. Then the sample can be excited by magnetic fields and the resulting vibrations can be picked up by an impedance coil. Using clamps, one introduces friction between clamps and samples, whereas supporting a foam bar on thin wires creates problems because the location of the vibrational nodes of the inhomogeneous sample is unknown. Thus to avoid clamping, the porous material can be fix the directly to an electromagnetic shaker. The amplitude of vibrations as a function of excitation frequency shows characteristic resonance peaks. The positions of the peaks ν_p allow one to calculate Young's modulus E from the sample dimensions and mass using standard formulae. The widths $\Delta\nu/\nu_p$ of the resonance peaks define the loss factor η.

REFERENCES

[1] J. J. Moore and H. J. Feng, "Combustion synthesis of advanced materials: Part I. Reaction parameters," *Progress in Materials Science*, vol. 39, pp. 243-273, 1995.

[2] C. Y. Chung, C. L. Chu, and S. D. Wang, "Porous TiNi shape memory alloy with high strength fabricated by self-propagating high-temperature synthesis," *Materials Letters*, vol. 58, pp. 1683-1686, 2003.

[3] C. L. Chu, C. Y. Chung, P. H. Lin, and S. D. Wang, "Fabrication of porous NiTi shape memory alloy for hard tissue implants by combustion synthesis," *Materials Science and Engineering A*, vol. 366, pp. Pages 114-119, 2003.

[4] B. Y. Li, L. J. Rong, Y. Y. Li, and V. E. Gjunter, "Synthesis of porous Ni-Ti shape-memory alloys by self-propagating high-temperature synthesis: reaction mechanism and anisotropy in pore structure," *Acta Materialia*, vol. 48, pp. 3895-3904, 2000.

[5] C. L. Yeh and W. Y. Sung, "Synthesis of NiTi intermetallics by self-propagating combustion," *Journal of Alloys and Compounds*, vol. In Press, Corrected Proof, 2003.

[6] C. Y. Chung, C. L. Chu, and S. D. Wang, "Porous TiNi shape memory alloy with high strength fabricated by self-propagating high-temperature synthesis," *Materials Letters*, vol. 58, pp. 1683-1686, 2004.

[7] S. A. Shabalovskaya, "Surface, corrosion and biocompatibility aspects of Nitinol as an implant material," *Bio-Medical Materials and Engineering*, vol. 12, pp. 69–109, 2002.

[8] B.-Y. Li, L.-J. Rong, and Y.-Y. Li, "Stress-strain behavior of porous Ni-Ti shape memory intermetallics synthesized from powder sintering," *Intermetallics*, vol. 8, pp. 643-646, 2000.

[9] Y. Kaieda, "Fabrication of composition-controlled TiNi shape memory wire using combustion synthesis process and the influence of Ni content on phase transformation behavior," *Science and Technology of Advanced Materials*, vol. 4, pp. 239-246, 2003.

[10] A. M. Locci, R. Orru, G. Cao, and Z. A. Munir, "Field-activated pressure-assisted synthesis of NiTi," *Intermetallics*, vol. 11, pp. 555-571, 2003.

[11] V. I. Itin, V. E. Gyunter, S. A. Shabalovskaya, and R. L. C. Sachdeva, "Mechanical properties and shape memory of porous nitinol," *Materials Characterization*, vol. 32, pp. 179-187, 1994.

[12] M. Castillo, J. J. Moore, F. D. Schowengerdt, R. A. Ayers, X. Zhang, M. Umakoshi, H. C. Yi, and J. Y. Guigne, "Effects of gravity on combustion synthesis of functionally graded biomaterials," *Advances in Space Research*, vol. 32, pp. 265-270, 2003.

[13] C. Suryanarayana, "Mechanical alloying and milling," *Progress in Material Science*, vol. 46, 2001.

[14] J. W. G. a. R. C. W. W.J. Buehler, *J Appl Phys 34*, pp. 1473., 1963.

[15] D. Mantovani, "Shape Memory Alloy: Properties and Biomedical Applications," *Journal of Materials*, vol. 52, pp. 36, 2000.

[16] S. L. Zhu, X. J. Yang, F. Hu, S. H. Deng, and Z. D. Cui, "Processing of porous TiNi shape memory alloy from elemental powders by Ar-sintering," *Materials Letters*, vol. 58, pp. 2369-2373, 2004.

[17] C. L. Chu, C. Y. Chung, and P. H. Lin, "Influences of solution treatment on compressive properties of porous NiTi shape memory alloy with the porosity of 53.4 vol% fabricated by combustion synthesis," *Journal of Materials Science*, vol. 39, pp. 4949-4951, 2004.

[18] Y.-H. Li, G.-B. Rao, L.-J. Rong, Y.-Y. Li, and W. Ke, "Effect of pores on corrosion characteristics of porous NiTi alloy in simulated body fluid," *Materials Science and Engineering A*, vol. 363, pp. 356-359, 2003.

[19] Kazuhiro Otsuka and Tomoyuki Kakeshita, "Science and Technology of Shape-Memory Alloys: New Developments," presented at MRS BULLETIN CONFERENCE, 2002.

[20] S. Miyazaki, K. Otsuka, and C. M. Wayman, "The shape memory mechanism associated with the martensitic transformation in Ti---Ni alloys--I. Self-accommodation," *Acta Metallurgica*, vol. 37, pp. 1873-1884, 1989.

[21] C. M. Wayman, "Shape memory and related phenomena," *Progress in Materials Science*, vol. 36, pp. 203-224, 1992.

[22] W. J. Buehler and F. E. Wang, "A summary of recent research on the nitinol alloys and their potential application in ocean engineering*1," *Ocean Engineering*, vol. 1, pp. 105-108, 1968.

[23] R. C. L. Sachdeva and S. Miyazaki, "Nitinol as a Biomedical Material," in *Encyclopedia of Materials: Science and Technology*. Oxford: Elsevier Science Ltd, 2003, pp. 6155-6160.

[24] I. Jarrige, P. Holliger, T. P. Nguyen, J. Ip, and P. Jonnard, "From diffusion processes to adherence properties in NiTi microactuators," *Microelectronic Engineering*, vol. 70, pp. 251-254, 2003.

[25] H. Kienapfel, C. Sprey, A. Wilke, and P. Griss, "Implant fixation by bone ingrowth," *The Journal of Arthroplasty*, vol. 14, pp. 355-368, 1999.

[26] Y. Zhao, M. Taya, Y. Kang, and A. Kawasaki, "Compression behavior of porous NiTi shape memory alloy," *Acta Materialia*, vol. 53, pp. 337-343, 2005.

[27] Y.-H. Li, L.-J. Rong, and Y.-Y. Li, "Compressive property of porous NiTi alloy synthesized by combustion synthesis," *Journal of Alloys and Compounds*, vol. 345, pp. 271-274, 2002.

[28] C. L. Chu, C. Y. Chung, and P. H. Lin, "DSC study of the effect of aging temperature on the reverse martensitic transformation in porous Ni-rich NiTi shape memory alloy fabricated by combustion synthesis," *Materials Letters*, vol. 59, pp. 404-407, 2005.

[29] S. Kujala, J. Ryhanen, A. Danilov, and J. Tuukkanen, "Effect of porosity on the osteointegration and bone ingrowth of a weight-bearing nickel-titanium bone graft substitute," *Biomaterials*, vol. 24, pp. 4691-4697, 2003.

[30] "http://www.biorthex.com/," 22 Oct 2003.

[31] M. Zhu, T. C. Li, J. T. Liu, and D. Z. Yang, "Microstructure characteristics of NiTi shape memory alloy obtained by explosive compact of elemental nickel and titanium powders," *Acta Metallurgica et Materialia*, vol. 39, pp. 1481-1487, 1991.

[32] R. P. Welsh, R. M. Pilliar, and I. Macnab, "Surgical implants. The role of surface porosity in fixation to bone and acrylic," *The Journal Of Bone And Joint Surgery. American Volume*, vol. 53, pp. 963-977, 1971.

[33] S. Kujala, "Biocompatibility and bomechanical aspects of nitinol shape memory metal implants," in *Department of Surgery, Departement of Anatomy and Cell Biology*: University of Oulu, 2003, pp. 88.

[34] A.-C. Maurin, R. Fromental, D. Cantaloube, and R. Caterini, "Porous tantalum and nitinol colonization by human osteoblasts in three-dimensional cell cultures," *Implantodontie*, vol. 14, pp. 44-50.

[35] B.-Y. Li, L.-J. Rong, and Y.-Y. Li, "Anisotropy of dimensional change and its corresponding improvement by addition of TiH2 during elemental powder sintering of porous NiTi alloy," *Materials Science and Engineering A*, vol. 255, pp. 70-74, 1998.

[36] Y.-H. Li, G.-B. Rao, L.-J. Rong, Y.-Y. Li, and W. Ke, "Effect of pores on corrosion characteristics of porous NiTi alloy in simulated body fluid," *Materials Science and Engineering A*, vol. 363, pp. 356-359, 2003

[37] Y.-H. Li, L.-J. Rong, and Y.-Y. Li, "Pore characteristics of porous NiTi alloy fabricated by combustion synthesis," *Journal of Alloys and Compounds*, vol. 325, pp. 259-262, 2001.

[38] Y.-H. Li, G.-B. Rao, L.-J. Rong, and Y.-Y. Li, "The influence of porosity on corrosion characteristics of porous NiTi alloy in simulated body fluid," *Materials Letters*, vol. 57, pp. 448-451, 2002.

[39] P. B. Entchev and D. C. Lagoudas, "Modeling of transformation-induced plasticity and its effect on the behavior of porous shape memory alloys. Part II: porous SMA response," *Mechanics of Materials*, vol. 36, pp. 893-913, 2004.

[40] E. Muller, C. Drasar, J. Schilz, and W. A. Kaysser, "Functionally graded materials for sensor and energy applications," *Materials Science and Engineering A*, vol. 362, pp. 17-39, 2003.

[41] V.E. Gunther, "Porous nickel-titanium alloy article,." United States Patent 5,986,169: Biorthex Inc.(CA), 1999.

[42] B. Yuan, C. Y. Chung, and M. Zhu, "Microstructure and martensitic transformation behavior of porous NiTi shape memory alloy prepared by hot isostatic pressing processing," *Materials Science and Engineering A*, vol. 382, pp. 181-187, 2004.

[43] Y. Zhao, M. Taya, and H. Izui, "Study on energy absorbing composite structure made of concentric NiTi spring and porous NiTi," *International Journal of Solids and Structures*, vol. 43, pp. 2497-2512, 2006 .

[44] S. O. K. Ishizaki, T. Fukikawa, A. Takata, *German Patent: P4091 346.5 1991, US Patent: 5,126,103,1992, Japanese Patent: H2-68709.*

[45] Y. S. Kang, Kikuchi, K., Kawasaki, "A Fabrication and characterization of functionally graded Ni/Al2O3/Ni compliant pad," presented at Proceeding of ISSPS, Japan., 2001.

[46] Z. A. Munir and U. Anselmi-Tamburini, "Self-propagating exothermic reactions: The synthesis of high-temperature materials by combustion," *Materials Science Reports*, vol. 3, pp. 277-365, 1989.

[47] M. D. McNeese, D. C. Lagoudas, and T. C. Pollock, "Processing of TiNi from elemental powders by hot isostatic pressing," *Materials Science and Engineering A*, vol. 280, pp. 334-348, 2000.

[48] A.G.Merzhanov and A.E.Sytschev, "About Self-Propagating High-temperature Synthesis http://www.ism.ac.ru/handbook/shsf.htm."

[49] Z. A. Munir, "Combustion and plasma synthesis of high-temperature materials," presented at International Symposium on Combustion and Plasma Synthesis of High-Temperature Materials, San Francisco, Calif, 1988.

[50] A. Varma and J.-P. Lebrat, "Combustion synthesis of advanced materials," *Chemical Engineering Science*, vol. 47, pp. 2179-2194, 1992.

[51] A. Makino, "Fundamental aspects of the heterogeneous flame in the self-propagating high-temperature synthesis (SHS) process," *Progress in Energy and Combustion Science*, vol. 27, pp. 1-74, 2001.

[52] I. Barin, *Thermochemical data of pure substances*: Weinheim, Federal Republic of Germany ; New York, NY, USA : VCH, 1989.

[53] R. M. German, *Powder Metallurgy Science*. Princeton, New Jersey: Metat powder Industries Federation, 1984.

[54] R. M. German, *Particle Packing Characteristics*: Metal Powder Industries Federation, 1999.

[55] P. Mossino, "Some aspects in self-propagating high-temperature synthesis," *Ceramics International*, vol.30, pp.311-33 2, 2004.

[56] E. A.-M. Levashov, O. V. - Kudryashov, A. E. - Gammel, F. - Suchentrunk, R., "Effects of Nanocrystalline Powders Additions on the Characteristics of Combustion Process, Phase- and Structure-Formation, and Properties of SHS Alloys on Titanium Carbide Base," *journal of Materials Synthesis and Processing*, vol. 10, pp. 231-236, 2002.

[57] E. M. Hunt, K. B. Plantier, and M. L. Pantoya, "Nano-scale reactants in the self-propagating high-temperature synthesis of nickel aluminide," *Acta Materialia*, vol. 52, pp. 3183-3191, 2004.

[58] H. Gleiter, "Nanocrystalline materials," *Progress in Materials Science*, vol. 33, pp. 223-315, 1989.

[59] C. Suryanarayana, "Mechanical alloying and milling," *Progress in Materials Science*, vol. 46, pp. 1-184, 2001.

[60] F. Charlot, E. Gaffet, B. Zeghmati, F. Bernard, and J. C. Niepce, "Mechanically activated synthesis studied by X-ray diffraction in the Fe-Al system," *Materials Science and Engineering A*, vol. 262, pp. 279-288, 1999.

[61] M. S. El-Eskandarany, *Mechanical alloying for fabrication of advanced engineering materials*. New York: NOYES PUBLICATIONS, 2001.

[62] J. William D. Callister, *Materials Science and Engineering:An introduction*, 3 ed: JOHN WILEY & SON, INC., 1994.

[63] K. Goi, Y.W. Gu, A.E.W. Jarfors, D.L. Butler, and C. S. Lim, "Preparation and Characterization of Mechanically Alloyed Ni-Ti," presented at International Conference on Precision Engineering 2003/04, Grand Hyatt Singapore, 2004.

[64] C. Gras, D. Vrel, E. Gaffet, and F. Bernard, "Mechanical activation effect on the self-sustaining combustion reaction in the Mo-Si system," *Journal of Alloys and Compounds*, vol. 314, pp. 240-250, 2001.

[65] K. W. K. Yeung, K. M. C. Cheung, W. W. Lu, and C. Y. Chung, "Optimization of thermal treatment parameters to alter austenitic phase transition temperature of NiTi alloy for medical implant," *Materials Science and Engineering A*, vol. 383, pp. 213-218, 2004.

[66] C. L. Chu, C. Y. Chung, and P. H. Lin, "Phase transformation behaviors in porous Ni-rich NiTi shape memory alloy fabricated by combustion synthesis," *Materials Science and Engineering A*, vol. 392, pp. 106-111, 2005

[67] K. Otsuka and X. Ren, "Physical metallurgy of Ti-Ni-based shape memory alloys," *Progress in Materials Science*, vol. 50, pp. 511-678, 2005.

[68] D. L. Wheeler, A. A. Campbell, G. L. Graff, and G. J. Miller, "Histological and biomechanical evaluation of calcium phosphate coatings applied through surface-induced mineralization to porous titanium implants," *Journal of Biomedical Materials Research*, vol. 34, pp. 539-543, 1997.

[69] G. F. Lee, "Resonance apparatus for damping measurements," *Metallurgical and Materials Transactions A: Physical Metallurgy and Materials Science*, vol. 26A, pp. 2819-2823, 1995.

[70] Y. Zhao, M. Taya, and H. Izui, "Study on energy absorbing composite structure made of concentric NiTi spring and porous NiTi," *International Journal of Solids and Structures*, vol. 43, pp. 2497-2512, 2006.

LIST OF PUBLICATIONS FROM THIS WORK

1) Y.W. Gu, C.W. Goh, L.S. Goi, C.S. Lim, A.E.W. Jarfors, B.Y. Tay and M.S. Yong "Solid state synthesis of nanocrystalline and/or amorphous 50Ni-50Ti alloy," *Materials Science and Engineering A,* Volume 392, Issues 1-2, 15 February 2005, Pages 222-228

2) C.W. Goh, Y.W. Gu, C.S. Lim, A.E.W. Jarfors, B.Y. Tay & M.S. Yong "Effect of using Mechanically Alloyed reaction agent on Self-Propagating High-Temperature Synthesis of Porous NiTi" *The 3rd International Conference on Materials Processing for Properties and Performance (MP3)*, Singapore, 24 - 26 November 2004, pp 905 - 912

3) C.W. Goh, Y.W. Gu, C.S. Lim, B.Y Tay "Influence of nanocrystalline Ni-Ti reaction agent on self-propagation high-temperature synthesized porous NiTi" *Intermetallics* (submitted).

APPENDICES

Appendix A. The certificate of analysis on Ti powder

CERAC™ incorporated
Quality Manufacturing Since 1964

Certificate of Analysis

Item Number	Description	Lot Number
T-2045	TITANIUM METAL, Ti Typically 99.9% (Na <10 ppm) -200 mesh (<74 μm)	X25822

SPECIFIC ANALYSIS OR PROPERTY

Test For	Found	Theoretical
Na	2 ppm	

SPECTROGRAPHIC ANALYSIS

Element	Result (%)	Element	Result (%)	Element	Result (%)
Ce	<0.001	Sr	0.0005		

X-RAY DIFFRACTION ANALYSIS

Chart Number: D39483
Major Ti matches PDF 44-1294 Hexagonal

CERAC Incorporated
P.O. Box 1178, Milwaukee, WI 53201
(414) 289-9800 Phone (414) 289-9805 Fax

Brian T Wegner

Brian T Wegner, Q.A. Supervisor July 2, 2001

Appendix B. The certificate of analysis on Ni powder

CERAC™ Incorporated
Quality Manufacturing Since 1964

Certificate of Analysis

Item Number	Description	Lot Number
N-1089	NICKEL METAL, NI Typically 99.9% pure about 5 microns average	X0026878

SPECIFIC ANALYSIS OR PROPERTY

Test For	Found	Theoretical
Fisher Size (APS)	2.52 µ	

SPECTROGRAPHIC ANALYSIS

Element	Result (%)	Element	Result (%)	Element	Result (%)
Co	<0.0003				

X-RAY DIFFRACTION ANALYSIS

CERAC Incorporated
P.O. Box 1178, Milwaukee, WI 53201
(414) 289-9800 Phone (414) 289-9805 Fax

Brian T Wegner

Brian T Wegner, QA Engineer — September 6, 2002

Appendix C. Analytical balance: Mettler-Toledo™ B204-S

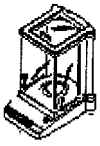

Model (part no.)	Readability	Max. capacity	Repeatability (s)	Linearity	Weighing pan (mm)
AB135-S Dual Range	0.01mg/0.1mg	31g/120g	0.03mg/0.1mg	±0.2mg*	⌀ 80
AB265-S Dual Range	0.01mg/0.1mg	61g/220g	0.05mg/0.1mg	±0.2mg*	⌀ 80
AB54-S	0.1mg	51g	0.1mg	±0.2mg	⌀ 80
AB104-S	0.1mg	110g	0.1mg	±0.2mg	⌀ 80
AB204-S	0.1mg	220g	0.1mg	±0.2mg	⌀ 80
AB304-S	0.1mg	320g	0.1mg	±0.4mg	⌀ 80

* Typical with 10g sample in fine range: ±0.03mg
Certified versions of all models are available.
You will find further details of our balances, equipment, and accessories in our laboratory and industry catalogs, or at www.mt.com

METTLER TOLEDO